

# THE ANTENNAE GALAXIES (NGC 4038/4039) REVISITED: ACS AND NICMOS OBSERVATIONS OF A PROTOTYPICAL MERGER<sup>1</sup>

BRADLEY C. WHITMORE,<sup>2</sup> RUPALI CHANDAR,<sup>3</sup> FRANÇOIS SCHWEIZER,<sup>4</sup>  
BARRY ROTHBERG,<sup>2,5</sup> CLAUD LEITHERER,<sup>2</sup> MARCIA RIEKE,<sup>6</sup> GEORGE RIEKE,<sup>6</sup>  
W. P. BLAIR,<sup>7</sup> S. MENGEL,<sup>8</sup> & A. ALONSO-HERRERO<sup>9</sup>

## ABSTRACT

The Advanced Camera for Surveys (ACS) and the Near Infrared Camera and Multi-Object Spectrometer (NICMOS) have been used to obtain new *Hubble Space Telescope* images of NGC 4038/4039 (“The Antennae”). These new observations allow us to better differentiate compact star clusters from individual stars, based on both size and color. We use this ability to extend the cluster luminosity function by approximately two magnitudes over our previous WFPC2 results, and find that it continues as a single power law,  $dN/dL \propto L^\alpha$  with  $\alpha = -2.13 \pm 0.07$ , down to the observational limit of  $M_V \approx -7$ . Similarly, the mass function is a single power law  $dN/dM \propto M^\beta$  with  $\beta = -2.10 \pm 0.20$  for

---

<sup>1</sup>Based on observations with the NASA/ESA *Hubble Space Telescope*, obtained at the Space Telescope Science Institute, which is operated by the Association of Universities for Research in Astronomy, Inc. under NASA contract NAS5-26555. Also based on data obtained from the Hubble Legacy Archive, which is a collaboration between the Space Telescope Science Institute (STScI/NASA), the Space Telescope European Coordinating Facility (ST-ECF/ESA) and the Canadian Astronomy Data Centre (CADC/NRC/CSA).

<sup>2</sup>Space Telescope Science Institute, 3700 San Martin Drive, Baltimore, Maryland 21218; whitmore@stsci.edu, etc.

<sup>3</sup>University of Toledo, Department of Physics & Astronomy, Toledo, OH 43606

<sup>4</sup>Carnegie Observatories, 813 Santa Barbara Street, Pasadena, CA 91101

<sup>5</sup>Naval Research Laboratory, Remote Sensing Division, Code 7211, 4555 Overlook Ave., Southwest, Washington, D.C. 20375

<sup>6</sup>The University of Arizona, Department of Astronomy, 933 N. Cherry Ave., Tucson, AZ 85721-0065

<sup>7</sup>Center for Astrophysical Sciences, The Johns Hopkins University, 3400 N. Charles Street, Baltimore, MD 21218

<sup>8</sup>European Southern Observatory, Germany; s.mengel@gmx.net

<sup>9</sup>Instituto de Estructura de la Materia, CSIC, Serrano 121, 28006 Madrid, Spain

clusters with ages  $< 3 \times 10^8$  yr, corresponding to lower mass limits that range from  $10^4$  to  $10^5 M_\odot$ , depending on the age range of the subsample. Hence the power law indices for the luminosity and mass functions are essentially the same. The luminosity function for intermediate-age clusters (i.e.,  $\sim 100$ – $300$  Myr old objects found in the loops, tails, and outer areas) shows no bend or turnover down to  $M_V \approx -6$ , consistent with relaxation-driven cluster disruption models which predict the turnover should not be observed until  $M_V \approx -4$ . An analysis of individual  $\sim 0.5$ -kpc sized areas over diverse environments shows good agreement between values of  $\alpha$  and  $\beta$ , similar to the results for the total population of clusters in the system. There is tentative evidence that the values of both  $\alpha$  and  $\beta$  are flatter for the youngest clusters in some areas, but it is possible that this is caused by observational biases. Several of the areas studied show evidence for age gradients, with somewhat older clusters appearing to have triggered the formation of younger clusters. The area around Knot B is a particularly interesting example, with an  $\sim 10$ – $50$  Myr old cluster of estimated mass  $\sim 10^6 M_\odot$  having apparently triggered the formation of several younger, more massive (up to  $5 \times 10^6 M_\odot$ ) clusters along a dust lane. A comparison with new NICMOS observations reveals that only  $16 \pm 6\%$  of the IR-bright clusters in the Antennae are still heavily obscured, with values of  $A_V > 3$  mag.

*Subject headings:* galaxies: star clusters—galaxies: interactions—galaxies: individual (NGC 4038 – NGC 4039)

## 1. Introduction

The Antennae (NGC 4038/39) are the youngest and nearest example of a pair of merging disk galaxies in the Toomre (1977) sequence. As such, they have been observed in virtually every wavelength regime: radio (e.g., Wilson et al. 2000, 2003; Neff & Ulvestad 2000; Hibbard et al. 2001; Zhu, Seaquist & Kuno 2003; Schulz et al. 2007), infrared (e.g., Mirabel et al. 1998; Kassin et al. 2003; Wang et al. 2004; Brandl et al. 2005, 2009; Mengel et al. 2005; Clark et al. 2007; Rossa et al. 2007; Gilbert & Graham 2007; Mengel et al. 2008), optical (Rubin, Ford, & D’Odorico 1970; Whitmore & Schweizer 1995; Whitmore et al. 1999; Kassin et al. 2003; Bastian et al. 2006), ultraviolet (e.g., Hibbard et al. 2005), and X-ray (e.g., Fabbiano et al. 2003, 2004; Metz et al. 2004; Zezas et al. 2006, 2007). One important result has been the discovery that much of the star formation occurs in the form of massive compact star clusters (Whitmore & Schweizer 1995; Whitmore et al. 1999), often referred to as “super star clusters.” Some of these clusters have properties expected of young globular clusters

(i.e., mass, effective radius, etc.). Hence, it may be possible to study the formation (and disruption, see Fall, Chandar, & Whitmore 2005, hereafter FCW05; Whitmore, Chandar, & Fall 2007, hereafter WCF07; and Fall, Chandar, & Whitmore 2009, hereafter FCW09) of globular clusters in the local universe rather than trying to determine how they formed some 13 Gyr ago.

One of the primary challenges for previous observations of the Antennae was the difficulty of distinguishing faint young clusters from individual young stars, which can be as luminous as  $M_V \approx -9$ . The Advanced Camera for Surveys, with its superior spatial resolution over a wider field of view than the Wide Field and Planetary Camera 2 (WFPC2), provides an opportunity to improve this situation. The ability to better distinguish faint clusters from stars provides several new science opportunities. The first is an extension of the cluster luminosity and mass functions to lower values. A large number of studies have found that the young cluster luminosity function (LF) in a variety of star-forming galaxies is a power law of the form  $\phi(L)dL \propto L^\alpha dL$  with a value of  $\alpha \approx -2$  (e.g., see compilations in Whitmore 2003; Larsen 2005, 2006; de Grijs & Parmentier 2007). However, recently there have been claims (e.g., Fritze-von Alvensleben 2004; de Grijs & Parmentier 2007; Anders et al. 2007) that the initial cluster luminosity function has a turnover at faint magnitudes, and is closer to the Gaussian form found for old globular clusters. The ability to push the LF about 2–3 mag fainter provides a more stringent test of the power-law nature of the initial cluster LF. Areas in the outskirts of the galaxy provide an especially sensitive test, since their low background levels allow cluster detections to fainter magnitudes. Most of the clusters in these tails, loops, and outer areas have intermediate ages (approximately 100–300 Myr) and have, therefore, survived the initial stages of cluster disruption or “infant mortality” associated with the removal of interstellar material (see Hills 1980; Lada, Margulis & Dearborn 1984; Boily & Kroupa 2003; Bastian & Goodwin 2006; and Fall et al. 2010 for theoretical discussions and Lada & Lada 2003, FCW05, and WCF07 for observational evidence).

Several studies have also found that the young cluster mass function (MF) in a variety of galaxies is a power law of the form  $\phi(M)dM \propto M^\beta dM$  with a value of  $\beta \approx -2$  (e.g., Zhang & Fall 1999 in the Antennae; Hunter et al. 2003 in the Magellanic Clouds; Bik et al. 2003 in M51; and Chandar et al. 2010 in M83). While the LF and MF are sometimes considered to be interchangeable, this is not true for populations of clusters that include a wide range of ages, and hence mass-to-light ratios. In fact, the observed similarity in the values of  $\alpha$  and  $\beta$  can be used as indirect evidence that the age and mass distributions are independent, at least up to ages of 300 Myr (e.g., Fall 2006). This independence has been established more directly in FCW05, and can be expressed explicitly by the fact that the bivariate mass-age distribution  $g(M, \tau)$  can be approximated by the product of the univariate mass and age distribution:  $g(M, \tau) \approx M^\beta \tau^\gamma$  (FCW05, WCF07, FCW09).

There have also been claims for several galaxies, including the Antennae, that there is a cutoff to the upper mass with which clusters can form (e.g., Gieles et al. 2006; Bastian 2008; Larsen 2009), and that there are bends in the age distributions of some galaxies (e.g., Boutloukos & Lamers 2003, and Lamers et al. 2005). However, based on our WFPC2 data, we found that both the mass function and the age distribution are simple power laws (see FCW09 for discussion). We suspect that these apparent discrepancies are due to selection effects in other studies, in particular to the exclusion of crowded regions which contain most of the young clusters. In this paper we examine whether or not there is evidence for such bends or cutoffs from our new ACS data set.

A second new science opportunity enabled by the high-resolution ACS images is to dissect the contents, both clusters and individual stars, in some of the spectacular star forming knots found in the Antennae. We will be able to assess whether some of the universal trends found for star-forming galaxies, for example the correlation between the absolute visual magnitude of the brightest cluster and the total number of clusters (e.g., Whitmore 2003), holds or not in individual sub-kpc regions of the Antennae. Age and mass estimates for the clusters in these regions will allow us to assess how star formation proceeds in these extreme environments, and whether there is evidence for sequential star formation.

In this paper, we adopt a distance modulus of 31.71 mag for the Antennae, as found by Schweizer et al. (2008) based on the Type Ia supernova 2007sr. This modulus corresponds to a distance of 22 Mpc for a Hubble constant of  $H_0 = 72 \text{ km s}^{-1} \text{ Mpc}^{-1}$ . Note that this distance is slightly further than that adopted in our earlier papers (19.2 Mpc), and quite different from the shorter distance of 13.3 Mpc found by Saviane et al. (2008), based on an apparent misidentification of the tip of the red giant branch (see Schweizer et al. 2008 for details). At a distance of 22 Mpc,  $1''$  is equivalent to 107 pc, and one  $0''.05$  ACS/WFC pixel covers 5.33 pc.

The remainder of this paper is organized as follows: §2 describes the observations and photometric reductions; §3 gives details of our procedure to estimate the ages and masses of the clusters; and §4 summarizes our method for separating stars and clusters (with more details included in Appendix A). We compare the 50 most luminous, massive, and IR-bright clusters in §5; examine the LF of star clusters in the Antennae in §6, and then the mass and age distributions in §7. In §8 we perform a detailed analysis of the cluster populations in star-forming knots and other regions, and §9 discusses patterns of star formation, including triggered star formation. A summary is provided in §10. Future papers will include a more detailed study of the age, mass, and size distributions of the clusters (Chandar et al., in prep.) and will incorporate our NICMOS observations of the Antennae more fully (Rothberg et al., in prep).

## 2. Data and Analysis

### 2.1. Optical ACS Observations

Observations of the main bodies of NGC 4038/39 were made with the *Hubble Space Telescope* (*HST*), using the Advanced Camera for Surveys (ACS), as part of Program GO-10188. Multi-band photometry was obtained in the following optical broad-band filters: F435W ( $\approx B$ ), F550M ( $\approx V$ ), and F814W ( $\approx I$ ). Observations in  $V$  were made using the medium-width filter F550M rather than the more widely used broad-band filter F555W to minimize possible contamination from [O III] and other nebular emission lines. Additional observations were made using the narrow-band filter F658N to study  $H\alpha$  emission at the redshift of the Antennae. All optical observations were made with the Wide Field Camera (WFC) of the ACS, with a scale of  $0''.049 \text{ pixel}^{-1}$  yielding a field of view of  $\sim 202'' \times 202''$ . Four separate exposures were taken for each of the filters F435W, F658N, and F814W, yielding total exposure times of 2192 s, 2300 s, and 1680 s, respectively. Six separate exposures were taken through the F550M filter, with a total exposure time of 2544 s. The longer integration and larger number of dither pointings maximized the spatial resolution of the F550M observations. Slightly shorter ACS/WFC exposures were also taken at two positions in the Southern tail, using the filters F435W, F550M, F658N, and F814W, and will be presented in a future paper.

Archival F336W photometry of the Antennae (Program GO-5962) was used to supplement our optical ACS/WFC observations. Two sub-pixel dither positions separated by  $0''.025$  were observed through the F336W filter, yielding a total exposure time of 4500 s.

The flatfielded ACS/WFC images were co-added using the task MULTIDRIZZLE (Koeke-moer et al. 2002) in PyRAF/STSDAS. A PIXFRAC value of 0.9 and a final scale of  $0''.045 \text{ pixel}^{-1}$  were used for each of the filters. A second, higher resolution F550M image was constructed to take advantage of the additional pointings. This “super-resolution” image was constructed using a PIXFRAC value of 0.7, and has a scale of  $0''.03 \text{ pixel}^{-1}$ . From here on we will use the term “super-res” to denote the  $0''.03$ -pixel F550M image. The archival WFPC2/F336W images were co-added in a manner similar to that used by Whitmore et al. (1999), but using MULTIDRIZZLE rather than the older DRIZZLE task. Each chip was treated separately, creating four final output images (PC, WF2, WF3, and WF4). A PIXFRAC value of 0.8 was used for all four chips, resulting in final scales of  $0''.035 \text{ pixel}^{-1}$  for the PC chip and  $0''.075 \text{ pixel}^{-1}$  for each of the WF chips.

Figure 1 shows a color image of the Antennae produced by Lars Christensen (ESA). The F435W image is shown in blue, F550M is shown in green, and a combination of the F814W and F658N ( $H\alpha$ ) images is shown in red. One intriguing aspect of this color image

is that it makes it possible to tell the difference between regions that are red because they have strong H $\alpha$  emission (these have a pinkish tint) and regions that are red because they suffer strong reddening due to dust (these have an orange tint).

Catalogs of cluster candidates were constructed from the F550M “super-res” image using the task DAOFIND in IRAF. The higher resolution of the “super-res” image is better suited to separate close objects which might otherwise remain blended in the lower resolution images. Removal of artifacts (e.g., hot pixel residuals, remaining cosmic rays) and background galaxies was aided by the calculation of a “Concentration Index”  $C$  for each object, which is taken to be the difference between magnitudes measured within a one and a three pixel radius (see Whitmore et al. 1999). We note that more concentrated objects, such as stars, have lower values of  $C$  (i.e.,  $\approx 1.45$ ), while extended objects, such as clusters, have larger values of  $C$  (i.e.,  $> 1.52$ ). Hence, this parameter might more properly be called a “diffuseness” index. However, for historical uniformity we prefer to retain the term “Concentration” Index. We also used the FWHM measured by the IRAF task RADPROF, and a parameter which we refer to as the “Flux Ratio,” which is defined to be the ratio of the flux in a 3-pixel radius aperture to the flux measured in the background annulus. This parameter was found to be useful for removing false detections in areas of dust. The final object catalog was assembled using parameter values of  $C > 0.0$ ,  $1.5 \text{ pixels} < \text{FWHM} < 5.5 \text{ pixels}$ , and a Flux Ratio  $> 1$ , and contained 60,790 candidate objects. For reference, a typical FWHM for stars in the Antennae is 1.7 pixels and for clusters is 2.0 pixels.

It has been suggested that the  $C$  technique, which uses the difference between magnitudes measured within two different apertures, may be sensitive to the precise center of an object at the sub-pixel level (Anders et al. 2006). If true, this would mean that objects of the same intrinsic size, but falling at the center of a pixel versus near the edge of a pixel, might have values of  $C$  that differ by as much as a magnitude or more according to Figure 29 in Anders et al. We tested for this effect by comparing our measured values of  $C$  for a number of isolated point sources believed to be foreground stars (i.e., Training Set 1 below). Figure 2a shows little, if any, trend. That is, if we break the sample in half, objects with more central pixel values have a mean  $\bar{C} = 1.437 \pm 0.014$ , while objects centered more on the pixel edges have a value of  $\bar{C} = 1.459 \pm 0.013$ . Hence, the difference in  $\bar{C}$  is only  $0.022 \pm 0.019$ . We can increase the sample by including all objects with  $C < 1.52$  and  $V < 23 \text{ mag}$ . While this sample may include some unresolved clusters in addition to stars (as discussed in §4), we again see no discernible trend, with more centrally positioned objects having a mean  $\bar{C} = 1.459 \pm 0.005$ , while objects with centers closer to the edge of a pixel have  $\bar{C} = 1.460 \pm 0.005$ . Hence, the difference is  $0.001 \pm 0.006$ . These comparisons show that centering has a negligible effect on our measurements of  $C$ . We also note that, while using as large a radius as advocated by Anders et al. (i.e.,  $\sim 5$  pixels) might be optimal when

objects are well separated, in crowded fields similar to the Antennae smaller apertures are clearly to be preferred.

The IRAF tasks XY2RD and RD2XY were used to convert object coordinates in the “super-res” F550M image to the F435W, F550M, F658N, and F814W ACS/WFC image coordinate system, as well as to the F336W WFPC2 coordinate system. Any remaining small shifts in object positions were determined for each filter from the task GEOMAP. Aperture photometry for the ACS/WFC data was performed using the IRAF task PHOT, with a 2-pixel radius and inner and outer background annuli of 4 and 7 pixels, respectively, corresponding to angular sizes of  $0''.09$ ,  $0''.18$ , and  $0''.315$  in radius. The VEGAMAG zeropoint values for ACS/WFC of 25.779, 24.867, and 25.501 mag were used for the F435W, F550M, and F814W images (Sirianni et al. 2005). Aperture photometry for the F336W WFPC2 data on the PC chip was conducted using an aperture with a 2-pixel radius and inner and outer background annuli of 4 and 7 pixels, respectively, corresponding to angular sizes of  $0''.07$ ,  $0''.14$ , and  $0''.245$ , respectively. An aperture radius of 1.5 pixels, and inner and outer background annuli of 3 and 6 pixel radii, corresponding to  $0''.112$ ,  $0''.225$ , and  $0''.45$ , respectively, were used for the WF2, WF3, and WF4 chips.

Aperture corrections, defined as the amount of light in magnitudes required to extrapolate from an aperture magnitude to a total magnitude, were derived by making photometric measurements of isolated, high signal-to-noise (S/N) clusters in each filter (for the F550M filter this was done on both the normal and “super-res” ACS/WFC images) and for each individual CCD in the WFPC2 data. Aperture corrections for clusters were found to be significantly larger than those for isolated stars, for all instruments and filters. A median value was used for the aperture corrections for each filter. The aperture corrections used for the 2-pixel photometry of the normal ACS/WFC images correspond to 0.905, 0.890, and 0.915 mag for the F435W, F550M, and F814W images, respectively. The aperture corrections for the 3-pixel photometry of the “super-res” F550M image was 0.886 mag. These aperture corrections are for the 2- or 3-pixel apertures to a  $0''.5$ -radius aperture. Aperture corrections from  $0''.5$  to infinity were taken from Sirianni et al. (2005).

Taking the different sizes of clusters into account properly would require different aperture corrections for each cluster. We experimented with making such corrections by deriving a formula relating aperture corrections and  $C$  indices for isolated, high S/N clusters. While this works well for many clusters, in crowded regions where values of  $C$  can be very uncertain the use of the formula adds considerable noise. Hence, corrections for variable cluster sizes have not been made in the current paper, but will be revisited in a future paper (Chandar et al., in preparation). We note that while this use of constant corrections typically makes individual absolute magnitudes of clusters uncertain by a few tenths of a magnitude (and

more than a full magnitude in a few exceptional cases), the effects on colors are negligible since the latter are determined from fixed apertures.

Aperture corrections for the F336W images and the 2-pixel PC and 1.5-pixel WF2, WF3, and WF4 apertures correspond to 1.041, 0.989, 0.937, and 1.055 mag, respectively. These corrections take the photometry in 2- or 1.5-pixel radius apertures to  $0''.5$ . The standard 0.1 mag correction from  $0''.5$  to infinity was then added to the above corrections (Holtzmann et al. 1995). We also applied Charge Transfer Efficiency (CTE) corrections to the WFPC2/F336W photometry based on the prescription given by Dolphin (2000).<sup>1</sup> We computed the X and Y coordinates for each object on the original images for each dither position. For objects appearing in both dither positions we adopted weighted averages of the CTE correction.

In addition to the data described above, long-slit H $\alpha$  observations using the Space Telescope Imaging Spectrograph (STIS) were planned as part of this proposal, similar to those reported by Whitmore et al. (2005). Unfortunately, STIS stopped working before these observations could be obtained.

Completeness corrections were determined by adding artificial clusters in regions of different background levels to the F550M “super-res” image, using the IRAF task MKOBJECT. These artificial clusters had the same median values of  $C$  and FWHM as real cluster candidates over a magnitude range of 18 to 28. The artificial clusters were then run through the same detection algorithms as used for real cluster candidates. Recovery of the artificial clusters was based on two criteria: (1) whether the recovered luminosity was within  $\pm 0.1$  mag of the input magnitude, and (2) whether the recovered artificial cluster was detected within  $\pm 0.5$  pixel of its input coordinates. The numbers of recovered artificial clusters were then sorted as a function of the background level (we used seven different background levels), binned in 0.25 mag bins, and compared with the initial numbers of artificial clusters. Completeness curves were constructed by smoothing the binned data using a boxcar smoothing algorithm and interpolating a curve through these points. Figure 3 shows the completeness curves for the different background levels. The dashed horizontal line marks the 50% completeness level. The completeness limits in  $V$  at 50% for the seven background levels are: 26.5, 26.4, 26.0, 25.3, 24.7, 24.2, and 23.3 mag, respectively.

In the rest of the present paper we will sometimes use the loose terminology “ $U$ ” for the F336W filter for brevity, and similarly “ $B$ ” for F435W, “ $V$ ” for F550M, and “ $I$ ” for F814W.

---

<sup>1</sup>We used the updated version from the webpage [http://purcell.as.arizona.edu/wfpc2\\_calib/](http://purcell.as.arizona.edu/wfpc2_calib/).



## 2.2. Near-Infrared NICMOS Observations

Infrared observations were made using the Near Infrared Camera and Multi-Object Spectrometer (NICMOS) camera on *HST* as part of Program GO-10188. Observations were made using the NIC2 camera with the F160W, F187N, and F237M filters, and the NIC3 camera with the F110W, F160W, F164W, F187N, and F222M filters. Only the NIC3 results are briefly discussed here. See Rothberg et al. (in prep.) for a more detailed presentation of the NICMOS data.

Two sets of NIC3 observations of the “overlap region” were carried out, one including the northern nucleus (NGC 4038) and the other the southern nucleus (NGC 4039). The NIC3 data were not reduced using the standard pipeline products. Instead, raw files were obtained from the archives and were first processed with the routine CALNICA, which flattens the data and performs instrumental calibration of the data, including dark current subtraction, non-linearity correction, conversion to count rates, and cosmic-ray identification. The output data were then processed with the task PEDSUB, which subtracts quadrant-dependent residual biases. Next, hot pixels were identified manually and masked. Finally, foreground stars were identified and masked. The F222M observations included an additional set of observations of a blank field for the purpose of background subtraction, since thermal contributions from the telescope are important in this bandpass.

The NICMOS observations were combined using the MULTIDRIZZLE task in STSDAS with the default values. The linear scale of NIC3 images is  $0''.20 \text{ pixel}^{-1}$ . However, the NIC3 observations were dithered, and the increased sampling made it possible to produce higher resolution data. The data in all three filters were rescaled to a final linear scale of  $0''.15 \text{ pixel}^{-1}$  using a PIXFRAC value of 0.8. The data were rotated to a position angle of  $0^\circ$ , and all bad pixels were ignored in the final combination. No interpolation was used to correct for saturated or bad pixels. Testing of interpolation showed that leaving this turned on in MULTIDRIZZLE produces spurious results in cluster detection and photometry.

Photometry was conducted on the final data once they were divided by an ADCGAIN value of 6.5. The photometric zeropoints used for the photometry correspond to 22.610, 21.818, and 20.134 mag in the F110W, F160W, and F222M filters, respectively, and are on the VEGAMAG system. The aperture sizes used for the candidate-cluster photometry were 1.5 pixels in each filter, which corresponds to an angular size of  $0''.225$  and a spatial size of 24.1 pc. Aperture corrections were measured to compensate for missing flux. Unfortunately, due to the limited FOV no high S/N isolated clusters could be identified for measuring aperture corrections. Hence, archival data for Program 9997 (P.I. Dickinson, Photometric Recalibration of NICMOS) were retrieved and processed in the exact same manner as the target observations for the purpose of obtaining aperture corrections. The FWHM of cluster

candidates on the NIC3 images of the Antennae were found to be very similar to point sources from Program 9997, justifying the use of point-source aperture corrections for the slightly resolved (at least by ACS standards) clusters in the Antennae. Two sets of aperture corrections were applied. The first corrected the  $0''.225$  aperture to a  $1''.1$  aperture used for the photometry zeropoint determination.<sup>2</sup> These aperture corrections correspond to 0.548, 0.628 and 0.723 mag for the F110W, F160W, and F222M filters, respectively. Additional aperture corrections of 0.059, 0.090, and 0.121 mag for the F110W, F160W, and F222M filters, respectively, were used to extrapolate to infinity.

### 3. Age Dating the Clusters

We age date the clusters using our ACS observations in the  $UBVIH_\alpha$  filters, following procedures very similar to those used for our earlier WFPC2 data (e.g., FCW05). We estimate the age, extinction, and mass of each cluster by comparing the integrated photometry described above with predictions from Charlot & Bruzual (2007; hereafter CB07, private communication; also see Bruzual & Charlot 2003) population synthesis models. Figure 4 shows a  $U - B$  vs.  $V - I$  two-color diagram for the 160 brightest observed sources in the  $V$  filter ( $m_V \leq 21.0$ ;  $M_V \leq -10.7$ ). At these high luminosities, all of the objects should be clusters. The measured colors are compared with the CB07 population synthesis models, which are provided on the *HST* VEGAMAG system, with open star symbols marking the predicted locations of  $10^6$ ,  $10^7$ ,  $10^8$ ,  $10^9$ , and  $10^{10}$  yr old model clusters, starting from the upper left. The arrow in the diagram shows the reddening vector for  $A_V = 1.0$  mag. Overall, the model predictions match our cluster photometry relatively well. At the top end there are a fair number of clusters that fall above the models, due to either photometric uncertainties, inappropriate models, or a combination of the two. The open circles represent our measurements of Bastian et al. (2009) clusters and show that these clusters span a relatively large range in color-color space and, hence, in age. A few of the Bastian et al. clusters are not in our sample of the brightest 160 clusters, whence they do not feature a data point at the center of the circle. Two clusters (T54 and T270) are highlighted and will be discussed in more detail below.

While two-color diagrams such as shown in Figure 4 are useful for visualizing the evolution of clusters, and hence are used extensively in this paper, we note that we actually use a  $\chi^2$  minimization technique for age-dating. This means that points outside the models (e.g., the “high” points in Figure 4) can be reasonably well fit. We estimate the age  $\tau$  and

---

<sup>2</sup>See <http://www.stsci.edu/hst/nicmos/performance/photometry/postnics.keywords.html/>.

extinction  $A_V$  for each cluster by performing a least  $\chi^2$  fit that compares observed magnitudes with magnitudes predicted from CB07 stellar population models with solar ( $Z = 0.02$ ) metallicity, appropriate for young stars and clusters in the Antennae (Christopher et al. 2008; Bastian et al. 2009). The best-fit combination of  $\tau$  and  $A_V$  returns the minimum  $\chi^2$ :  $\chi^2(\tau, A_V) = \sum_{\lambda} W_{\lambda} (m_{\lambda}^{\text{obs}} - m_{\lambda}^{\text{mod}})^2$ , where the sum runs over all available broad- and medium-band ( $UBVI$ ) filters and the F658N narrow-band filter, but requires a minimum of three measurements (including the  $V$  band) to estimate age and extinction. The weights are related to the photometric uncertainty  $\sigma_{\lambda}$  through  $W_{\lambda} = [\sigma_{\lambda}^2 + (0.05)^2]^{-1}$ . The F658N filter includes both continuum and (nebular) line emission, and is dominated by line emission for the youngest objects ( $\tau \lesssim \text{several} \times 10^6$  Myr) and by continuum emission for older objects with  $\tau \gtrsim 10^7$  yr. This enables us to use the narrow-band filter as a fifth data point in many cases, regardless of the age of a cluster. We find that including the narrow-band filter helps to break the age–extinction degeneracy, leading to more accurate age estimates in a number of cases. In a forthcoming paper (R. Chandar et al., in prep.) we will provide a more comprehensive description of our age-dating procedure.

Figure 5 (left panel) compares our photometric age estimates for 15 clusters with the spectroscopic ages determined by Bastian et al. (2009) from absorption- and emission-line features in ground-based integrated cluster spectra. This comparison shows that the photometric and spectroscopic age estimates agree within the uncertainties for all but two of the clusters, T54 and T270. Our age estimates are older in both cases. For T270 the discrepancy is probably due to a spatial resolution effect. Whereas we do not see any  $H\alpha$  emission in our small-aperture measurements, consistent with our age estimate of  $\log \tau = 7.86$ , the ground-based spectrum obtained through a much larger aperture shows strong emission lines (see Figure 3 by Bastian et al.). This interpretation is consistent with a blowup of the region shown in the lower right panel of Figure 5 (originally from our Figure 1), which reveals  $H\alpha$  emission close to, but not coincident with the cluster. Although Bastian et al. exclude emission-lines from their fits, it appears that light from younger stars surrounding the cluster may contribute to the stellar continuum within their larger aperture, thereby affecting their results, since they find an age of  $\log \tau < 6.8$  for T270. For T54 the color image shows no surrounding  $H\alpha$  emission (see Figure 5). This object could be either an older cluster with low extinction or a younger cluster with higher extinction. The location of this cluster in the two-color diagram (Figure 4) is consistent with both age estimates, our  $\log \tau = 8.16$  and Bastian et al.’s  $\log \tau = 6.9$ . However, the lack of other nearby clusters and of any  $H\alpha$  emission makes the younger age estimate somewhat suspect.

Other authors (e.g., Anders et al. 2004) have found that including near-IR filters in the age-dating process can be useful. We have chosen to not include the NICMOS observations in our age determinations in the current paper for a variety of reasons, including the following

two: Our NICMOS images cover only  $\sim 50\%$  of the area covered by the ACS images, and the difference in spatial resolution between the NICMOS and ACS images would lead to serious difficulties in crowded areas. We plan to revisit this issue in future papers.

#### 4. Differentiating Stars from Clusters

In Whitmore et al. (1999), one of our primary difficulties was differentiating individual stars from star clusters. The new ACS data presented here, with their higher spatial resolution, provide an opportunity to better separate the two. The concentration index  $C$ , the difference between magnitudes measured within a one and a three pixel radius, is one of the primary tools we use to help differentiate stars from clusters based on their image size.<sup>3</sup>

We begin by identifying three “training sets” of objects: (1) a set in a relatively isolated area primarily containing foreground stars and ancient globular clusters; (2) one in an area of the Northwest Extension (Outer 9 in Figure 17; see also Figure 5 in Whitmore et al. 1999) containing primarily intermediate-age clusters ( $\sim 100\text{--}300$  Myr); and (3) one in a crowded area (Knot S) containing both individual young stars and clusters. The lessons learned from these three training sets will then be applied to objects in the entire galaxy. Many additional details and information on the training sets are given in Appendix A.

Based on Training Set 1 (Figure 6) we find that overall the concentration index  $C$  separates well most stars from old globular cluster candidates, with  $1.37 < C < 1.52$  ( $\bar{C} = 1.448$ , sample rms = 0.049) for stars and  $1.62 < C < 1.78$  ( $\bar{C} = 1.676$ , rms = 0.052) for old globular clusters. We therefore adopt a value of  $C = 1.52$  as our boundary between unresolved and resolved objects. Stars and ancient-cluster candidates also separate fairly nicely in  $U - B$  vs.  $V - I$  two-color diagrams (Figure 6b). This relatively good separation is important for cases where it is difficult to differentiate stars from clusters based on size alone, such as in very crowded regions. See Tables 1 & 2 and Appendix A.1 for more details concerning Training Set 1.

We use Training Set 2, which is dominated by intermediate age ( $\sim 100\text{--}300$  Myr) clusters in the outer portions of the Antennae, to assess how our measurements of  $C$  and age behave

---

<sup>3</sup>We experimented with other size estimates (e.g., the FWHM measured by the IRAF task RADPROF, and the effective or half-light radius  $r_e$  estimated from the ISHAPE software package; Larsen 1999), but found that—while these methods provide superior performance in certain circumstances (e.g., isolated objects with high S/N)—they were less robust in many cases (e.g., very crowded regions). We also tried estimating the residual light after a “mean cluster PSF” had been subtracted from every object, and found that the performance was comparable, but not superior, to the simple  $C$  index.

at fainter magnitudes. In this age range, the brightest stars should have  $M_V \approx -3$ , well below our detection threshold. We find that essentially all objects brighter than  $M_V = -7$  have  $C$  values expected for extended objects, while at fainter absolute magnitudes the scatter increases and a few objects have  $C < 1.52$  despite the fact that they are probably star clusters (Figure 7). One interesting result is that we find a possible correlation between  $M_V$  and  $C$  for these intermediate-age clusters, in the sense that brighter clusters are typically larger, as might be expected. The cluster sizes in the Antennae will be addressed in more detail in a future paper (R. Chandar et al., in prep.). Figure 7 also shows that age estimates begin to fail for  $M_V \geq -7$ . See Table 3 and Appendix A.2 for more details concerning Training Set 2.

Training Set 3 provides a more difficult, but also more typical case of a crowded region including both individual young stars and clusters. Figure 8 shows all objects in and around Knot S, plotted in four two-color diagrams, each for a different range of luminosity. The figure starts with the brightest objects ( $M_V < -10$ ) in the top left panel and ends with relatively faint objects ( $-8 < M_V < -7$ ) in the bottom right panel. The objects with  $C < 1.52$  (i.e., profiles indistinguishable from stars) are shown as open squares, while those with  $C > 1.52$  (i.e., resolved) are shown as solid circles. Evolutionary tracks of CB07 solar-metallicity model clusters are shown as solid lines. Padova models for stars brighter than  $M_V = -6$  are shown by a string of dots in the top left panel. The arrow shows the reddening vector for  $A_V = 1.0$  mag. Based on these models and comparisons with our observations discussed below, we divide the two-color diagram into four distinct regions:

- (1) “cluster space” ( $U - B < 0.6$  and  $V - I > 0.1$ ),
- (2) “foreground-star space” ( $U - B > 0.6$  and  $V - I > 0.9$ ),
- (3) “yellow-star space” ( $U - B > 0.6$  and  $0.1 < V - I < 0.9$ ), and
- (4) “blue-star/cluster space” ( $V - I < 0.1$ ).

Several conclusions can be drawn from Figure 8. The first is that the brightest objects (i.e.,  $M_V < -10$ ) are all consistent with being young ( $< 10$  Myr) clusters with relatively little extinction (i.e., they lie close to the models). This is reassuring, since we have used  $M_V = -9$  [i.e., the Humphreys & Davidson (1979) limit] to differentiate clusters from stars in the past (e.g., Whitmore et al. 1999). The upper-right panel (showing objects with  $-10 < M_V < -9$ ) has three point-like objects that fall in or near what we call yellow-star space. These appear to be luminous yellow supergiant stars. We also find several point-like objects in cluster space, indicating that—based on their position in the two-color diagram—some clusters at the distance of the Antennae appear sufficiently concentrated that they cannot be distinguished from stars based on their size alone. Our final, and perhaps most important, conclusion is that in all cases down to  $M_V = -7$  more than 60% of the objects are resolved, and hence are clusters. This is actually a conservative lower limit since, as we just noted, many of the

unresolved objects are also clusters based on their position in the two-color diagram.

These results have a number of important ramifications, the most important being that the number of faint clusters continues to rise down to at least  $M_V \approx -7$ . This provides a counter example to published claims that the initial cluster LF in some galaxies has a Gaussian-like distribution (e.g., de Grijs, Parmentier, & Lamers 2005; Anders et al. 2007), since this would require that essentially all the faint objects be individual stars. We will address this issue more fully in §6 below, when we examine the LF in more detail.

See Tables 4 & 5 and Appendix A.3 for more details concerning Training Set 3, and Appendix A.4 for an extension of this methodology to all of NGC 4038/39 covered by the ACS images.

## 5. Fifty Most Luminous, Massive, and IR-bright Clusters

In this section we compare the 50 most luminous (in  $V$ : Table 6), most massive (Table 7), and most IR-bright (in  $F160W$ : Table 8) clusters. Part of our motivation for doing so is to facilitate comparisons with other studies, since we suspect that at least some of the differing conclusions reached by various authors (see Introduction) result from excluding young clusters in crowded environments. In general these three sets are relatively disjoint, with the most luminous clusters tending to be the youngest (median  $\log \tau = 6.78$ ), the IR-bright clusters being older (median  $\log \tau = 7.57$ ; after removing those with questionable ages as indicated in Table 8), and the most massive clusters tending to be the oldest (median  $\log \tau = 7.84$ ).

Figure 9 shows the logarithmic age vs. mass diagram with circles marking the 50 most massive clusters. Note that there are some objects in the diagram with apparent masses that would qualify them for the top 50, but which have been excluded (i.e., are not circled in Figure 9 or included in Table 7) based on a visual review of the images and the two-color diagrams. These are caused by a variety of interlopers and artifacts (e.g., stars, galactic nuclei, incorrect extinction corrections). The fraction of artifacts is quite low up to values of  $\log \tau < 8.6$ , which will be used in the following sections as an upper limit to reliable age dating (e.g., when constructing the mass function). The most important artifact beyond this age is due to clusters that are probably quite young (e.g., are near regions with strong  $H\alpha$ , although they themselves do not have  $H\alpha$  emission) and are heavily extinguished by dust (e.g., are in the overlap region). The age-dating algorithm often classifies these as intermediate-age or old clusters due to their red colors and lack of  $H\alpha$  emission, hence giving them larger masses than they actually possess. This is the well-known age vs. extinction degeneracy. As

long as a cluster shows  $H\alpha$  emission ( $\log \tau < 6.8$ ) it is possible to break this degeneracy, but once there is no  $H\alpha$  emission, it is difficult to distinguish an intermediate-age cluster from a young cluster with strong extinction. Luckily, most young clusters expel most of the dust around them within about 10 Myr, hence it is primarily the clusters with extensive *foreground* extinction where this is a problem (i.e., in the overlap region).

Figure 10 shows all three sets of clusters (most luminous in blue, most massive in red, and most IR-bright in white). Note that the IR observations with NICMOS only cover about half of the field of view (see Figures 11 and 12). For this reason we only include the 25 most IR-bright clusters, so that at least in the regions which are covered in all three sets the density of points are similar and hence can be more easily compared.

As expected, the western loop (i.e., the right 1/3 of Figure 10a) has a higher number of luminous clusters (19 of 50) than of massive clusters (9 of 50) because of the predominance of young clusters in this region. Conversely, the area around Regions 4, 5, 6, and 7 and Knots E and F (i.e., in the vicinity below the red circle 34 in Figure 10a) has the highest number of massive clusters (19 of 50) compared to luminous clusters (11 of 50) because of the preponderance of intermediate-age clusters in this region. This implies that there has been more star formation in this region than anywhere else in the galaxy during the past few hundred Myr.

Figures 11 and 12 show the NICMOS F160W observations on the top (with and without positions marked by circles and rank order numbers), and the  $V$  observations on the bottom for comparison, for the two NIC-3 pointings. While most of the IR-bright objects have clear optical counterparts, there are a few IR-bright objects with relatively faint counterparts (i.e., 3, 16, 24, 28 in Figure 11 and 12, 18, 26 in Figure 12). There is only one object (12) out of the 50 with a marginal detection (i.e.,  $M_V = -5.58 \pm 0.30$ ; see Table 8). More quantitatively, only 8 of the 50 brightest IR-sources ( $16 \pm 6\%$ ) have values of  $A_V > 3$ , with the highest value being  $A_V \approx 7$  (assuming an intrinsic color of  $V - I = 0.5$  for all the clusters). This is in good agreement with the result by Whitmore & Zhang (2002) that 85% of the bright thermal radio sources have optical counterparts. *Hence, our optical sample is not missing a large fraction of clusters due to dust obscuration.*

## 6. Luminosity Function

In this section we utilize our new technique for differentiating clusters from stars based on a combination of size and color information, and we revisit the shape of the cluster LF in the main bodies of the Antennae. In Figure 13 we use a magnitude limit of  $M_V < -7$ , since

the completeness correction is  $\leq 50\%$  for this range. It also becomes difficult to distinguish the stars from clusters for fainter magnitudes (e.g., see Figure 7). We note that corrections have *not* been made for extinction when constructing the LFs, for reasons further discussed below. We also manually removed six bright “interlopers” (five foreground stars and the nucleus of NGC 4039) from the sample to insure that they do not artificially bias the bright end of the cluster LF.

Figure 13a shows the LF for all detected objects, i.e., for a *mix* of individual stars and clusters. Open symbols show the uncorrected data while filled symbols show completeness corrected data. To determine the slope of the LF via a least-squares fit, we restrict the range of the fit to  $M_V = -15$  to  $-7$  (or  $-15.2$  to  $-7.2$  if one accounts for a foreground extinction of  $A_V = 0.15$ ). This yields a good fit with a single power law,  $dN/dL \propto L^\alpha$ , where  $\alpha = -2.26 \pm 0.03$ . We next use what we have learned in §4 to produce subsamples designed to differentiate the clusters from the stars, to the degree possible. Figure 13b shows the result of using only the concentration index as a size criterion,  $C > 1.52$ . Figure 13c shows the result of using only a color criterion,  $U-B < 0.6$ , to select objects in cluster space or in blue-star/cluster space as shown in Figure 8. Figure 13d shows the result of using both the size and color criteria for clusters. This is our preferred cluster catalog and represents our “best guess” LF. As the figure demonstrates, the results of the various selections and fits are fairly similar, with values of the power-law index  $\alpha$  ranging from  $-2.26$  when using all objects to  $-2.13$  for our best LF. This reflects the fact that most of the objects, even at  $M_V = -7$ , are still clusters rather than stars.

The fits in Fig. 13 use variable bin sizes, where there are an equal number of clusters in each bin, since Maíz Apellániz (2008) finds that using the standard fixed-bin-size technique will artificially steepen a LF. We empirically confirm this bias, with the variable-bin method systematically giving slightly higher values of  $\alpha$  (i.e., flatter slopes), with a mean difference of  $\sim 0.1$ . In the cases below where comparisons are made with past values of  $\alpha$  derived from fixed binning, a correction of 0.1 is made. We use the variable-binning technique as our preferred method throughout the rest of this paper, although some later figures (e.g., Figure 15) show both techniques for comparison.

Figure 14 attempts to extract the *stellar* LF by restricting the sample to objects with  $C < 1.52$  and  $M_V < -10$  (the latter criterion to avoid foreground stars). As expected, for stars the slope is steeper, with  $\alpha = -2.47 \pm 0.04$ .

The possibility of a bend (at the few- $\sigma$  level) in the cluster LF obtained from WFPC2 data was discussed by Whitmore et al. (1999). The new ACS data do not appear to show any similar bend. More specifically, if we break the total luminosity range for clusters into two segments ( $-15 < M_V < -10.4$  and  $-10.4 < M_V < -7$ ), and use the  $U - B < 0.6$



criterion for distinguishing clusters, we find power-law exponents of  $\alpha = -2.22 \pm 0.17$  and  $\alpha = -2.23 \pm 0.02$ , respectively. Hence, we do not find supporting evidence for any bend or break in the LF of star clusters in the Antennae when using the new, higher-quality ACS observations.

These results contradict recent claims for a turnover in the Antennae cluster LF, based on a re-analysis of our WFPC2 data (Anders et al. 2007). Clearly, the much deeper and higher-resolution ACS data show no evidence for a turnover, even if we restrict our sample to only include resolved objects. The peak found near  $M_V \approx -8.5$  mag by Anders et al. appears to be caused by the introduction of a selection criterion that requires objects to have a  $U$ -band photometric uncertainty of  $\sigma_U \leq 0.2$  mag. While completeness corrections could compensate for this effect in principle (as Anders et al. 2007 attempt to do), in practice it is difficult to accurately model the completeness of a cluster system as complicated as the Antennae’s. Using the Anders et al. technique, even a very small mismatch in the true vs. estimated completeness corrections can result in an apparent turnover near the completeness threshold, which appears to have happened in their analysis.

We search for any hint of a flattening of the cluster LF at the faintest magnitudes by attempting to extend the fits to  $M_V = -6$ , at the risk of pushing the completeness corrections to where they become large. At the bright end we use a restrictive cutoff of  $M_V = -11$  to increase the sensitivity of the least-squares fit to faint magnitudes. Using the  $U - B < 0.6$  criterion for clusters, since the  $C > 1.52$  criterion becomes unreliable beyond  $M_V = -7$ , we find values for  $\alpha$  that run from  $-2.24 \pm 0.04$  (for  $M_V = -11$  to  $-8$ ) to  $-2.22 \pm 0.03$  ( $M_V = -11$  to  $-7$ ) to  $-2.13 \pm 0.02$  ( $M_V = -11$  to  $-6$ ). Hence, we find weak evidence for a potential small amount of flattening of the cluster LF beyond  $M_V = -7$ . However, due to the greater dependence on the completeness correction at these faint light levels, we consider this result very uncertain.

A note on error estimates for the power-law index  $\alpha$  is in order. While the formal internal statistical errors typically are quite small (e.g., 0.03 for the entire sample when a wide range in magnitudes is used, as shown in Figure 13), they do not include a number of possible errors, both internal and external (e.g., deficiencies in cluster-finding algorithms and uncertainties in background and completeness corrections). A more realistic approach to determining actual errors is to compare the scatter in a variety of determinations. For example, using the four methods shown in Figure 13 yields a mean  $\bar{\alpha} = -2.20$  (rms = 0.05). If we divide the Antennae into three pieces: NGC 4039 ( $\alpha \approx -2.17$ ), the overlap region between the two galaxies ( $\alpha \approx -2.15$ ), and the western half of NGC 4038 ( $\alpha \approx -2.18$ ),  $\bar{\alpha} = -2.17$  (rms = 0.02). A comparison between an extinction-corrected LF with  $\alpha = -1.99$  (WFC07) and an uncorrected LF with  $\alpha = -2.07$  (Whitmore et al. 1999; down to  $M_V = -9$ ), both using

WFPC2 data, yields a value of  $\bar{\alpha} = -2.03$  (rms = 0.06). Note that including a correction for extinction has the problem that the faint end of the LF is automatically underpopulated due to the lack of objects below the completeness threshold, hence artificially flattening the LF. For the purposes of the current exercise, we make the comparison between extinction-corrected and uncorrected values only down to a value of  $M_V = -9$  in order to minimize the effect. Throughout the rest of this paper we use uncorrected LFs.

Taking an average of all the different methods discussed in this section, our estimate for the slope of the cluster LF,  $dN/dL \propto L^\alpha$ , is  $\bar{\alpha} = -2.17$  (rms = 0.07), based on an ensemble with 14 separate trials. This is quite similar to our single best ACS value of  $\alpha = -2.13 \pm 0.03$  from Figure 13d. We adopt the latter value as our best guess value, but use the rms value of 0.07 from the ensemble for our error estimate.

These results are in reasonably good agreement with our earlier WFPC2 results of  $-2.07 \pm 0.06$  (Whitmore et al. 1999; down to  $M_V = -9$ ) and extend the luminosity range by  $\sim 2$  magnitudes.

## 7. Mass and Age Distributions for Clusters in the Antennae

We previously studied the mass and age distributions for star clusters in the Antennae using the WFPC2 observations (Zhang & Fall 1999; FCW05; WCF07; FCW09). Here, we use the higher-resolution ACS images plus our new ability to separate clusters from stars to assess the accuracy and extend the range of our earlier results.

### 7.1. Mass Distributions

The mass function for a population of star clusters provides important information on the formation and dynamical evolution of the clusters, and in principle is more straightforward to interpret than the luminosity function, where the dimming of older clusters can affect the slope. A comparison between the mass and luminosity functions can yield insights into the age distribution of the clusters as well as the processes responsible for the formation and dissolution of clusters. However, it is important to keep in mind that mass is a derived property, introducing additional biases and uncertainties. Hence we must be careful to only use it in age and mass ranges that are reliable.

The top three panels of Figure 15 show the mass functions for cluster candidates (i.e.,  $M_V < -9$ ) in the Antennae in three intervals of age,  $\log \tau < 7.0$ ,  $7.0 \leq \log \tau < 8.0$ , and  $8.0 \leq \log \tau \leq 8.6$ . The corresponding lower mass limits range from  $10^4$  to  $10^5 M_\odot$ ,

respectively, as shown by the dashed red lines in Figure 9.

The bottom panels show the mass functions in the same intervals of age, but with only resolved objects selected (i.e.,  $C > 1.52$ ). Each panel shows the mass function resulting from two different bin selections: our preferred version with variable bin sizes, where there are an equal number of clusters in each bin (filled circles), and a version with approximately fixed bin sizes (open circles).

We find that over the plotted mass-age range, the mass function declines monotonically, with no evidence for a flattening or a peak. Similarly, we do not see any obvious steepening of the mass function at the high mass end as suggested by Gieles et al. (2006), which would be expected if there was a physical cutoff to the masses with which clusters can form. Hence, the mass functions for clusters in the Antennae can be described by a single power-law of the form  $dN/dM \propto M^\beta$  (or  $dN/d\log M \propto M^{\beta+1}$  plotted logarithmically). The solid lines are best fits to the variable-binning data (filled circles), while dashed lines are fits to the fixed-bin data (open circles). The values of  $\beta$  given in Figure 15 are for the variable-bin data, and the mean value for the six panels is  $\bar{\beta} = -2.10 \pm 0.13$ . A more realistic value for the uncertainty in  $\beta$  is 0.2, based on the discussion of uncertainties in  $\alpha$  (§6) and the fact that the mass is a derived property, thus introducing additional artifacts and uncertainties (e.g., uncertainty in the metallicity).

The results presented here confirm and extend those based on previous WFPC2 data (Zhang & Fall 1999; FCW09). We find that the mass function continues as a power-law with  $\beta \approx -2$  to lower masses (i.e.,  $\sim 10^4 M_\odot$  for ages  $< 10^7$  yrs) and to older ages ( $\sim 3 \times 10^8$  yr for  $> 10^5 M_\odot$ ) than reported previously. This has a number of physical implications, which are discussed in detail in FCW09. In particular, the shape of the mass function does not change for the first  $\sim 3 \times 10^8$  yr over the observed mass-age range, at least within the uncertainties, which constrains various models for cluster disruption.

Figure 16 shows the MFs (top row) and LFs (bottom row) for four of the  $\sim 0.5$  kpc-size areas that will be discussed in §8. In general, the indices  $\alpha$  and  $\beta$  are essentially the same within the errors, as already found for the entire distribution of objects in the Antennae (i.e.,  $\alpha = -2.13 \pm 0.07$  and  $\beta = -2.10 \pm 0.20$ ). Fall (2006) shows that this similarity between the cluster LFs and MFs is only expected if the MF is a power law, and if the cluster age and mass distributions are approximately independent of one another.

## 7.2. Age Distributions

The shape of the age distribution for star clusters provides clues to the formation and survival of the clusters. We previously found, based on WFPC2 data, that the age distribution of star clusters in the Antennae declines more or less continuously and in approximately power-law fashion,  $dN/d\tau \propto \tau^\gamma$ , with  $\gamma \approx -1.0$  for the first few  $10^8$  yr. We also found that the shape of  $dN/d\tau$  was similar in two different intervals of mass (FCW05, WCF07, FCW09), suggesting that the age distribution does not depend strongly on the mass of the clusters. Here we confirm and extend these two important conclusions, using the higher quality ACS data and the results from our detailed investigation of the 50 most massive clusters in the Antennae. A more detailed treatment will be presented by Chandar et al. (in preparation).

The cluster age distribution is the result of a combination of formation and disruption processes. A value of  $\gamma = -1$  for the shape of the age distribution implies that there should be equal numbers of clusters in equal bins of  $\log \tau$  above a given mass, which means that there are approximately ten times fewer clusters each subsequent decade in  $\log \tau$ . If we assume that the star formation rate (SFR) is roughly constant, this implies a 90% cluster disruption rate each decade in  $\log \tau$ . While the assumption of a constant SFR is clearly an oversimplification, especially for merging galaxies where bursts of star formation are expected, the rapid drop in  $dN/d\tau$  by two orders of magnitude from 5 to 500 Myr, when compared to the predicted increase in the SFR from a model simulation of the Antennae (a factor of a few, see Mihos et al. 1993), suggests that the dominant influence for understanding the demographics of clusters are disruption processes rather than fluctuations in the formation rate. Other arguments supporting this conclusion are presented in FCW05 and WCF07. Specifically, the  $dN/d\tau$  diagram declines in a similar fashion throughout the Antennae (see Figures 8 and 9 in WCF07), even though there are no hydrodynamical processes that could synchronize the formation rate of the clusters this precisely over such large separations. In addition, the  $dN/d\tau$  diagram looks similar in many star forming galaxy (see WCF07, Mora et al. 2009, Chandar et al. 2010a, 2010b).

In WCF07 our best-fit model for the Antennae clusters suggested an infant mortality rate of  $\sim 80\%$  per  $\log \tau$  decade, corresponding to a value of  $\gamma \approx -0.7$ , which is only slightly flatter than the canonical value of  $-1$  discussed above.

Recently, Bastian et al. (2009) have attempted to take into account variations in the star formation rate in the Antennae when interpreting the cluster age distribution, by adopting the star formation rate found in the simulation by Mihos et al. (1993). This is an interesting approach. Yet, it is limited by the large uncertainties imposed by our lack of understanding of the star-formation process (e.g., shock-induced vs. density-induced star formation, see Barnes 2004), the fraction of gas in the progenitors, etc. Perhaps most worrisome in using

the Mihos et al. (1993) model for the Antennae to predict the varying SFR is the fact that according to this model most of the star formation should occur in the nuclear regions, while in reality most of it is currently distributed throughout the disks of the two galaxies. A new N-body/SPH simulation by Karl et al. (2010) predicts more distributed star formation, similar to the observations, and has a nearly constant SFR in the age range  $6.7 < \log \tau < 8.7$ , in contrast to the Mihos et al. (1993) model where the SFR increases a factor of a few. This demonstrates the large uncertainties involved with making these simulations, and hence in using the Bastian et al. approach for estimating the cluster dissolution rate.

Probably the best approach for determining the disruption rate of clusters will be to combine the data from a much larger sample of galaxies, especially non-interacting spiral galaxies, where the assumption of a roughly constant SFR is better justified statistically. The recent study by Mora et al. (2009) provides a promising start in this direction. Using *HST* imaging, they found power-law age distributions for star clusters in five nearby spiral galaxies. Although they used a somewhat different technique, counting clusters brighter than a given  $V$  band luminosity rather than above a given mass, they found that the age distributions are all consistent with  $\approx 80\%$  of the clusters being disrupted every decade in age for  $\tau \lesssim 10^9$  yr, nearly identical to our results for the Antennae (see their Figure 15).

Table 7 lists the 50 most massive star clusters found in the present study of the Antennae. We can use its data to derive a mass-limited ( $\log M > 5.8$ ) age-distribution up to  $\log \tau = 8.6$  (i.e., limited by artifacts that manifest themselves at higher ages; see discussion in §5). Making the first-order assumption of a roughly constant SFR during this period, a value of  $\gamma = -1$  would imply that there should be approximately equal numbers of clusters in the three intervals  $\log \tau = 6-7$ ,  $7-8$ , and  $8-9$ , while a value of  $\gamma = -0.7$  (i.e., the preferred value from WCF07) would imply a factor of 2 increase for successive intervals. Counting the clusters in Table 7, we find that the above three age intervals contain 10, 19, and 45 clusters (extrapolating from a logarithmic range  $8-8.6$  for the last bin), respectively, in good agreement with the prediction from an 80% disruption model with roughly constant SFR.

Because Table 7 contains only 50 clusters, thus leading to low number statistics, we also checked the number of clusters in a second range of masses,  $5.3 \leq \log(M/M_\odot) \leq 5.7$ . Here we find that the three age intervals  $\log \tau = 6-7$ ,  $7-8$ , and  $8-9$  contain 28, 41, and 126 clusters, respectively. Hence the lower mass clusters have a similar age distribution as the higher mass clusters, increasing in number by approximately a factor of 2 in successive unit intervals of  $\log \tau$ , as predicted from an 80% disruption model with roughly constant SFR.

To conclude, our new results confirm that the number of massive star clusters in the Antennae increases only slightly in bins of  $\log \tau$  and, therefore, must decline fairly steeply as a function of linear  $\tau$ , with an index of  $\gamma \approx -0.7$ . We have interpreted this steep decline

as being primarily due to the disruption, rather than the formation, of clusters (see also FCW05; WCF07; FCW09). In addition, the similarity of the relative numbers of clusters in different age intervals, but at different masses, also supports the idea that any disruption that affects these clusters does so in a manner nearly independent of the cluster mass, at least for the first few  $10^8$  yr.

## 8. Area-by-Area Analysis

In this section we examine selected areas in the Antennae. Three different sets of areas have been selected for study, as shown in Figure 17. The first set consists of the bright star forming “knots” first identified by Rubin, Ford, & D’Odorico (1970). These are labeled by letters A, B, C, through T. The second set consists of less prominent, more extended star forming regions similar to the “other regions of interest” first identified by Whitmore & Schweizer (1995). These “regions” are labeled by numbers 1–16. The third set consists of areas in the outer parts of the galaxy (e.g., tails and loops). These are labeled as Outer 1, Outer 2, . . . , Outer 10. Table 9 collects information for each of the knots, regions, and outer areas.

In the following, we include all objects in our analysis rather than trying to select only clusters. This choice is based on the similarity we found in the results for the luminosity functions (Figure 13) between the various methods of selecting clusters and the total sample, and is—ultimately—due to the fact that most of the objects in our list are clusters down to at least  $M_V = -7$ . Specifically, we do not wish to eliminate objects with  $C < 1.52$  because many of them are unresolved young clusters, as seen from their position in cluster or blue-star/cluster space (§4). Repeating the analysis using, for example, a  $C > 1.52$  size criterion, results in only minor differences.

### 8.1. General Properties

We begin by examining general trends in the properties of the selected areas and then discuss possible physical interpretations for these trends. Some of the most prominent correlations for clusters in the selected areas are shown in Figure 18. The top left panel shows the  $M_V(\text{brightest})$  vs.  $\log N$  diagram, where  $M_V(\text{brightest})$  is the absolute magnitude of the brightest cluster in each area and  $\log N$  is the number of clusters brighter than  $M_V = -9$  in that area. This is the strongest correlation ( $8\sigma$ -level of significance) of those shown in the figure. A version of this diagram for cluster populations in entire galaxies was first shown

by Whitmore (2003) and has been subsequently studied by several other authors (Larsen 2002; WCF07; Bastian 2008; Larsen 2009). The diagram was one of the primary drivers in developing the “universal” cluster demographics model described in WCF07, since the observed correlation can be explained by a statistical “size-of-sample” effect, assuming all young cluster systems in galaxies have power-law LFs with a value of  $\alpha \approx -2$ . A comparison of the data from our area-by-area analysis with the best-fit line for cluster populations in entire galaxies (mergers, starbursts, dwarfs, spirals) from WC07 (dotted line) shows that the relationship is essentially identical. This again provides evidence for a universal relationship, at least down to the  $\sim 0.5$  kpc scales we have studied here.

The second best correlation is the  $\log E(B-V)$  vs.  $\log \tau$  relation shown in Figure 18b ( $7\sigma$ -level of significance). This is similar to the result from Figure 10c in Whitmore & Zhang (2002), but we now use the median value of  $\log E(B-V)$  for clusters within a defined area instead of plotting values of  $\log E(B-V)$  for individual clusters. Similar results have also been found by Bastian et al. (2005) for M51 and Mengel et al. (2005) for the Antennae. Using areas instead of individual clusters, we find a typical  $E(B-V)$  value of  $\sim 0.3$  mag (i.e.,  $A_V \approx 1$  mag) for areas dominated by the youngest clusters with logarithmic ages (in years)  $\log \tau \approx 6.5$ , declining to values of  $E(B-V) \approx 0.1$  mag ( $A_V \approx 0.3$  mag) for areas with logarithmic ages  $\log \tau \approx 8.0$ .

Figures 18c and 18d show values of  $\alpha$  (the slope of the LF) and  $\beta$  (the slope of the MF) as a function of the median age of the clusters in each region. We first note that for ages greater than  $\log \tau = 7$ , the slope values are relatively constant, and the mean values of  $\alpha$  and  $\beta$  are roughly equal within the uncertainties (i.e.,  $\bar{\alpha} = -2.12 \pm 0.04$  (rms = 0.17) and  $\bar{\beta} = -2.09 \pm 0.06$  (rms = 0.24)). This is similar to what we found for the total distributions of clusters in the Antennae, as discussed in §7.1, and provides further evidence that the mass and age distributions are independent of each other, as discussed in Fall (2006).

Figures 18c and 18d also show tentative evidence for flatter slopes for  $\alpha$  and  $\beta$  when  $\log \tau < 7$ . However, it is possible that this is due to observational biases, for example difficulties in making completeness corrections for the youngest clusters, which tend to lie in areas of higher background brightness. In principle, our completeness corrections should take care of this effect, but the combination of high background and severe crowding makes this task more difficult. Another potential problem is extinction, since fainter clusters might suffer more extinction than highly luminous clusters due to their lack of massive stars needed to clear out the surrounding dust. We can test for this hypothetical effect fairly easily by comparing the colors of the bright and faint clusters. This comparison shows that a very small effect does exist (i.e.,  $-0.02$  mag in  $U-B$  when comparing clusters in the knots brighter than  $M_V = -10$  with those in the range  $M_V = -10$  to  $-9$ ), but this effect is too small to

cause more than a very minor difference in the LFs.

## 8.2. Area-by-Area Analysis of Outer Areas

One of our primary goals for the outer areas, where the background is very low, is to push the LF to  $M_V \approx -6$ . This is particularly interesting because most of the clusters in these regions have intermediate ages, having probably been formed during the first encounter between the two galaxies (e.g., see Figure 17 of Whitmore et al. 1999). We should therefore be able to search for a possible turnover in the LF that is expected to eventually appear if the power-law form of the LF for young clusters evolves dynamically—assuming evaporation processes typical of the Milky Way—to the peaked form found for old globular clusters. Based on Fall & Zhang (2001) we might expect this turnover to occur around  $M_V \approx -4$ , assuming that most of the outer clusters are 100–300 yr old and that two-body relaxation is the dominant process.

Figure 19 shows the data and values of  $\alpha$  for the best fits for the three outer areas with the most clusters (Outer 2, 5, and 7). We find no clear evidence for a turnover in the LFs of the cluster population in the tails, consistent with an extrapolation from the Fall & Zhang (2001) model.

## 9. Patterns of Star Formation

Star formation in merging galaxies is sometimes considered to be quite chaotic, with gas clouds slamming into one another at hundreds of  $\text{km s}^{-1}$ . The “overlap region” in the Antennae is often quoted as a prime example. Yet, the periods and locations of violent interaction are relatively short-lived, being most pronounced during closest approaches. Hence, during much of a merger’s evolution the distortions imposed by the interaction are less dramatic, resulting in a number of well defined patterns, both large- and small-scale (e.g., Renaud et al. 2009). These patterns can provide important clues to the processes of star and cluster formation.

### 9.1. Large-Scale Patterns

On the largest scales, a number of long “linear” (or gently curved) features can be discerned in the Antennae. The most obvious examples are the two long tidal tails ( $\sim 130$  kpc in projection tip to tip) that give this system its nickname. Most of the clusters in the



inner parts of these tails (the only parts covered by the central pointings; results from outer pointings along the tails will be reported in a future paper) have ages of roughly 200 Myr and were probably formed during the first-pass encounter between the two galaxies. However, an intriguing feature is the existence of ongoing star formation at a low level, as evidenced by the existence of about a dozen faint H $\alpha$  knots strung along the inner edge of the southern tail near its base, where it connects to the disk of NGC 4038 (i.e., Outer 5, see Figures 17 and 20a).

A possible continuation of this feature is the increasingly strong H $\alpha$  “streak” seen passing through knots N and P and extending to the “Western Loop” that includes knots G, R, S, T, M, and L (Figure 20b and 17). A faint but, again, increasingly strong dust lane is associated with this H $\alpha$  emission. In the outer regions it is first aligned with the H $\alpha$  knots themselves, but further into the galaxy it becomes offset to the inside of the H $\alpha$  emission. A similar trend in alignment between H $\alpha$  emission and dust is observed in M51. In fact, this whole aligned feature of H $\alpha$  emission plus dust lane in the Antennae is reminiscent of, though perhaps less regular than, the spiral arms and outer tidal features in M51.

Similar large-scale features are the “spiral-looking tail” in Region 1 (Figure 20e;  $\sim 3.4$  kpc) and the long (Figure 20c;  $\sim 8.2$  kpc) dust lane running from the bottom of Outer 6 through Outer 3 and Outer 2, to near the end of Outer 1. A less prominent example is the nearly linear string of giant H II regions following a line from Knot F to E to Region 3 (Figure 20d). This nearly straight string was used to good advantage by Whitmore et al. (2005), who aligned the long-slit of the STIS spectrograph with it. This string also forms the eastern edge of the overlap region. Hence, its apparent regularity in both morphological linearity and a smooth velocity field, suggests that even the overlap region might be less chaotic than commonly believed.

Several other linear features are seen on slightly smaller scales. Examples are the two linear dust lanes that run from near the nucleus of NGC 4038 out to Regions 13 and 14 (Figure 20f), respectively, with regions of prominent star formation along one edge of each dust lane (e.g., Knot L). The side-by-side arrangement of star formation and dust lanes is reminiscent of normal spiral arms (although the linear rather than spiral arrangement is not typical).

Note that while clusters form currently at the highest rate in the chaotic overlap region, other clusters are also forming throughout most of the two galaxies. In particular, the velocity pattern of the ionized gas in most of the northern half of NGC 4038 is quite regular (Amram et al. 1992), yet a large fraction of the clusters are forming in this region at the present time. Hence, high collision velocities are not required for making clusters, a result also found by Zhang et al. (2001) and Whitmore et al. (2005), and supported by theory

(Renaud et al. 2008).

## 9.2. Small-Scale Patterns—Evidence for Sequential Star Formation

While the specific details of how star formation is triggered may still be obscure, it is clear that compression and shocks play an important role (e.g., along spirals arms). One method for studying triggered star formation is to age-date stars or star clusters and then look for patterns that might indicate the presence of sequential star or cluster formation. A classic example of this is 30 Doradus, where Walborn et al. (1999) found evidence for several generations of star formation. Does our age-dating of clusters in the Antennae provide similar evidence of sequential cluster formation?

Figure 21 shows the pattern of ages obtained for clusters in Knot S, along with an  $H\alpha$  image of Knot S. There is some evidence for triggering as shown by the preponderance of 5–10 Myr clusters (green circles; including the central dominant cluster) positioned in what appears to be a hole in the  $H\alpha$ . The younger clusters (blue circles) are primarily to the left, as the star formation apparently works its way into the dust reservoir (see the ACS/HRC image in Figure 28). There is also a smaller region of triggered formation in the upper right, as evidenced by both the age dating and presence of  $H\alpha$  in that area. We also note a scattering of older clusters throughout much of the region with ages 10–100 Myr (red circles), which may have triggered earlier episodes of star formation in this region.

Knot B (Figure 22) presents a similar, but even more dramatic example of triggered cluster formation. In this case we find a single cluster with an apparent age of  $\sim 50$  Myr (and a mass of  $\sim 10^6 M_\odot$ ) located off to the right side, but also a population of younger clusters with a total mass of  $\sim 8 \times 10^6 M_\odot$ , about *eight times greater than the mass of the cluster that appears to have triggered their formation*. Note that the  $H\alpha$  shell is centered on the older cluster and that the young clusters are located where the shell intersects a major dust lane at the edge of the overlap region (see Figure 1). Dividing the radius of the  $H\alpha$  bubble by the age of the central cluster yields an expansion velocity of  $\sim 6 \text{ km s}^{-1}$ . This is smaller than values of 20–30  $\text{km s}^{-1}$  derived for the bubbles in knots S and J by Whitmore et al. (1999), and than the direct measurements of  $H\alpha$  velocities by Amram et al. (1992). One possibility is that the age of this cluster is closer to 10–20 Myr, which lies in the range that is hard to measure (see Figure 9 and discussion in Whitmore et al. 1999). This slightly smaller age would give expansion velocities in the range 15–30  $\text{km s}^{-1}$  and would also be more compatible with the age gradient shown in Figure 22. Presumably, the dust lane in the overlap region provides a much greater reservoir of raw material needed to form massive clusters than is the case for Knot S. An analogy might be that a match dropped on a field of

dry grass might only result in a few minor brushfires, but a match dropped next to a tinder box can result in a much more impressive, explosive fire (e.g., Knot B).

In general, early star formation tends to occur on the edges of gas reservoirs and then work its way into the dust lanes, creating a linear rather than circular gradient of sequential star formation. This is sometimes known as the “blister model” (Israel 1978). Several other knots and regions in the Antennae (e.g., knots A, E, F, K, L, and T; and regions 3, 4, and 13) have this linear morphology of sequential cluster formation with the gradient in the direction toward a major dust lane, as shown in Figure 23 (e.g., knots E & F and region 13). We note, however, that similar morphologies might also result from large-scale processes such as a density wave or collision between two large gas clouds. In fact, it is likely that both large- and small-scale triggering is happening simultaneously.

Another interesting case is a dark, relatively circular dust cloud with a small amount of star formation on only one side of the cloud that is found near Outer 3 (see Figures 20g and 20c) in the southern outskirts of NGC 4039. The lack of an obvious trigger in this case suggests the possibility that the cloud is falling back into the galaxy and the star formation results from the ram pressure being exerted by the interstellar medium. Perhaps velocity measurements with ALMA will be able to test this hypothesis. This appears to be a relatively unique case in the Antennae, but we note that other examples may be harder to discern due to the geometry of their encounter. One possible second case might be near the center of Knot N, with a dust cloud falling back into the galactic disk along our line of sight (see Figure 20b).

## 10. Conclusions

The Advanced Camera for Surveys on *HST* was used to obtain high-resolution images of NGC 4038/4039, which allow us to better differentiate between individual stars and compact star clusters. We have used this improved ability to extend the cluster LF by approximately 2–3 mag at its faint end, when compared to the previous WFPC2 photometry. In addition, the Near Infrared Camera and Multi-Object Spectrometer (NICMOS) was used to help study the clusters still largely embedded in dust. Following are our main results:

1. The cluster luminosity function continues as a single power law,  $dN/dL \propto L^\alpha$ , with  $\alpha = -2.13 \pm 0.07$  down to the current observational limit of  $M_V \approx -7$ . This value is uncorrected for extinction and based on variable-binning fits. Similarly, the cluster mass function is a single power law  $dN/dM \propto M^\beta$  with  $\beta = -2.10 \pm 0.20$  for clusters with ages  $< 3 \times 10^8$  yr, corresponding to lower mass limits that range from  $10^4$  to  $10^5 M_\odot$ , depending

on the age range of the subsample. Hence the power-law indices for the luminosity and mass functions are essentially the same.

2. The LF for intermediate-age clusters (e.g.,  $\sim 200$  Myr old clusters found in the loops, tails, and outer areas) does not show any hint of a turnover down to  $M_V \approx -6$ . This is consistent with relaxation-driven cluster disruption models, which predict the turnover should not be observed until  $M_V \approx -4$  for this age range.

3. The brightest individual stars in the Antennae reach absolute visual magnitudes of  $M_V \approx -9.5$ , a limit compatible with the so-called Humphreys–Davidson (1979) limit observed in the Milky Way and nearby galaxies (see Appendix A for details).

4. Our photometrically determined cluster ages are in good agreement with spectroscopically determined ages from Bastian et al. (2009) for 13 of the 15 clusters in common. In the other two cases, spatial resolution effects are likely to be responsible for the age differences, since the ground-based spectroscopic observations contain light from a much larger area than our *HST* measurements.

5. An area-by-area analysis shows a strong correlation between the absolute magnitude of an area’s brightest cluster,  $M_V(\text{brightest})$ , and the (logarithmic) number of clusters brighter than  $M_V = -9$  in that area,  $\log N$ . The  $M_V(\text{brightest})$  vs.  $\log N$  diagram for all areas of the Antennae studied is essentially identical to the corresponding diagram for entire galaxies, supporting the universality of this observed trend on a scale of a few hundred pc and larger. In addition, the reddening vs. age correlation found for individual clusters by Whitmore & Zhang (2002), Mengel et al. (2005), and Bastian et al. (2005) has been confirmed for the area-by-area analysis as well.

6. The same area-by-area analysis also reveals a tentative discovery of a new relationship between the power-law exponent  $\alpha$  of the LF and the median age of clusters in each area, in the sense that younger clusters have flatter LFs (i.e., values of  $\alpha \approx -1.8$  for the youngest star- and cluster-forming knots and  $-2.1$  for the outer areas). However, it is possible that this is caused by observational biases. The power-law indices for the LFs and MFs are in good agreement, and are similar to the results for the total population of clusters in the galaxy.

7. Using our age and mass estimates of clusters in the Antennae, we have found evidence of sequential cluster formation in several regions. Often there is a massive, somewhat older cluster which appears to have triggered the formation of younger, lower-mass satellite clusters. The area around Knot B is a particularly dramatic example of triggered star cluster formation, with evidence for one massive ( $\sim 10^6 M_\odot$ ) cluster, with an age in the range 10–50 Myr, having triggered the formation of several younger massive clusters (up to  $5 \times 10^6 M_\odot$ )

in the direction of a strong dust lane, with an amplification factor of  $\sim 8\times$  in the total mass of triggered clusters.

8. NICMOS observations show that  $16 \pm 6\%$  of the clusters in the Antennae are still largely embedded in their dust cocoons, with values of  $3 \lesssim A_V \lesssim 7$  mag. However, the top 50 IR-bright clusters *all* have optical counterparts in the much deeper ACS observations, hence the effect on our optically-based catalog derived from deep ACS images is minimal.

In conclusion, the results presented here confirm and extend those based on previous WFPC2 data (e.g., Whitmore et al. 1999, Zhang & Fall 1999, Whitmore & Zhang 2002, FCW05, WCF07, FCW09). In addition, similarities between our results for the Antennae and those for a growing number of other star-forming galaxies (e.g., Mora et al. 2009) support the universality model for the formation and disruption of star clusters.

We thank Stéphane Charlot for making the CB07 population-synthesis models for *HST* passbands available ahead of publication, and Lars Christensen for the use of his beautiful color image of the Antennae. We thank Mike Fall, Nate Bastian, Mark Gieles, and Soeren Larsen for helpful discussions and comments on the manuscript. We also thank an anonymous referee for several comments that helped improve the paper. Support for Program GO-10188 was provided by NASA through a grant from the Space Telescope Science Institute, which is operated by the Association of Universities for Research in Astronomy, Inc., under NASA contract NAS5-26555.

## Appendix

### A. Differentiating Stars and Clusters in the Antennae

With their higher spatial resolution across the entire field of view when compared to earlier WFPC2 data, our new ACS data provide a better opportunity for separating individual stars from clusters. In this Appendix we describe in some detail three “training sets” designed to help teach us how to achieve this separation. These three training sets consist of objects in: (1) an area dominated by foreground stars and old globular clusters; (2) one dominated by intermediate-age clusters; and (3) one containing a crowded mix of young stars and clusters.

### A.1. Training Set 1 – Isolated Foreground Stars vs. Old Globular Clusters

Training Set 1 includes reddish and yellow-red objects ( $V - I > 0.5$ ) in relatively low-background areas around the edges of the visually luminous galaxy disks. Most of these objects were identified as candidate foreground stars of our Galaxy in Table 4 of Whitmore et al. (1999). We contrast this set of 26 candidate stars with the 11 candidate old globular clusters from Table 3 of Whitmore et al. (1999). Information about the candidate foreground stars is given in Table 1. Information on the 11 candidate old globular clusters used as part of Training Set 1 is included in Table 2 (top group).

Figure 6a shows a plot of the absolute magnitude  $M_V$  vs. the concentration index  $C$  (i.e., the difference in magnitude using 1 and 3 pixel radius apertures) for the candidate foreground stars and old globular clusters of Training Set 1. We find that in general there is good separation between the two samples, with all of the candidate foreground stars lying in the range  $1.37 < C < 1.52$  ( $\bar{C} = 1.448$  mag, sample rms = 0.049 mag) and all but two of the candidate old globular clusters lying in the range  $1.62 < C < 1.78$  ( $\bar{C} = 1.676$  mag, rms = 0.052 mag). Note that the discrepant concentration indices for two of the candidate old globular clusters were already known (#1 and #9 in Table 2, corresponding to #8 and #1, respectively, in Table 3 of Whitmore et al. 1999), but the objects were retained since they had colors appropriate for old globular clusters.

The measured  $U - B$  and  $V - I$  colors for our training-set objects are compared with a CB07 evolutionary track for a model star cluster in Figure 6b. Note that only about half of the candidate stars (open circles) are detected in the  $U$  filter and can, therefore, be placed on this diagram. Most of the candidate globular clusters (filled circles) fall very close to the CB07 model predictions. There is only one discrepant object (#1) which falls well below the track, where most of the candidate stars rather than globular clusters are found. Hence object #1 is likely to be a star, based on both its color and its small value of  $C$ . The other globular cluster candidate (#9) that has a value of  $C$  overlapping with those measured for individual stars has colors that are indistinguishable from those of other old globular clusters. Turning our attention to the candidate stars, we find that all but two lie in the bottom-right part of the two-color diagram, well separated from the globular clusters. While most of the candidate stars and globular clusters are separated in the two-color diagram, it is clear that *some* stars can have colors similar to old globular clusters (typically early F-type stars). Hence, we can use a combination of size and color information to more reliably differentiate between stars and clusters. The dotted line in Figure 6b shows the region of the  $U - B$  vs.  $V - I$  diagram which we call “foreground-star space.”

Based on the results above, we include in Table 2 a new set of candidate old globular clusters (middle and bottom groups). The criteria used for their selection are: age estimates

in the range  $8.8 < \log \tau < 10$  (note that an examination of objects with estimated  $\log \tau > 10$  shows many of them to be either red foreground stars or distant background galaxies, hence our use of  $\log \tau < 10$ ), concentration indices in the range  $1.57 < C < 1.80$ , and locations away from regions with extensive dust (since a heavily reddened young cluster could masquerade as an old globular cluster).

## A.2. Training Set 2 – Isolated Intermediate-Age Clusters

The second training set consists primarily of intermediate-age clusters ( $\sim 200$  Myr) in what was defined as the Northwestern Extension in Figure 6 of Whitmore et al. 1999. This area is also designated as “Outer 9” in Figure 17. In a  $\sim 200$  Myr-old population, the brightest stars should have absolute magnitudes  $M_V \approx -3$ , well below our detection threshold. Hence, the vast majority of objects in this sample should be clusters, with perhaps a foreground star or two also included.

This area contains a loop of material that is believed to have been extracted from NGC 4038 at roughly the same time as the long tidal tails (Whitmore et al. 1999). The loop features three of the best examples of intermediate-age clusters (## 58549, 58909, and 59721 in Figure 24). These clusters turn out to have nearly identical properties, as shown in Table 3 (first three entries) and in Figure 25. The wide FOV of the ACS allows us to include many other clusters with similar properties. One likely bright foreground star (STAR-60076 in Figure 24) has been removed from the sample based on its small value of  $C = 1.389$ , although we note that it has colors similar to those of intermediate-age clusters. We recommend that a spectrum of this object be obtained to make a firm determination of its true nature.

Figure 7 shows the values  $C$  and  $\log \tau$  for the objects of Training Set 2, after the objects have been sorted into three subsamples according to their absolute magnitudes  $M_V$ . Note that all objects brighter than  $M_V = -8$  have values of  $C$  consistent with them being extended clusters, based on our results for Training Set 1 (i.e.,  $C > 1.52$ ). At fainter magnitudes we find that the increased observational scatter results in some estimates of  $C < 1.52$  and  $\log \tau < 8.0$ . Since we do not expect any intermediate-age stars in this region to have magnitudes brighter than our detection threshold, we interpret such values of  $C$  and  $\log \tau$  as being due to observational scatter, suggesting that the reliability of our  $C$  and age estimates is limited below  $M_V \approx -7$ . A supporting piece of evidence is that there is no  $H\alpha$  emission in this area, which would be expected if there actually were stars present with  $M_V \approx -7$  and  $\log \tau < 8$ . One other interesting result is the apparent correlation between  $M_V$  and  $C$  seen in Figure 7a, in the sense that brighter clusters tend to be larger, as might be expected.

Figure 25 shows the  $U-B$  vs.  $V-I$  diagrams for the objects of Training Set 2, again sorted by absolute magnitude. Note that the scatter for the three brightest clusters (crosses in top panel) is surprisingly small. We again find that a threshold of  $M_V \approx -7$  marks the point at which a relatively large fraction ( $\sim 20\%$ ) of the objects would be misclassified (i.e., are in regions of color-color space expected to be occupied only by stars). However, the midpoint of the color distributions remains about the same over the entire magnitude range. This shows that the objects are all very similar and, therefore, likely intermediate-age clusters. For example, we are not suddenly seeing a large percentage of blue or yellow/red stars. Note, however, that there is a small offset between the observations and the model tracks in Figure 25, with the midpoint of the data lying roughly 0.15 mag blueward of the tracks in  $V-I$ .

### A.3. Training Set 3 – Crowded Area of Knot S with both Stars and Clusters

The third training set consists of 23 objects around Knot S that were examined independently by four of us (BCW, RC, BR, and FS) with a variety of techniques that we have used to differentiate between stars and clusters in the past (e.g., visual examination using the IMEXAMINE tools in IRAF, varying contrasts on the DS9 display, circular shape, lack of nebulosity, etc.). This crowded area represents the opposite extreme from the areas containing Training Sets 1 and 2, with both the high density of objects and the high background level making size measurements more difficult. In general, the four independent assessments agreed at about the 85% level. Our final list of objects is based on the majority agreement from the independent assessments and consists of 12 candidate stars and 11 candidate clusters. Figure 26 shows the area around Knot S with the 23 objects marked while Table 4 includes information about the objects.

Next, Figure 27 shows the  $M_V$  vs.  $C$  and  $U-B$  vs.  $V-I$  diagrams for the objects of Training Set 3. Nine of the 12 candidate stars have concentration indices in the range  $1.37 < C < 1.52$ , appropriate for stars (see Figure 6). The one object (#20) below this range is the faintest one in the sample ( $M_V = -7.3$ ) and also lies within a few pixels of a very bright object. Hence the photometry for this object is suspect. This finding is consistent with our results from Figure 7, where we found that estimates of  $C$  and  $\log \tau$  for objects with  $M_V \approx -7$  were suspect even when the objects were isolated.

Another object (#18) has a much larger value of  $C$  than the other candidate stars and is almost certainly a cluster, based on its  $C$  value and the fact that it lies right on the CB07 evolutionary track in Figure 27, at an age of  $\sim 4$  Myr. This was one of the three objects in crowded subgroups added to the original sample of 20 training-set objects in order



to determine whether stars and clusters can be differentiated visually in this environment. While the correct assignments appear to have been made for the objects in the other two crowded subgroups (## 10 and 21, see Table 4), in the case of #18 the visual assignment of object type appears to have been incorrect.

All of the objects in Training Set 3 that were visually classified as clusters have values of  $C > 1.52$ , with a mean  $\bar{C} = 1.719$  ( $\sigma_1 = 0.082$ ) only slightly larger than that for the old globular clusters of Training Set 1. Hence, in general our visual classification agrees with the  $C$  criterion at the 80–90% level.

Figure 27b shows that only two of the 11 candidate stars (## 4 and 22, after having removed #18) lie below the CB07 model tracks in or near the region where young yellowish stars lie, as indicated by the small dots marking Padova models for stars brighter than  $M_V = -6$ . The remaining objects (e.g., ## 2, 5, 18, and 23) have colors expected for young clusters. Hence, *size alone is not always sufficient to differentiate between stars and clusters*. Many clusters are so compact that they remain indistinguishable from stars even at the improved resolution provided by ACS images. It is also possible that in some clusters the light from a single supergiant star dominates the light profile sufficiently so as to result in a smaller concentration index.

It is important to understand how an object gets to a position like #23’s in the  $U-B$  vs.  $V-I$  diagram of Figure 27, with a blue color in  $U-B$  ( $-0.68$  mag), but a yellow color in  $V-I$  ( $+0.62$  mag). A single star cannot have such colors, as shown by the Padova stellar models. What is needed is a combination of red or yellow supergiants, which dominate the light in  $V-I$ , and blue supergiants, which dominate the light in  $U-B$ . This composite nature of cluster light is the reason why clusters with ages from 5 to 8 Myr—when the earliest, most massive red supergiants appear—evolve so rapidly to the right, as is seen in the long horizontal stretch from  $V-I = -0.1$  to  $+0.8$  mag in the  $U-B$  vs.  $V-I$  diagram. The position of some candidate stars in this region of the diagram is indisputable evidence that they are actually clusters, masquerading as stars based on their small  $C$  due to the likely dominance of a single red or yellow supergiant (see, e.g., Drout et al. 2009 for a discussion of yellow supergiants).

Figure 8 shows two-color diagrams for all measured objects in and around Knot S, rather than just for the 23 objects of Training Set 3. The major conclusions based on these diagrams are discussed in §4. We wish to make an additional point here, related to the discussion above. While most of the resolved objects in the  $-10 < M_V < -9$  diagram hug the CB07 evolutionary track very nicely, five objects lie substantially to its left. We believe most of these are cases where there is a mixture of light from a young cluster with one (or perhaps two) individual very bright star(s), hence resulting in colors that are intermediate between

those of the cluster and stellar models. Ubeda et al. (2007) discuss this topic in their study of NGC 4214. This color “stochasticity” does not happen for the most luminous clusters ( $M_V < -10$ ) because such clusters have enough stars so that a few bright stars cannot greatly affect the total color. This has also been noted by other authors (e.g., Cervino, Valls-Gabaud, & Mass-Hesse 2002).

In Figure 8 we divided each two-color diagram into four regions: cluster space, foreground-star space, yellow-star space, and blue-star/cluster space. The first three follow from the discussion above. However, the fourth region, blue-star/cluster space, is more problematic, since both individual blue supergiants and the youngest clusters have similar colors according to the models (i.e., the upper-left regions of Figures 8 and 27b).

In principle, it should be possible to distinguish stars from clusters in this region of the two-color diagram based on their concentration index. However, as Figure 7 illustrates, the photometric uncertainties make this difficult for objects fainter than  $M_V \approx -7$ . Nevertheless, we note a clear statistical enhancement of objects in blue-star/cluster space for objects in the range  $-8 < M_V < -7$  in Figure 8. We suspect that this is indeed caused by the onset of a large number of young blue stars within this absolute-magnitude range (see §A.4 below for further discussion). A similar enhancement of yellow stars is not seen in yellow-star space, probably because the yellow supergiants are too faint to be observed in the  $U$  filter.

Figure 28 shows an ACS/HRC image taken as part of Proposal GO-10187, a study of Supernova 2004gt that went off in Knot S in 2004. The supernova is the very bright, red, and saturated object to the lower left of Knot S marked with a cross. The improved spatial resolution of the ACS/HRC provides an even better opportunity to distinguish between stars and clusters than do our dithered ACS/WFC observations. In Figure 29, which is a graytone version of Figure 28, we show the locations of the most luminous candidate yellow and blue stars around Knot S, based on the  $C < 1.52$  criterion. Table 5 lists these stars and gives their positions and photometric parameters.

Finally, Figure 30 shows a close up view of the second-brightest candidate yellow star. As in several other cases, the dominant yellow-red object appears to be embedded in a faint cluster. This is consistent with the object’s intermediate position in the two-color diagram between the CB07 cluster tracks and the Padova stellar models. Note also the preponderance of very blue or very yellow-red objects at slightly fainter magnitudes in the ACS/HRC image (Figure 28). Most of these objects are likely to be individual stars that have fallen out of our sample, generally due to the lack of a reliable WFPC2 measurement in the  $U$  band (Filter F336W).

#### A.4. Distinguishing Stars and Clusters Galaxy-Wide

We now use what we have learned from Training Sets 1 through 3 to extend our study of objects to the entire galaxies. Figures 31a–d plot all objects in the Antennae with  $M_V < -9$  that fall in cluster space, yellow-star space, foreground-star space, and blue-star/cluster space, respectively.

Figure 31a shows that while the vast majority of objects in *cluster space* are resolved (89% with  $C > 1.52$ ), there are also objects present in this part of the two-color diagram that are so compact as to be undifferentiable from stars based on their size alone, as discussed in §A.3 above.

Next, Figure 31b shows the dramatic difference in the fraction of unresolved objects in *yellow-star space* (79%), demonstrating that—while apparent size alone is not a perfect discriminator between stars and clusters—it does provide a good first-order separation, especially for bright objects with  $M_V < -9$ . However, one should keep in mind that there probably also are a few heavily reddened clusters in this region of the diagram, although they appear to be rare. Note that there are only four candidate yellow stars brighter than  $M_V = -9.5$ , hence this absolute magnitude appears to be an effective upper limit to the luminosity of yellow supergiants. This upper limit is known as the Humphreys–Davidson (1979) limit.

The fraction of unresolved objects in *foreground-star space* is an even higher 92%, as seen in Figure 31c. Note that the objects with apparent “absolute magnitudes” brighter than  $M_V = -10$  are almost certainly all foreground stars in our own Galaxy, whence their “absolute magnitudes”—computed for the adopted distance to the Antennae—are meaningless. The objects fainter than  $M_V = -10$  are likely to be a mix of foreground stars, yellow stars in the Antennae, and a few heavily reddened clusters as, e.g., the two objects with  $C > 1.52$ .

The fraction of objects in *blue-star/cluster space* with  $C > 1.52$  is essentially the same (87%) as in cluster space (89%), demonstrating that at these bright magnitudes few—if any—of the objects are individual stars. However, when we change our lower limit for  $M_V$  from  $-9$  to  $-8$  mag and then on to  $-7$  mag (not shown), we find that the fraction of objects with  $C < 1.52$  increases from 13% to 29% and on to 32%, respectively. While a few percent of these increases may be due to observational uncertainties (e.g., the fraction of objects in cluster space with  $C < 1.52$  also increases from 11% to 20%), it is clear that we are beginning to see a larger fraction of individual blue stars at fainter absolute magnitudes in this part of the diagram.

## REFERENCES

- Amram, P., Marcelin, M., Boulesteix, J., & le Coarer, E. 1992, *A&A*, 266, 106
- Anders, P., Bissantz, N., Boysen, L., de Grijs, R., & Fritze-v. Alvensleben, U. 2007, *MNRAS*, 377, 91
- Anders, P., Bissantz, N., Fritze-v. Alvensleben, U., & de Grijs, R. 2004, *MNRAS*, 347, 196
- Anders, P., Gieles, M., & de Grijs, R. 2006, *A&A*, 451, 375
- Barnes, J. 2004, *MNRAS*, 350, 798
- Bastian, N. 2008, *MNRAS*, 390, 759
- Bastian, N. & Goodwin, S. P. 2006, *MNRAS*, 369, 9
- Bastian, N., Emsellem, E., Kissler-Patig, M., & Maraston, C. 2006, *A&A*, 445, 471
- Bastian, N., Trancho, G., Konstantopoulos, I. S., & Miller, B. W. 2009, *ApJ*, 701, 607
- Bik, A., Lamers, H. J. G. L. M., Bastian, N., Panagia, N., & Romaniello, M. 2003, *A&A*, 397, 473
- Boily, C. M. & Kroupa, P. 2003, *MNRAS*, 338, 673
- Boutloukos, S. G., & Lamers, H. J. G. L. M. 2003, *MNRAS*, 338, 717
- Brandl, B. R., Clark, D. M., Eikenberry, S. S., Wilson, J. C., Henderson, C. P., Barry, D. J., Houck, J. R., Carson, J. C., & Hayward, T. L. 2005, *ApJ*, 635, 280
- Brandl, B. R., Sijnders, M., den Brok, M., Whelan, D. G., Groves, B., van der Werf, P., Charmandaris, V., Smith, J. D., Armus, L., Kennicutt, R. C., & Houck, J. R. 2009, *ApJ*, 699, 1928
- Bruzual A. G., & Charlot, S. 2003, *MNRAS*, 344, 1000
- Cervino, M., Valls-Gabaud, D., Luridiana, V., & Mas-Hesse, J. M. 2002, *A&A*, 381, 51
- Chandar, R., Fall, S. M., & Whitmore, B. C. 2010a, *ApJ*, in press
- Chandar, R., Fall, S. M., & Whitmore, B. C. 2010b, in preparation
- Chandar, R., Whitmore, B. C., Kim, H., Kaleida, C., Mutchler, M., Calzetti, D., Saha, A. and the WFC3 Science Oversight Committee 2010, in preparation
- Charlot, S. & Bruzual, G. 2007, private communication (CB07)
- Christopher, M. H. 2008, Ph.D. thesis, California Institute of Technology
- Clark, D. M., Eikenberry, S. S., Brandl, B. R., Wilson, J. C., Carson, J. C., Henderson, C. P., Hayward, T. L., Barry, D. J., Ptak, A. F., & Colbert, E. J. M. 2007, *ApJ*, 658, 319

- de Grijs, R., Parmentier, G., & Lamers, H. J. G. L. M. 2005, *MNRAS*, 364, 1054
- de Grijs, R. & Parmentier, G. 2007, *Chinese Journal Astronomy & Astrophysics*, 7, 155
- Dophin, A. E. 2000, *PASP*, 112, 1397
- Drout, M. R., Massey, P., Meynel, G., Tokarz, S., & Caldwell, N. 2009, *ApJ*, 703, 441
- Fabbiano, G., Krauss, M., Zezas, A., Rots, A., & Neff, S. 2003, *ApJ*, 598, 272,
- Fabbiano, G., Baldi, A., King, A. R., Ponman, T. J., Raymond, J., Read, A., Rots, A.,  
Schweizer, F., & Zezas, A. 2004, *ApJ*, 605, L21
- Fall, S. M. 2006, *ApJ*, 652, 1129
- Fall, S. M., Chandar, R., & Whitmore, B. C. 2005, *ApJ*, 631, L133 (FCW05)
- Fall, S. M., Chandar, R., & Whitmore, B. C. 2009, *ApJ*, 704, 453 (FCW09)
- Fall, S. M., Krumholz, M. R., & Matzner, C. D. 2010, *ApJ*, 710, 142
- Fall, S. M., & Zhang, Q., 2001, *ApJ*, 561, 751
- Fritze-von Alvensleben, U. 2004, in “Starbursts from 30 Doradus to Lyman Break Galaxies,”  
eds. R. de Grijs, R. M. Gonzalez Delgado, *Astrophysics & Space Science Library Series*,  
(Dordrecht: Kluwer)
- Gieles, M., Larsen, S., Bastian, N., & Stein, I. 2006, *A&A*, 450, 129
- Gilbert, A., & Graham, J. R. 2007, *ApJ*, 668, 168
- Hibbard, J. E., et al. 2005, *ApJ*, 619, L87
- Hibbard, J. E., van der Hulst, J. M., Barnes, J. E., & Rich, R. M. 2001, *AJ*, 122, 2969
- Hills, J. G. 1980, *ApJ*, 225, 986
- Holtzman, J. A., Burrows, C. J., Casertano, S., Hester, J. J., Trauger, J. T., Watson, A. M.,  
& Worthey, G. 1995, *PASP*, 107, 1065
- Humphreys, R. M., & Davidson, K. 1979, *ApJ*, 232, 409
- Hunter, D. A., Elmegreen, B. G., Dupuy, T. J., & Mortonson, M. 2003, *AJ*, 126, 1836
- Israel, F. P. 1978, *A&A*, 70, 769
- Karl, S. J., Naab, T., Johansson, P. H., Kotarba, H., Boily, C., Renaud, F. & Theis, C. 2010,  
arXiv:1003.0685v1
- Kassin, S. A., Frogel, J. A., Pogge, R. W., Tiede, G. P., & Sellgren, K. 2003, *AJ*, 126, 1276
- Koekemoer, A. M., Fruchter, A. S., Hook, R. N., & Hack, W. in *The 2002 HTT Calibration  
Workshop*, eds., A. Santiago, A. Koekemoer, & B. Whitmore (Cambridge: Cambridge  
University Press), p. 337

- Lada, C. J., & Lada, E. A. 2003, *ARA&A*, 41, 57
- Lada, C. J., Margulis, M., & Dearborn, D. 1984, *ApJ*, 285, 141
- Lamers, H. J. G. L. M., Gieles, M., Bastian, N., Baumgardt, H., Kharchenko, N. V., & Portegies Zwart, S. 2005, *A&A*, 441, 117
- Larsen, S. S. 1999, *A&A*, 139, 393
- Larsen, S. S. 2002, *AJ*, 124, 1393
- Larsen, S. S. 2005, “Star Formation in Clusters,” in *Planets to Cosmology: Essential Science in Hubble’s Final Years*, ed., M. Livio (Cambridge: Cambridge University Press) (astro-ph/0408201)
- Larsen, S. S. 2006, “Observational Constraints on Cluster Evolution,” in *Mass Loss from Stars and the Evolution of Stellar Clusters*, ed., A. de Koter, R. Waters & L. Smith, ASP Conference Series, (San Francisco: ASP) (astro-ph/0609062)
- Larsen, S. S. 2009, *A&A*, 494, 539
- Maíz Apellániz, J. 2009, *Ap&SS*, 324, 95
- Mengel, S., Lehnert, M. D., Thatte, N., & Genzel, R. 2005, *A&A*, 443, 41
- Mengel, S., Lehnert, M. D., Thatte, N., Vacca, W. D., Whitmore, B., & Chandar, R. 2008, *A&A*, 489, 1091
- Metz, J. M., Cooper, R. L., Guerrero, M. A., Chu, Y., Chen, C. R., & Gruendl, R. A. 2004, *ApJ*, 605, 725
- Mirabel, L. F., Vigroux, L., Charmandaris, V., Sauvage, M., Gallais, P., Tran, D., Cesarsky, C., Madden, S. C., & Duc, P. A. 1998, *A&A*, 333, L1
- Mora, M. D., Larsen, S. S., Kissler-Patig, M., Brodie, J. P., & Richtler, T. 2009, *A&A*, 501, 949
- Mihos, J. C., Bothun, G. D., & Richstone, D. O. 1993, *ApJ*, 418, 82
- Neff, S. G., & Ulvestad, J. S. 2000, *AJ*, 120, 670
- Renaud, F., Boily, C. M., Fleck, J., Naab, T., & Theis, C. 2009, *MNRAS*, 391, L98
- Rossa, J., Laine, S., van der Marel, R. P., Mihos, J. C., Hibbard, J. E., Boker, T., & Zabludoff, A. L. 2007, *AJ*, 134, 2124
- Rubin, V. C., Ford, W. K. Jr., & D’Odorico, S. 1970, *ApJ*, 160, 801
- Saviane, I., Momany, Y., Da Costa, G. S., Rich, R. M., & Hibbard, J. E. 2008, *ApJ*, 678, 179

- Schulz, A., Henkel, C., Muders, D., Mao, R. Q., Rollig, M., & Mauersberger, R. 2007, *A&A*, 466, 467
- Schweizer, F., et al. 2008, *AJ*, 136, 1482
- Sirianni, M., et al. 2005, *PASP*, 117, 1049
- Toomre, A. 1977, in *The Evolution of Galaxies and Stellar Populations*, eds. B. M. Tinsley & R. B. Larson (Yale University Press, New Haven), p. 401
- Ubeda, L., Maiz-Apellaniz, J., & Mackenty, J. 2007, *AJ*, 133, 917.
- Walborn, N. R., Barba, R. H., Brandner, W., Rubio, M., Grebel, E. K., & Probst, R. G. 1999, *AJ*, 117, 225
- Wang, Z., Fazio, G. G., Ashby, M. L. N., Huang, J.-S., Pahre, M. A., Smith, H. A., Willner, S. P., Forrest, W. J., Pipher, J. L., & Surace, J. A. 2004, *ApJS*, 154, 193
- Whitmore, B. C. 2003, *The Formation of Star Clusters*, in “A Decade of HST Science,” eds., Mario Livio, Keith Noll, & Massimo Stiavelli (Cambridge: Cambridge University Press), 153
- Whitmore, B. C., Casertano, S., White, R. L., & 24 other authors, 2010, in preparation
- Whitmore, B. C., Chandar, R. C., & Fall, S. M. 2007, *AJ*, 133, 1067 (WFC07)
- Whitmore, B. C., Gilmore, D., Leitherer, C., Fall, S. M., Chandar, R., Blair, W. P., Schweizer, F., Zhang, Q., & Miller, B. W. 2005, *AJ*, 130, 2104
- Whitmore, B. C., & Schweizer, F. 1995, *AJ*, 109, 960
- Whitmore, B. C., Zhang, Q., Leitherer, C., Fall, S. M., Schweizer, F., & Miller, B. W. 1999, *AJ*, 118, 1551
- Whitmore, B. C., & Zhang, Q. 2002, *AJ*, 124, 1418
- Wilson, C. D., Scoville, N., Madden, S., & Charmandaris, V. 2000, *ApJ*, 542, 120
- Wilson, C. D., Scoville, N., Madden, S., & Charmandaris, V. 2003, *ApJ*, 599, 1049
- Zezas, A., Fabbiano, G., Baldi, A., Schweizer, F., King, A. R., Ponman, T. J., & Rots, A. H. 2006, *ApJS*, 166, 211
- Zezas, A., Fabbiano, G., Baldi, A., Schweizer, F., King, A. R., Rots, A. H., & Ponman, T. J. 2007, *ApJ*, 661, 135
- Zhang, Q., & Fall, S. M. 1999, *ApJ*, 527, L81
- Zhang, Q., Fall, S. M., & Whitmore, B. C. 2001, *ApJ*, 561, 727

Zhu, M., Seaquist, E. R., & Kuno, N. 2003, *ApJ*, 588, 243



Table 1. Training Set 1 – Isolated Stars

#	ID	RA	DEC	$V$	$C$	$U-B$	$V-I$
(1)	(2)	(3)	(4)	(5)	(6)	(7)	(8)
1	613	12:01:55.7415	-18:54:34.579	22.24	1.39	—	0.68
2	1136	12:01:54.5631	-18:54:20.884	23.32	1.46	—	2.45
3	2630	12:01:54.1272	-18:54:00.581	19.50	1.51	—	1.46
4	4839	12:01:48.6882	-18:53:43.771	22.76	1.52	—	2.54
5	7023	12:01:46.3254	-18:53:33.566	21.80	1.43	—	0.96
6	7491	12:01:46.9367	-18:53:31.676	20.58	1.38	—	0.91
7	8480	12:01:48.6734	-18:53:27.519	22.42	1.48	0.98	1.74
8	8682	12:01:44.3237	-18:53:26.731	20.08	1.52	—	0.63
9	9286	12:01:49.1499	-18:53:24.155	22.44	1.41	1.29	2.00
10	10720	12:01:48.8214	-18:53:19.320	22.72	1.47	0.32	0.82
11	12987	12:01:46.9616	-18:53:12.194	23.76	1.37	—	0.94
12	14982	12:01:49.0956	-18:53:06.515	22.21	1.39	1.65	2.91
13	16825	12:01:53.0615	-18:53:00.087	23.20	1.47	1.77	1.25
14	17004	12:01:50.0916	-18:52:59.413	23.41	1.44	—	0.82
15	17964	12:01:50.4818	-18:52:56.122	21.50	1.49	1.51	1.71
16	18167	12:01:58.7591	-18:52:55.352	21.16	1.39	2.53	1.21
17	18417	12:01:44.7510	-18:52:54.474	21.05	1.50	—	0.55
18	20475	12:01:56.2577	-18:52:46.213	20.09	1.44	2.43	2.00
19	21767	12:01:53.3848	-18:52:41.607	22.33	1.51	0.92	1.03
20	27696	12:01:53.7585	-18:52:27.105	20.34	1.39	0.12	0.57
21	29805	12:02:02.2895	-18:52:23.653	18.55	1.49	—	0.45
22	34825	12:02:02.2330	-18:52:15.868	21.63	1.51	—	0.57
23	35045	12:02:01.3544	-18:52:15.510	23.65	1.42	—	1.81
24	50277	12:01:54.9046	-18:51:48.495	19.36	1.43	1.22	1.08
25	60076	12:01:49.8474	-18:51:21.501	18.84	1.39	-0.07	0.64
26	60094	12:01:52.4592	-18:51:21.133	22.60	1.49	—	2.05

Table 2. Training Set 1 – Old Globular Clusters

#	ID	RA	DEC	$M_V$	$C$	$U-B$	$V-I$	Old ID
(1)	(2)	(3)	(4)	(5)	(6)	(7)	(8)	(9) <sup>a</sup>
Previous Good Candidates								
1	4150	12:01:51.4714	–18:53:47.899	–9.27	1.41	1.23	0.91	8 <sup>b</sup>
2	4169	12:01:51.5055	–18:53:47.739	–9.28	1.64	0.29	0.86	6
3	5129	12:01:51.8439	–18:53:42.270	–9.42	1.64	0.01	0.80	3
4	5641	12:01:53.1949	–18:53:39.703	–8.36	1.63	0.12	1.10	10
5	9160	12:01:51.0299	–18:53:24.726	–8.63	1.69	0.09	0.94	9
6	9443	12:01:50.8450	–18:53:23.616	–9.12	1.64	0.24	1.07	7
7	10881	12:01:49.6483	–18:53:18.824	–8.12	1.75	0.21	0.89	11
8	19740	12:01:57.2806	–18:52:49.207	–9.33	1.68	0.24	0.86	5
9	20383	12:01:54.0195	–18:52:46.552	–10.89	1.48	0.31	0.79	1 <sup>b</sup>
10	42197	12:01:51.8296	–18:52:04.096	–9.45	1.77	–0.14	0.77	2
11	60284	12:01:53.0748	–18:51:15.764	–9.28	1.65	0.10	0.80	4
Additional Good Candidates								
12	935	12:01:53.4373	–18:54:24.962	–8.44	1.59	—	0.86	
13	1635	12:01:55.8945	–18:54:12.315	–8.53	1.58	—	0.75	
14	3016	12:01:53.3451	–18:53:57.197	–8.39	1.63	—	0.81	
15	4299	12:01:54.9452	–18:53:46.943	–8.32	1.60	—	0.96	
16	4927	12:01:52.9523	–18:53:43.351	–8.83	1.66	0.84	1.11	
17	5234	12:01:54.6394	–18:53:41.680	–8.84	1.67	—	0.98	
18	7651	12:01:56.8215	–18:53:30.965	–8.53	1.73		0.78	
19	12230	12:01:51.1248	–18:53:14.541	–8.06	1.62	1.29	1.06	
20	16051	12:01:56.4667	–18:53:03.006	–8.19	1.65	0.00	1.20	
21	16328	12:01:55.4370	–18:53:01.921	–8.26	1.75	1.11	1.01	
22	20154	12:01:52.6369	–18:52:47.577	–8.56	1.60	0.00	0.81	
23	21253	12:01:52.3052	–18:52:43.364	–8.22	1.66	0.05	0.83	
24	39147	12:01:51.7752	–18:52:09.392	–8.65	1.72	0.45	0.81	
25	56458	12:01:56.0763	–18:51:37.157	–9.11	1.59	0.52	1.00	
26	59900	12:01:52.8571	–18:51:24.263	–8.78	1.58	0.19	0.83	
Additional Fair Candidates								
27	2771	12:01:50.8738	–18:53:59.279	–7.94	1.61	0.34	0.75	
28	3393	12:01:49.8663	–18:53:53.634	–7.26	1.78	–0.03	0.84	
29	7006	12:01:52.9097	–18:53:33.617	–8.47	1.73	–0.15	0.75	

Table 2—Continued

#	ID	RA	DEC	$M_V$	$C$	$U-B$	$V-I$	Old ID
(1)	(2)	(3)	(4)	(5)	(6)	(7)	(8)	(9) <sup>a</sup>
30	19624	12:01:54.9801	-18:52:49.689	-8.93	1.62	0.00	0.87	
31	22843	12:01:57.7456	-18:52:38.276	-7.16	1.75	0.06	0.88	
32	25751	12:01:54.2522	-18:52:30.796	-9.42	1.61	0.67	0.98	
33	27148	12:01:58.1976	-18:52:28.094	-7.34	1.80	0.29	0.95	
34	39147	12:01:51.7752	-18:52:09.392	-8.65	1.72	0.45	0.81	
35	39889	12:01:53.7189	-18:52:08.176	-8.41	1.60	0.15	0.79	
36	43099	12:01:53.6510	-18:52:02.501	-8.89	1.67	0.18	0.75	
37	44151	12:01:53.4195	-18:52:00.339	-9.21	1.63	0.01	0.90	
38	44714	12:01:54.0253	-18:51:59.188	-9.26	1.68	0.11	0.79	
39	45810	12:01:51.8726	-18:51:57.080	-8.29	1.76	-0.14	0.82	
40	46967	12:01:54.2646	-18:51:54.748	-8.33	1.79	-0.07	0.78	
41	47348	12:01:55.5780	-18:51:54.035	-8.26	1.76	0.34	0.76	
42	49136	12:01:51.8314	-18:51:50.645	-8.63	1.66	0.74	0.75	

<sup>a</sup>See Table 3, Whitmore et al. (1999).

<sup>b</sup>Likely star, based on small value of  $C$ . See Appendix A.1 for discussion.

Table 3. Training Set 2 (Outer 9) – Intermediate-Age Clusters

#	ID	RA	DEC	$M_V$	$C$	$U-B$	$V-I$	$E(B-V)$	Log $\tau$	Mass
(1)	(2)	(3)	(4)	(5)	(6)	(7)	(8)	(9)	(10)	(11)
1	58909	12:01:50.9787	-18:51:30.197	-10.22	1.81	-0.01	0.41	0.00	8.41	3.22 E5
2	58549	12:01:51.0594	-18:51:31.526	-10.10	1.81	-0.08	0.38	0.00	8.36	2.74 E5
3	59721	12:01:50.6764	-18:51:26.030	-9.96	1.84	-0.03	0.39	0.00	8.41	2.56 E5
4	59474	12:01:49.7051	-18:51:27.682	-9.30	1.71	0.30	0.46	0.00	8.56	1.78 E5
5	60197	12:01:49.3203	-18:51:18.795	-9.05	1.72	—	0.57	0.04	8.26	1.05 E5
6	59798	12:01:49.9133	-18:51:25.384	-8.89	1.89	0.08	0.52	0.00	8.51	1.10 E5
7	59904	12:01:50.0653	-18:51:24.245	-8.72	1.68	0.43	0.43	0.00	8.56	1.02 E5
8	59797	12:01:51.3711	-18:51:25.379	-8.18	1.74	-0.11	0.35	0.00	8.31	4.50 E4
9	58828	12:01:51.2279	-18:51:30.517	-8.11	1.67	0.00	0.65	0.10	8.26	5.29 E4
					Likely Star					
—	60076	12:01:49.8474	-18:51:21.501	-12.87 <sup>a</sup>	1.39	-0.07	0.64	0.02	—	—

<sup>a</sup>This magnitude is meaningless if the object is a foreground star, but is included in case the object turns out to be a cluster. See text for discussion.

Table 4. Training Set 3 (Knot S) – Mixed Stars and Clusters

#	ID	RA	DEC	$M_V$	$C$	$U-B$	$V-I$	$E(B-V)$	Log $\tau$	Mass
(1)	(2)	(3)	(4)	(5)	(6)	(7)	(8)	(9)	(10)	(11)
					Candidate Clusters					
1	32771	12:01:50.5334	-18:52:19.242	-11.20	1.69	-0.93	0.35	0.00	7.51	2.73 E5
3	33536	12:01:50.7583	-18:52:18.036	-9.51	1.77	0.18	0.52	0.00	8.46	1.83 E5
6	34134	12:01:50.5929	-18:52:17.080	-8.75	1.68	-0.44	0.62	0.20	8.06	1.05 E5
9	35118	12:01:50.4052	-18:52:15.428	-11.19	1.57	-1.06	0.36	0.00	7.51	2.74 E5
10	35128	12:01:50.7005	-18:52:15.399	-9.85	1.83	-0.94	0.64	0.64	6.38	1.84 E5
11	35687	12:01:50.5041	-18:52:14.532	-10.48	1.66	-1.03	0.44	0.26	6.76	5.09 E4
12	35780	12:01:50.4830	-18:52:14.404	-10.86	1.79	-1.24	0.22	0.32	6.50	9.55 E4
14	35897	12:01:50.4453	-18:52:14.223	-11.63	1.70	-0.91	0.49	0.00	7.63	4.55 E5
16	36094	12:01:50.4607	-18:52:13.932	-14.63	1.71	-1.68	-0.05	0.12	6.78	1.63 E6
19	37300	12:01:50.5679	-18:52:12.223	-12.93	1.66	-1.00	0.48	0.00	7.51	1.34 E6
21	37521	12:01:50.2009	-18:52:11.865	-10.76	1.84	-1.19	-0.03	0.00	6.78	3.35 E4
					Candidate Stars					
2	32864	12:01:50.4862	-18:52:19.094	-10.78	1.50	-1.31	0.19	0.04	—	—
4	33853	12:01:50.7798	-18:52:17.531	-9.35	1.44	1.23	0.63	0.00	—	—
5	34109	12:01:50.3400	-18:52:17.149	-7.31	1.45	-1.64	0.50	0.00	—	—
7	34394	12:01:50.1945	-18:52:16.618	-8.25	1.40	-0.30	0.49	0.00	—	—
8	34439	12:01:50.5483	-18:52:16.524	-8.92	1.41	-0.80	0.25	0.32	—	—
13	35829	12:01:50.1773	-18:52:14.329	-8.10	1.40	-0.68	0.53	0.00	—	—
15	35914	12:01:50.4009	-18:52:14.197	-8.52	1.43	-0.64	0.16	0.22	—	—
17	36966	12:01:50.4276	-18:52:12.707	-9.58	1.45	-0.68	0.14	0.00	—	—
18	37058	12:01:50.2591	-18:52:12.555	-10.36	1.79 <sup>a</sup>	-1.12	0.02	0.02	6.78 <sup>a</sup>	2.40 E4 <sup>a</sup>
20	37398	12:01:50.3277	-18:52:12.066	-7.33	1.25	-1.65	1.43	0.28	—	—
22	38311	12:01:50.4612	-18:52:10.702	-9.36	1.46	0.33	0.51	0.00	—	—
23	38533	12:01:50.5411	-18:52:10.395	-8.86	1.54 <sup>a</sup>	-0.68	0.62	0.16	7.91 <sup>a</sup>	8.07 E4 <sup>a</sup>

<sup>a</sup>These objects are likely to be clusters, based on  $C$ , hence reddening and age values are included.

Table 5. Training Set 3 (Knot S) – Brightest Candidate Yellow and Blue Stars

#	ID	RA	DEC	$M_V$	$C$	$U-B$	$V-I$
(1)	(2)	(3)	(4)	(5)	(6)	(7)	(8)
Yellow Stars							
1	38311	12:01:50.4612	–18:52:10.702	–9.36	1.46	0.33	0.51
2	33853	12:01:50.7798	–18:52:17.531	–9.35	1.44	1.23	0.63
3	33032	12:01:50.3345	–18:52:18.862	–9.32	1.40	0.45	0.63
4	34751	12:01:50.2708	–18:52:16.030	–8.85	1.35	0.48	0.35
5	34526	12:01:50.4021	–18:52:16.375	–8.54	1.37	0.50	0.12
6	34034	12:01:50.2675	–18:52:17.256	–8.16	1.44	0.66	0.50
Blue Stars							
1	36176	12:01:50.5054	–18:52:13.803	–9.62	1.49	–0.91	–0.20
2	36353	12:01:50.2560	–18:52:13.578	–8.72	1.48	–1.22	–0.19
3	36579	12:01:50.3469	–18:52:13.242	–8.47	1.35	–0.95	0.04
4	36505	12:01:50.2515	–18:52:13.352	–8.20	1.47	–1.51	–0.37
5	32772	12:01:50.4016	–18:52:19.240	–8.18	1.50	–1.50	–0.32
6	34618	12:01:50.6484	–18:52:16.228	–8.06	1.48	–1.40	0.00
7	37952	12:01:50.2040	–18:52:11.238	–8.01	1.50	–1.63	–0.10

Table 6. 50 Most Luminous Clusters

#	ID	RA	DEC	$M_V$	$C^a$	$U-B$	$V-I$	$E(B-V)$	$\text{Log } \tau$	Mass <sup>b</sup>	comments
(1)	(2)	(3)	(4)	(5)	(6)	(7)	(8)	(9)	(10)	(11)	(12)
1	36094	12:01:50.4607	-18:52:13.932	-14.63	1.71	-1.68	-0.05	0.12	6.78	1.63 E6 (10)	Knot S
2	50776	12:01:51.3963	-18:51:47.562	-14.45	1.61	-1.47	-0.23	0.04	6.78	1.09 E6 (24)	Knot G
3	38220	12:01:53.0075	-18:52:10.829	-14.20	1.52	-1.75	-0.14	0.08	6.76	9.22 E5 (28)	Knot K, 13th IR
4	38639	12:01:53.0355	-18:52:10.223	-13.27	1.67	-1.16	0.00	0.00	6.78	3.30 E5	Knot K, 35th IR
5	21058	12:01:55.8098	-18:52:44.038	-13.08	1.57	-1.11	0.07	0.22	6.64	5.01 E5	Knot D
6	36737	12:01:54.7459	-18:52:12.988	-12.93	1.67	-1.21	-0.09	0.00	6.78	2.45 E5	Knot F
7	37300	12:01:50.5679	-18:52:12.223	-12.93	1.66	-1.00	0.48	0.00	7.51	1.34 E6 (18)	Knot S
8	37254	12:01:56.0399	-18:52:12.264	-12.87	1.61	-0.85	0.58	0.02	7.53	1.35 E6 (17)	Region 6
9	25671	12:01:51.1582	-18:52:30.977	-12.83	1.65	-0.86	0.38	0.00	7.72	1.56 E6 (13)	Region 14
10	40713	12:01:50.5088	-18:52:06.752	-12.72	1.67	-1.05	0.10	0.06	6.78	2.39 E5	Knot R
11	32604	12:01:55.4307	-18:52:19.476	-12.68	1.65	-0.77	0.57	0.06	7.70	1.58 E6 (12)	Region 7, 1st IR
12	38959	12:01:54.6090	-18:52:09.734	-12.60	1.63	-1.34	-0.17	0.00	6.58	1.60 E5	Knot F
13	36731	12:01:55.9896	-18:52:12.985	-12.54	1.66	-0.81	0.59	0.04	7.63	1.15 E6 (21)	Region 6, 2nd IR
14	35177	12:01:54.8864	-18:52:15.318	-12.53	1.68	-0.95	0.09	0.12	6.78	2.37 E5	Knot F
15	15492	12:01:54.6691	-18:53:04.875	-12.39	1.62	-0.32	0.77	1.00	6.40	4.22 E6 (2)	Knot B
16	45889	12:01:54.3092	-18:51:56.879	-12.26	1.60	-0.95	0.49	0.00	7.51	7.24 E5 (38)	Region 9, 23rd IR
17	25220	12:01:52.0390	-18:52:31.975	-12.25	1.60	-1.07	0.13	0.10	6.78	1.73 E5	Knot M
18	27222	12:01:51.8954	-18:52:27.963	-12.24	1.70	-0.51	0.73	0.12	8.26	2.52 E6 (5)	Knot M
19	26993	12:01:52.0013	-18:52:28.376	-12.22	1.66	-0.90	0.29	0.34	6.70	3.30 E5	Knot M
20	15398	12:01:54.5335	-18:53:05.193	-12.20	1.72	-0.74	0.63	0.12	7.68	1.16 E6 (20)	Knot B, 8th IR
21	32364	12:01:55.7614	-18:52:19.797	-12.18	1.55	-0.83	0.36	0.00	7.72	8.54 E5 (30)	Region 4, 38th IR
22	28556	12:01:53.1260	-18:52:25.650	-12.16	1.68	-0.92	0.53	0.00	7.51	6.60 E5 (42)	Region 8, 10th IR
23	30652	12:01:50.5117	-18:52:22.453	-12.11	1.52	-1.09	0.27	0.14	6.74	1.64 E5	Knot T
24	29516	12:01:55.6342	-18:52:24.141	-12.06	1.58	-0.79	0.44	0.00	7.81	8.53 E5 (31)	Knot E, 25th IR
25	21464	12:01:55.1483	-18:52:42.579	-12.06	1.78	-0.37	0.45	0.00	8.31	1.61 E6 (11)	Region 2, 32nd IR
26	31099	12:01:52.2670	-18:52:21.710	-12.04	1.72	-1.20	0.11	0.04	6.78	1.21 E5	Knot L
27	14003	12:01:53.1657	-18:53:09.214	-12.01	1.75	-0.50	1.04	0.42	7.81	2.81 E6 (4)	Knot A
28	31265	12:01:50.4090	-18:52:21.477	-11.99	1.86	-0.92	0.46	0.00	7.53	5.68 E5 (50)	Knot T
29	38372	12:01:54.5174	-18:52:10.592	-11.97	1.62	-1.00	0.29	0.10	6.80	1.47 E5	Knot F, 42nd IR
30	55784	12:01:52.7066	-18:51:38.512	-11.92	1.59	-1.39	0.13	0.24	6.46	3.63 E5	Knot P
31	48841	12:01:51.3683	-18:51:51.199	-11.91	1.60	-0.47	1.03	0.44	7.91	3.05 E6 (3)	Knot G
32	19275	12:01:55.4319	-18:52:51.151	-11.90	1.92	-1.46	0.39	0.32	6.02	4.68 E5	Knot C
33	19459	12:01:55.4798	-18:52:50.412	-11.90	1.67	-1.47	-0.13	0.10	6.56	1.25 E5	Knot C

Table 6—Continued

#	ID	RA	DEC	$M_V$	$C^a$	$U-B$	$V-I$	$E(B-V)$	Log $\tau$	Mass <sup>b</sup>	comments
(1)	(2)	(3)	(4)	(5)	(6)	(7)	(8)	(9)	(10)	(11)	(12)
34	29784	12:01:55.9339	-18:52:23.711	-11.86	1.66	-0.69	0.54	0.04	7.81	7.88 E5 (35)	Region 4, 37th IR
35	42384	12:01:53.1008	-18:52:03.750	-11.85	1.61	-0.52	0.65	0.96	6.40	2.30 E6 (6)	Knot J
36	27080	12:01:52.0153	-18:52:28.242	-11.85	1.75	-1.40	0.03	0.20	6.54	1.60 E5	Knot M
37	15502	12:01:54.6349	-18:53:04.827	-11.82	1.82	-1.27	0.11	0.38	6.48	3.12 E5	Knot B
38	19416	12:01:55.4844	-18:52:50.547	-11.81	1.77	-1.47	-0.08	0.00	6.72	8.76 E4	Knot C
39	28042	12:01:51.3940	-18:52:26.497	-11.77	1.70	-0.66	0.24	0.02	8.06	9.96 E5 (26)	Region 14
40	25824	12:01:51.1646	-18:52:30.680	-11.77	1.61	-0.91	0.32	0.00	7.72	5.90 E5 (47)	Region 14
41	40612	12:01:50.4939	-18:52:06.927	-11.76	1.65	-1.06	0.17	0.10	6.78	1.08 E5	Knot R
42	52713	12:01:51.2689	-18:51:44.205	-11.73	1.77	-1.17	0.54	0.00	7.12	2.18 E5	Knot G
43	32282	12:01:50.3558	-18:52:19.946	-11.72	1.75	-1.21	-0.19	0.04	6.66	9.07 E4	Knot T
44	15466	12:01:54.6439	-18:53:04.958	-11.70	1.84	-1.33	0.22	0.38	6.08	4.23 E5	Knot B, 4th IR
45	35897	12:01:50.4453	-18:52:14.223	-11.63	1.70	-0.91	0.49	0.00	7.63	4.55 E5	Knot S
46	29410	12:01:55.4840	-18:52:24.273	-11.62	1.64	-0.58	0.64	0.18	7.91	1.10 E6 (23)	Knot E, 27th IR
47	14034	12:01:53.4714	-18:53:09.111	-11.60	1.75	-1.16	0.16	0.20	6.72	1.28 E5	Knot A
48	14422	12:01:53.3319	-18:53:08.037	-11.60	1.79	-0.62	0.80	0.28	7.86	1.38 E6 (15)	Knot A
49	15145	12:01:54.6547	-18:53:06.010	-11.60	1.58	-0.54	0.43	0.58	6.66	3.94 E5	Knot B
50	14550	12:01:53.5296	-18:53:07.726	-11.60	1.63	-1.19	0.10	0.00	6.80	7.74 E4	Knot A

<sup>a</sup>Values of  $C > 1.51$  are required for inclusion in this table.

<sup>b</sup>Values in parentheses are the rank order from Table 7.

Table 7. 50 Most Massive Clusters

#	ID	RA	DEC	$M_V^a$	$C^b$	$U-B$	$V-I$	$E(B-V)$	$\log \tau$	Mass	comments
(1)	(2)	(3)	(4)	(5)	(6)	(7)	(8)	(9)	(10)	(11)	(12)
1	14612	12:01:55.0360	-18:53:07.529	-7.79	1.67	-1.70	3.16	2.44	6.00	6.80 E6	“WS80” <sup>c</sup> , near Knot B, 16th IR
2	15492	12:01:54.6691	-18:53:04.875	-12.39 (15)	1.62	-0.32	0.77	1.00	6.40	4.22 E6	Knot B
3	48841	12:01:51.3683	-18:51:51.199	-11.91 (31)	1.60	-0.47	1.03	0.44	7.91	3.05 E6	Knot G
4	14003	12:01:53.1657	-18:53:09.214	-12.01 (27)	1.75	-0.50	1.04	0.42	7.81	2.81 E6	Knot A
5	27222	12:01:51.8954	-18:52:27.963	-12.24 (18)	1.70	-0.51	0.73	0.12	8.26	2.52 E6	Knot M
6	42384	12:01:53.1008	-18:52:03.750	-11.85 (35)	1.61	-0.52	0.65	0.96	6.40	2.30 E6	Knot J
7	32187	12:01:55.2607	-18:52:20.093	-11.28	1.65	-0.13	0.93	0.30	8.31	1.88 E6	Region 7, 19th IR
8	31730	12:01:55.5385	-18:52:20.760	-11.31	1.74	-0.45	1.16	0.50	7.74	1.71 E6	Knot E
9	25751	12:01:54.2522	-18:52:30.796	-9.42	1.61	0.67	0.98	0.00	9.68	1.66 E6	Region 8, old globular cluster
10	36094	12:01:50.4607	-18:52:13.932	-14.63 (1)	1.71	-1.68	-0.05	0.12	6.78	1.63 E6	Knot S
11	21464	12:01:55.1483	-18:52:42.579	-12.06 (25)	1.78	-0.37	0.45	0.00	8.31	1.61 E6	Region 2, 32th IR
12	32604	12:01:55.4307	-18:52:19.476	-12.68 (11)	1.65	-0.77	0.57	0.06	7.70	1.58 E6	Region 7, 1st IR
13	25671	12:01:51.1582	-18:52:30.977	-12.83 (9)	1.65	-0.86	0.38	0.00	7.72	1.56 E6	Region 14
14	42257	12:01:53.1051	-18:52:03.964	-11.35	1.58	-0.28	0.70	1.08	6.50	1.39 E6	Knot J, 21st IR
15	14422	12:01:53.3319	-18:53:08.037	-11.60 (48)	1.79	-0.62	0.80	0.28	7.86	1.38 E6	Knot A
16	30673	12:01:56.2076	-18:52:22.386	-10.23	1.77	0.04	1.18	0.48	8.41	1.37 E6	Region 4, 47th IR
17	37254	12:01:56.0399	-18:52:12.264	-12.87 (8)	1.61	-0.85	0.58	0.02	7.53	1.35 E6	Region 6
18	37300	12:01:50.5679	-18:52:12.223	-12.93 (7)	1.66	-1.00	0.48	0.00	7.51	1.34 E6	Knot S
19	18848	12:01:54.8341	-18:52:52.841	-7.66	1.67	0.56	3.02	2.20	6.68	1.20 E6	near Knot C, 28th IR
20	15398	12:01:54.5335	-18:53:05.193	-12.20 (20)	1.72	-0.74	0.63	0.12	7.68	1.16 E6	Knot B, 8th IR
21	36731	12:01:55.9896	-18:52:12.985	-12.54 (13)	1.66	-0.81	0.59	0.04	7.63	1.15 E6	Region 6, 2nd IR
22	21028	12:01:55.3679	-18:52:44.177	-11.21	1.53	-0.20	0.47	0.10	8.46	1.14 E6	Region 2
23	29410	12:01:55.4840	-18:52:24.273	-11.62 (46)	1.64	-0.58	0.64	0.18	7.91	1.10 E6	Knot E, 27th IR
24	50776	12:01:51.3963	-18:51:47.562	-14.45 (2)	1.61	-1.47	-0.23	0.04	6.78	1.09 E6	Knot G
25	35561	12:01:55.0547	-18:52:14.710	-10.49	1.63	-0.25	0.95	0.46	8.06	1.08 E6	Knot F
26	28042	12:01:51.3940	-18:52:26.497	-11.77 (39)	1.70	-0.66	0.24	0.02	8.06	9.96 E5	Region 14
27	41030	12:01:53.0442	-18:52:06.195	-11.17	1.66	-0.53	0.67	0.22	8.01	9.38 E5	Knot J, 17th IR
28	38220	12:01:53.0075	-18:52:10.829	-14.20 (3)	1.52	-1.75	-0.14	0.08	6.76	9.22 E5	Knot K, 13th IR
29	9443	12:01:50.8450	-18:53:23.616	-9.15	1.64	0.24	1.07	0.00	9.51	8.87 E5	near Outer 1, old globular cluster
30	32364	12:01:55.7614	-18:52:19.797	-12.18 (21)	1.55	-0.83	0.36	0.00	7.72	8.54 E5	Region 4, 38th IR
31	29516	12:01:55.6342	-18:52:24.141	-12.06 (24)	1.58	-0.79	0.44	0.00	7.81	8.53 E5	Knot E, 25th IR
32	23657	12:01:51.3760	-18:52:35.888	-10.61	1.56	-0.56	0.81	0.36	8.01	8.47 E5	Region 14
33	38235	12:01:54.8023	-18:52:10.810	-11.06	1.55	-0.48	0.92	0.18	8.11	8.17 E5	Knot F, 34th IR
34	40436	12:01:55.3956	-18:52:07.226	-11.21	1.71	-0.43	0.73	0.10	8.16	8.00 E5	Region 7, 41st IR



Table 7—Continued

#	ID	RA	DEC	$M_V^a$	$C^b$	$U-B$	$V-I$	$E(B-V)$	$\text{Log } \tau$	Mass	comments
(1)	(2)	(3)	(4)	(5)	(6)	(7)	(8)	(9)	(10)	(11)	(12)
35	29784	12:01:55.9339	-18:52:23.711	-11.86 (34)	1.66	-0.69	0.54	0.04	7.81	7.88 E5	Region 4, 37th IR
36	31216	12:01:56.2315	-18:52:21.543	-11.20	1.77	-0.44	0.68	0.10	8.16	7.76 E5	Region 4, 46th IR
37	6993	12:01:52.5961	-18:53:33.643	-11.51	1.75	-0.54	0.40	0.02	8.06	7.59 E5	Outer 1
38	45889	12:01:54.3092	-18:51:56.879	-12.26 (16)	1.60	-0.95	0.49	0.00	7.51	7.24 E5	Region 9, 23rd IR
39	14825	12:01:57.8272	-18:53:06.960	-9.37	1.56	—	0.94	0.00	9.30	7.20 E5	Outer 5, old globular cluster
40	24693	12:01:54.8371	-18:52:33.145	-8.45	1.69	1.27	1.41	1.44	6.00	6.82 E5	Region 2
41	39348	12:01:56.0426	-18:52:09.029	-10.93	1.78	0.04	0.43	0.00	8.46	6.75 E5	Region 6
42	28556	12:01:53.1260	-18:52:25.650	-12.16 (22)	1.68	-0.92	0.53	0.00	7.51	6.60 E5	near Region 8, 10th IR
43	40591	12:01:53.0323	-18:52:06.964	-10.89	1.55	-0.23	0.61	0.96	6.48	6.60 E5	Knot J
44	26387	12:01:55.5827	-18:52:29.540	-9.84	1.62	-0.21	1.09	0.50	8.01	6.20 E5	Region 8
45	38583	12:01:52.7265	-18:52:10.300	-11.52	1.59	-0.73	0.44	0.02	7.91	6.11 E5	near Knot K, 50th IR
46	31419	12:01:56.0175	-18:52:21.251	-11.17	1.71	-0.62	0.69	0.04	8.11	6.01 E5	Region 4, 43rd IR
47	25824	12:01:51.1646	-18:52:30.680	-11.77 (40)	1.61	-0.91	0.32	0.00	7.72	5.90 E5	Region 14
48	27555	12:01:51.5593	-18:52:27.393	-9.11	1.67	-0.15	1.28	0.58	8.31	5.87 E5	Region 14
49	34777	12:01:55.2514	-18:52:15.972	-10.62	1.62	-0.28	0.63	0.10	8.31	5.80 E5	Region 7
50	31265	12:01:50.4090	-18:52:21.477	-11.99 (28)	1.86	-0.92	0.46	0.00	7.53	5.68 E5	Knot T

<sup>a</sup>Values in parentheses are the rank order from Table 6.

<sup>b</sup>Values of  $C > 1.51$  are required for inclusion in this table.

<sup>c</sup>See Whitmore & Zhang (2002) for discussion of this object.

Table 8. 50 Brightest NICMOS Clusters

#	ID	RA	DEC	$M_V^a$	$C$	$U-B$	$V-I$	$F110W$	$F160W$	$F222M$	$E(B-V)$	$\text{Log } \tau$	Mass <sup>a</sup>	comments
(1)	(2)	(3)	(4)	(5)	(6)	(7)	(8)	(9)	(10)	(11)	(12)	(13)	(14)	(15)
1	32604	12:01:55.4307	-18:52:19.476	-12.68 (11)	1.65	-0.77	0.57	17.92	16.87	16.25	0.06	7.70	1.6 E6 (12)	Region 7
2	36731	12:01:55.9896	-18:52:12.985	-12.54 (13)	1.66	-0.81	0.59	17.92	16.88	16.29	0.04	7.63	1.1 E6 (21)	Region 6
3	19807	12:01:55.2762	-18:52:48.952	-8.83	1.65	—	2.71	18.48	16.89	16.28	1.00	10.30 <sup>b</sup>	— <sup>b</sup>	near Knot C
4	15466	12:01:54.6439	-18:53:04.958	-11.70 (44)	1.84	-1.33	0.22	17.39	16.97	15.94	0.38	6.08	4.2 E5	Knot B
5	24126	12:01:54.8838	-18:52:34.669	-12.02 <sup>c</sup>	1.39 <sup>c</sup>	1.59	1.49	18.01	17.02	16.93	0.34	10.30 <sup>b</sup>	— <sup>b</sup>	Region 2
6	25439	12:01:55.3483	-18:52:31.510	-11.37	1.77	0.64	1.14	18.22	17.15	16.42	0.02	10.30 <sup>b</sup>	— <sup>b</sup>	Region 2
7	25895	12:01:55.4406	-18:52:30.513	-11.63 <sup>c</sup>	1.51 <sup>c</sup>	0.63	1.11	18.30	17.23	16.60	0.00	10.27 <sup>b</sup>	— <sup>b</sup>	Region 2
8	15398	12:01:54.5335	-18:53:05.193	-12.20 (20)	1.72	-0.74	0.63	18.19	17.24	16.75	0.12	7.68	1.2 E6 (20)	Knot B
9	31730	12:01:55.5385	-18:52:20.760	-11.31	1.74	-0.45	1.16	18.47	17.27	16.51	0.50	7.74	1.7 E6 (8)	Region 7
10	28556	12:01:53.1260	-18:52:25.650	-12.16 (22)	1.68	-0.92	0.53	18.35	17.34	16.78	0.00	7.51	6.6 E5 (42)	Region 8
11	36270	12:01:55.1438	-18:52:13.650	-9.09	1.64	-1.44	2.07	18.70	17.36	16.66	0.82	6.96	1.9 E5	Region 7
12	33952	12:01:55.2903	-18:52:17.375	-5.58	1.22	0.55	3.86	19.38	17.41	16.38	2.10	6.96	2.5 E5	Region 7
13	38220	12:01:53.0075	-18:52:10.829	-14.20 (3)	1.52	-1.75	-0.14	17.75	17.41	16.83	0.08	6.76	9.2 E5 (28)	Knot K
14	31569	12:01:55.5458	-18:52:20.993	-9.24	1.76	-0.58	0.68	18.43	17.43	16.81	0.22	8.01	1.6 E5	Region 7
15	50277	12:01:54.9046	-18:51:48.495	-12.35 <sup>c</sup>	1.43 <sup>c</sup>	1.22	1.08	18.29	17.48	17.16	0.12	10.30 <sup>b</sup>	— <sup>b</sup>	Region 9
16	14612	12:01:55.0360	-18:53:07.529	-7.79	1.67	-1.70	3.16	18.70	17.49	15.89	2.44	6.00	6.8 E6 (1)	“WS80” <sup>d</sup> , near Knot B
17	41030	12:01:53.0442	-18:52:06.195	-11.17	1.66	-0.53	0.67	18.63	17.49	16.82	0.22	8.01	9.4 E5 (27)	Knot J
18	33331	12:01:55.1975	-18:52:18.356	-8.19	1.60	—	2.62	19.13	17.53	16.74	0.94	10.30 <sup>b</sup>	— <sup>b</sup>	Region 7
19	32187	12:01:55.2607	-18:52:20.093	-11.28	1.65	-0.13	0.93	18.67	17.55	16.90	0.30	8.31	1.9 E6 (7)	Region 7
20	41285	12:01:53.1005	-18:52:05.728	-9.73	1.84	-0.65	0.73	18.87	17.60	17.05	0.82	6.60	1.4 E5	Knot J
21	42257	12:01:53.1051	-18:52:03.964	-11.35	1.58	-0.28	0.70	18.23	17.61	16.95	1.08	6.50	1.4 E6 (14)	Knot J
22	46102	12:01:53.2415	-18:51:56.508	-11.44	1.74	-1.39	0.39	18.71	17.63	17.09	0.00	6.86	8.1 E4	Knot H
23	45889	12:01:54.3092	-18:51:56.879	-12.26 (16)	1.60	-0.95	0.49	18.63	17.67	17.30	0.00	7.51	7.2 E5 (38)	Region 9
24	19825	12:01:54.6356	-18:52:48.902	-7.66	1.71	2.98	3.12	19.19	17.67	17.07	1.28	10.30 <sup>b</sup>	— <sup>b</sup>	Region 2
25	29516	12:01:55.6342	-18:52:24.141	-12.06 (24)	1.58	-0.79	0.44	18.73	17.69	17.28	0.00	7.81	8.5 E5 (31)	Knot E
26	42620	12:01:53.1623	-18:52:03.366	-7.81	1.83	—	2.55	19.21	17.72	16.85	1.90	6.60	5.2 E5	Knot J
27	29410	12:01:55.4840	-18:52:24.273	-11.62 (46)	1.64	-0.58	0.64	18.78	17.73	17.27	0.18	7.91	1.1 E6 (23)	Knot E
28	18848	12:01:54.8341	-18:52:52.841	-7.66	1.67	0.56	3.02	19.29	17.79	17.01	2.20	6.68	1.2 E6 (19)	near Knot C
29	29955	12:01:55.6571	-18:52:23.458	-11.19	1.65	-0.95	0.59	18.89	17.82	17.24	0.04	7.51	3.0 E5	Knot E
30	19330	12:01:55.4291	-18:52:50.871	-11.39	1.85	-1.60	0.41	18.33	17.85	17.01	0.34	6.16	3.2 E5	Knot C
31	29090	12:01:55.6321	-18:52:24.812	-11.49	1.66	-0.84	0.59	18.96	17.94	17.46	0.04	7.60	4.3 E5	Knot E
32	21464	12:01:55.1483	-18:52:42.579	-12.06 (25)	1.78	-0.37	0.45	18.82	17.97	17.67	0.00	8.31	1.6 E6 (11)	Region 2
33	34907	12:01:55.7695	-18:52:15.723	-10.41	1.78	-1.37	0.14	18.88	17.97	17.38	0.00	6.72	2.2 E4	Region 5
34	38235	12:01:54.8023	-18:52:10.810	-11.06	1.55	-0.48	0.92	19.13	18.00	17.44	0.18	8.11	8.2 E5 (33)	Knot F
35	38639	12:01:53.0355	-18:52:10.223	-13.27 (4)	1.67	-1.16	0.00	18.35	18.05	17.62	0.00	6.78	3.3 E5	Knot K
36	11721	12:01:55.0537	-18:53:16.055	-10.68	1.51	-0.78	1.30	19.29	18.05	17.02	0.42	7.34	4.4 E5	near Knot B
37	29784	12:01:55.9339	-18:52:23.711	-11.86 (34)	1.66	-0.69	0.54	19.04	18.09	17.61	0.04	7.81	7.9 E5 (35)	Region 4
38	32364	12:01:55.7614	-18:52:19.797	-12.18 (21)	1.55	-0.83	0.36	19.06	18.09	17.55	0.00	7.72	8.5 E5 (30)	Region 4
39	28435	12:01:55.5053	-18:52:25.815	-10.58	1.81	-1.03	0.52	19.13	18.12	17.49	0.50	6.56	1.1 E5	Knot E
40	35410	12:01:54.9067	-18:52:14.959	-10.97	1.52	-0.92	0.98	18.90	18.16	17.71	0.62	6.74	2.4 E5	Knot F
41	40436	12:01:55.3956	-18:52:07.226	-11.21	1.71	-0.43	0.73	19.24	18.19	17.84	0.10	8.16	8.0 E5 (34)	Region 7
42	38372	12:01:54.5174	-18:52:10.592	-11.97 (29)	1.62	-1.00	0.29	19.23	18.23	17.55	0.10	6.80	1.5 E5	Knot F
43	31419	12:01:56.0175	-18:52:21.251	-11.17	1.71	-0.62	0.69	19.25	18.23	17.81	0.04	8.11	6.0 E5 (46)	Region 4
44	35561	12:01:55.0547	-18:52:14.710	-10.49	1.63	-0.25	0.95	19.35	18.24	17.52	0.46	8.06	1.1 E6 (25)	Knot F
45	22708	12:01:55.4540	-18:52:38.755	-10.56 <sup>c</sup>	1.49 <sup>c</sup>	-0.10	0.96	19.42	18.29	17.75	0.34	8.36	1.1 E6 <sup>c</sup>	Region 2

Table 8—Continued

# (1)	ID (2)	RA (3)	DEC (4)	$M_V^a$ (5)	$C$ (6)	$U-B$ (7)	$V-I$ (8)	$F110W$ (9)	$F160W$ (10)	$F222M$ (11)	$E(B-V)$ (12)	Log $\tau$ (13)	Mass <sup>a</sup> (14)	comments (15)
46	31216	12:01:56.2315	-18:52:21.543	-11.20	1.77	-0.44	0.68	19.22	18.29	17.94	0.10	8.16	7.8 E5 (36)	Region 4
47	30673	12:01:56.2076	-18:52:22.386	-10.23	1.77	0.04	1.18	19.45	18.30	17.84	0.48	8.41	1.4 E6 (16)	Region 4
48	22079	12:01:56.3823	-18:52:40.601	-11.28	1.67	-0.90	0.50	19.37	18.31	17.73	0.28	6.76	1.1 E5	Region 3
49	50088	12:01:53.3190	-18:51:48.866	-11.51	1.66	-0.94	0.53	19.30	18.32	17.87	0.00	7.57	3.8 E5	Knot N
50	38583	12:01:52.7265	-18:52:10.300	-11.52	1.59	-0.73	0.44	19.39	18.33	17.66	0.02	7.91	6.1 E5 (45)	near Knot K

<sup>a</sup>Values in parentheses are the rank order from Table 6 or 7, as appropriate.

<sup>b</sup>Very questionable age estimate.

<sup>c</sup>Missing in Table 6 and/or Table 7 due to value of  $C < 1.52$ . Hence, it is possible that some of these are stars.

<sup>d</sup>See Whitmore & Zhang (2002) for discussion of this object.

Table 9. Properties of Knots, Regions, and Outer Areas

ID	Class <sup>a</sup>	$N$	$N_9^b$	$M_V(Bright)$	$\text{Log } \tau^c$	$\sigma^d$	$E(B-V)^c$	$\alpha$	$\beta$	Range <sup>e</sup>
(1)	(2)	(3)	(4)	(5)	(6)	(7)	(8)	(9)	(10)	(11)
Star Forming Knots										
A	2	94	32	–11.60	6.74	0.91	0.30	–2.10	–1.95	6–7
B	3	46	31	–12.39	6.61	0.79	0.40	–1.60	–1.70	6–7
C	2	27	15	–11.90	6.02	0.48	0.32	–1.80	–1.60	6–7
D	1	48	22	–13.07	6.40	0.67	0.33	–2.00	–1.90	6–7
E	2	87	35	–12.06	7.60	0.83	0.20	–1.90	–2.10	6–7
F	1	80	38	–12.93	6.58	0.71	0.21	–2.00	–2.30	6–7
G	1	128	37	–14.45	6.81	0.83	0.13	–2.20	–2.30	6–7
H	1	39	17	–11.44	7.51	0.67	0.05	–2.20	–2.20	6–7
I	2	18	—	—	6.64	0.97	0.46	—	—	—
J	3	27	15	–11.85	6.52	1.10	0.64	—	–1.75	6–7
K	1	19	—	—	6.52	0.38	0.25	—	—	—
L	3	79	18	–12.04	6.70	0.88	0.25	–1.90	–2.10	6–7
M	2	160	34	–12.25	6.70	0.80	0.27	–1.90	–2.30	6–7
N	2	90	14	–10.83	6.79	0.67	0.15	–2.20	–2.00	6–7
P	2	122	9	–11.92	6.90	0.74	0.11	–2.50	–2.30	6–7
R	2	89	27	–12.71	6.74	0.81	0.22	–2.00	–2.00	6–7
S	1	96	34	–14.63	6.76	0.76	0.17	–2.10	–2.00	6–7
T	3	93	60	–12.11	6.74	0.66	0.15	–1.60	–1.60	6–7
Regions										
1	2	53	16	–11.60	6.74	0.81	0.34	–2.15	–2.17	6–7
2	—	201	18	–12.06	7.96	1.42	0.34	–2.30	–2.60	6–7
3	1	84	11	–11.28	6.78	0.90	0.26	–2.10	–2.05	6–7
4	2	118	14	–11.86	7.88	0.65	0.09	–2.00	–1.90	7.5–8.5
5	2	40	18	–11.42	6.91	0.64	0.09	–1.70	–1.80	6–7
6	1	21	8	–12.87	7.51	0.86	0.05	—	—	—
7	—	279	38	–12.68	7.74	0.88	0.17	–2.00	–2.00	7.5–8.5
8	—	—	5	–11.37	8.31	1.31	0.29	–2.10	—	—
9	—	277	25	–12.27	7.46	0.86	0.12	–1.90	–2.00	6–7
10	—	286	10	–10.01	7.51	0.82	0.12	–1.70	–1.50	7–8
11	—	—	6	–10.28	7.32	1.09	0.16	–2.40	–2.10	6–7
12	—	114	7	–10.54	8.36	0.94	0.14	–2.25	–2.10	7.5–8.5

Table 9—Continued

ID	Class <sup>a</sup>	$N$	$N_9^b$	$M_V(Bright)$	$\text{Log } \tau^c$	$\sigma^d$	$E(B-V)^c$	$\alpha$	$\beta$	Range <sup>e</sup>
(1)	(2)	(3)	(4)	(5)	(6)	(7)	(8)	(9)	(10)	(11)
13	2	30	8	−10.87	6.66	0.83	0.26	−1.80	−1.75	6–7
14	—	320	44	−12.83	6.91	0.97	0.26	−2.00	−1.90	6–7
15	2	28	2	−11.22	7.66	0.77	0.23	−2.10	−2.50	6–7
Outer Areas										
1	—	216	14	−11.50	7.96	0.77	0.10	−2.30	−2.17	7.5–8.5
2	—	57	—	—	8.36	0.96	0.06	−2.20	−2.30	8–9
3	—	35	1	−9.29	8.26	0.60	0.05	−2.00	−1.90	8–9
4	—	22	2	−10.71	8.31	0.45	0.04	−2.20	−2.30	8–9
5	—	92	7	−10.26	8.36	0.88	0.06	−2.10	−2.10	8–9
6	—	37	5	−9.44	8.36	0.59	0.03	−2.10	−1.90	8–9
7	—	51	4	−10.92	8.06	0.80	0.06	−2.20	−2.10	8–9
8	—	16	1	−9.11	8.33	0.33	0.05	—	—	—
9	—	—	5	−10.21	8.33	0.20	0.02	−2.00	−1.90	8–9
10	—	43	1	−9.20	8.31	0.77	0.03	−2.30	−2.10	8–9

<sup>a</sup>1 = has very dominant cluster(s), 2 = has dominant cluster(s), 3 = has no dominant cluster(s), — = not relevant since a general region rather than single cluster complex.

<sup>b</sup>Number of clusters with  $M_V < -9$ .

<sup>c</sup>Median

<sup>d</sup>Dispersion in  $\text{Log } \tau$ . Note that low values signify a single- rather than multi-age population.

<sup>e</sup>Range in  $\text{Log } \tau$  used in determination of  $\alpha$  and  $\beta$ .

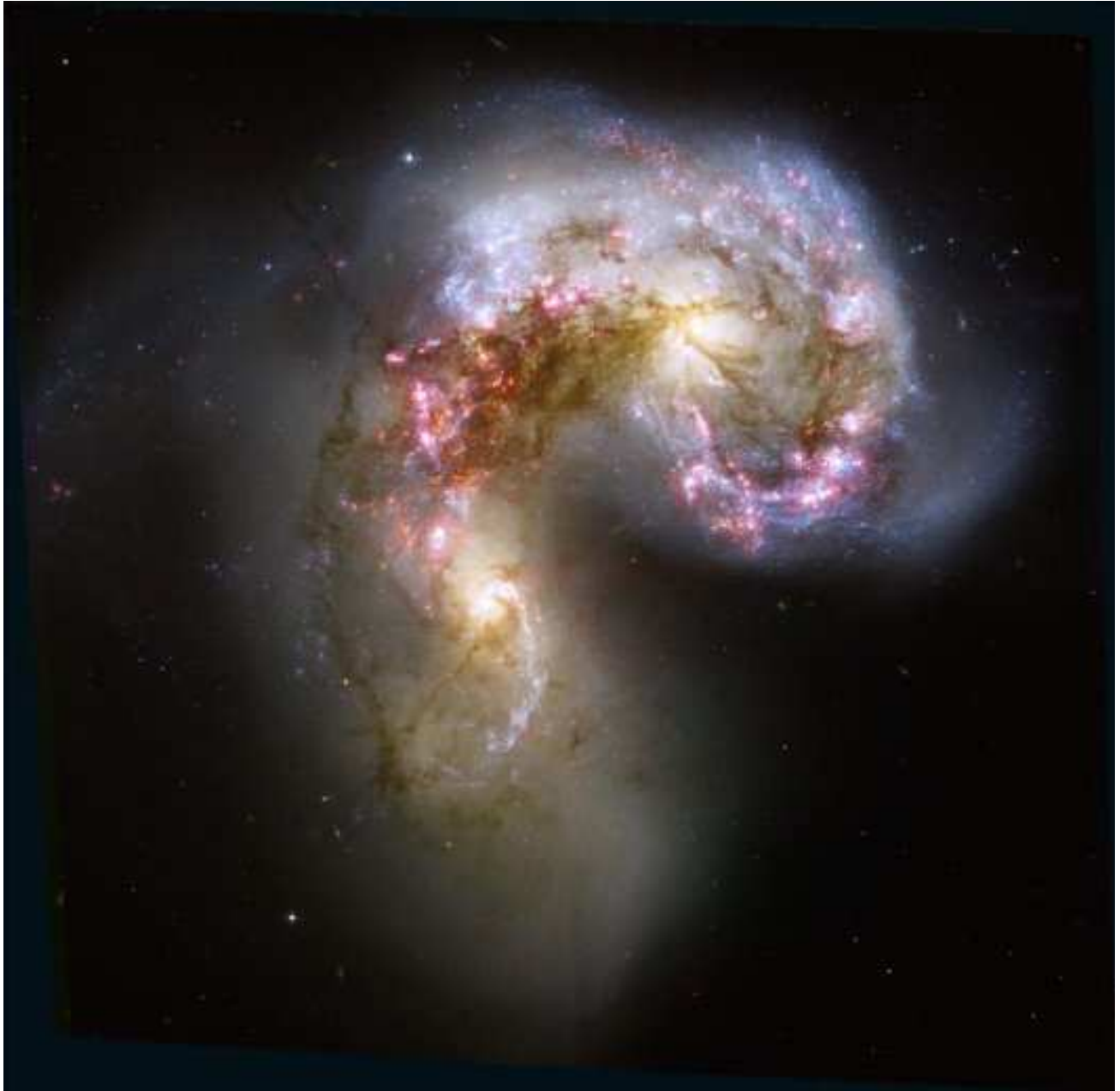


Fig. 1.— Color image of NGC 4038/4039 produced by Lars Christensen (ESA). The F435W image is shown in blue, the F550M image in green, and a combination of the F814W and  $H\alpha$  images in red.

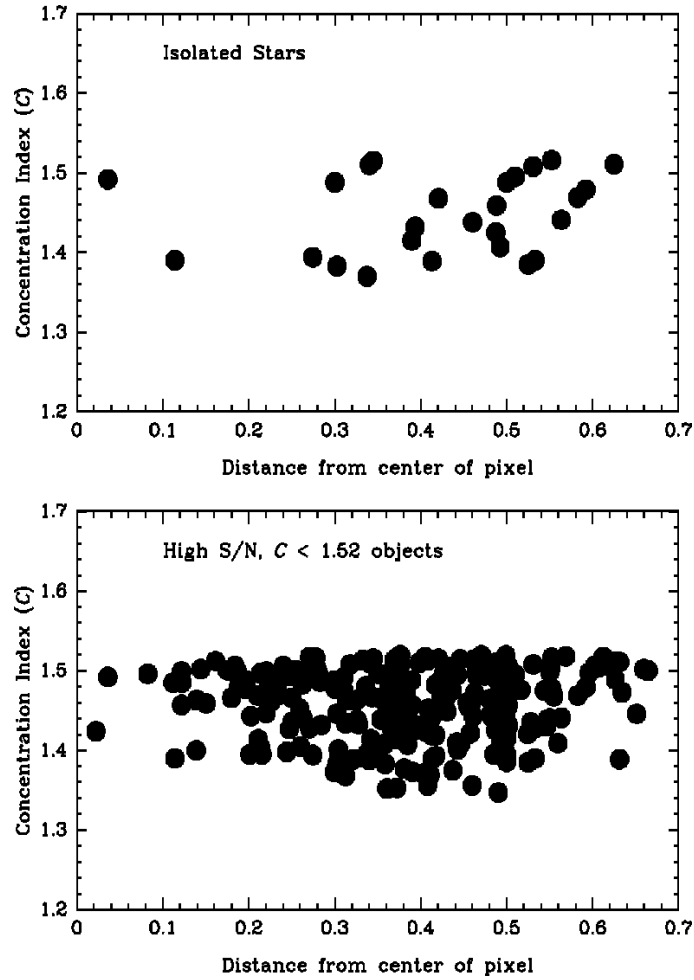


Fig. 2.— Values of the concentration index  $C$ , the difference between magnitudes measured within a one and a three pixel radius, are plotted versus the positions of objects relative to the pixel center for (a) a sample of 26 isolated foreground stars and (b) candidate stars selected for having values of  $C < 1.52$  and  $V < 23$  mag. Note that there are no clear trends, contrary to the claims made by Anders et al. (2002).

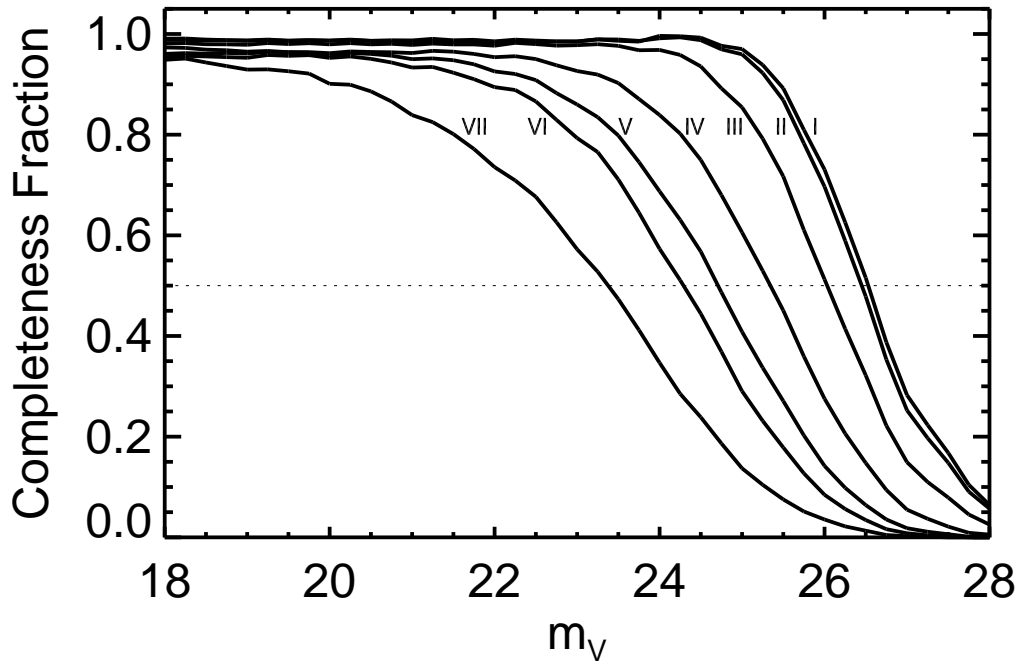


Fig. 3.— Completeness curves as determined from artificial object experiments for different background levels. The background levels (in units of electrons  $s^{-1}$ ) are:  $0 \leq \mathbf{I} \leq 0.014$ ;  $0.014 < \mathbf{II} \leq 0.020$ ;  $0.020 < \mathbf{III} \leq 0.040$ ;  $0.040 < \mathbf{IV} \leq 0.060$ ;  $0.060 < \mathbf{V} \leq 0.090$ ;  $0.090 < \mathbf{VI} \leq 0.120$ ; and  $\mathbf{VII} > 0.120$ .



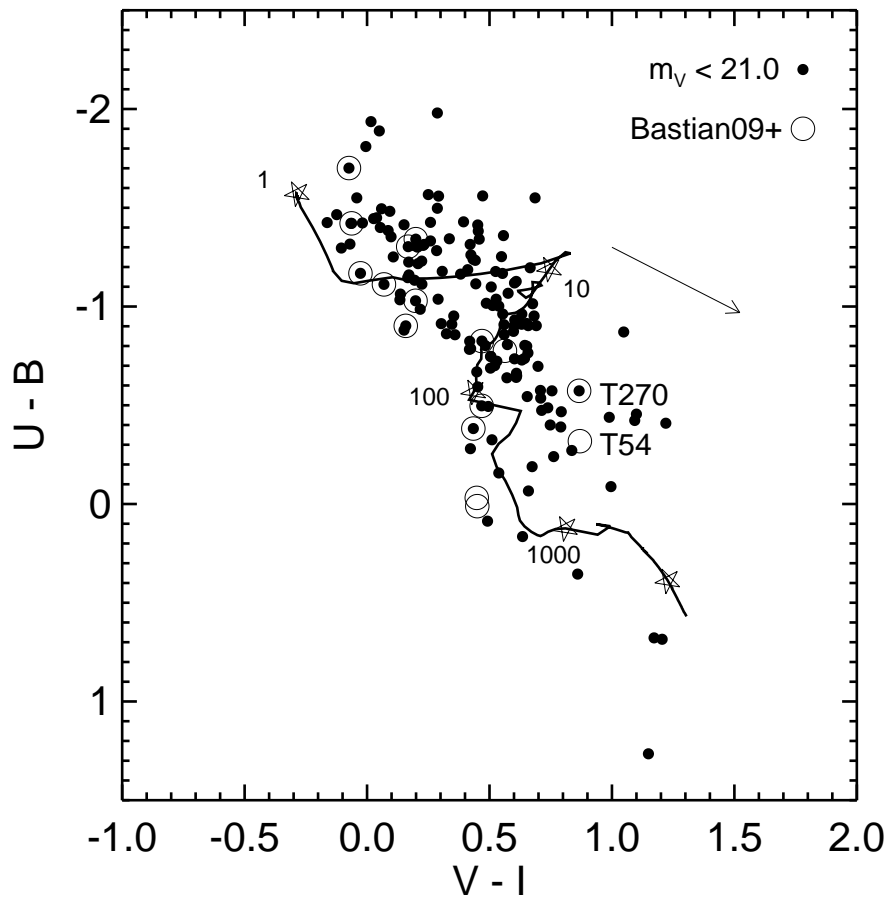


Fig. 4.—  $U-B$  vs.  $V-I$  diagram for the 160 brightest candidate clusters in the Antennae. The solid line shows the evolutionary track of a CB07 model cluster of solar metallicity, with open stars denoting cluster ages of  $10^6$ ,  $10^7$ ,  $10^8$ ,  $10^9$ , and  $10^{10}$  yrs (labeled in Myr in the figure). Circled points also have spectroscopic observations by Bastian et al. (2009), providing independent age estimates. A few of the Bastian et al. clusters are not in our sample of the brightest 160 clusters, whence they do not feature a data point at the center of the circle. The arrow shows the reddening vector for  $A_V = 1.0$  mag. For details, see text.

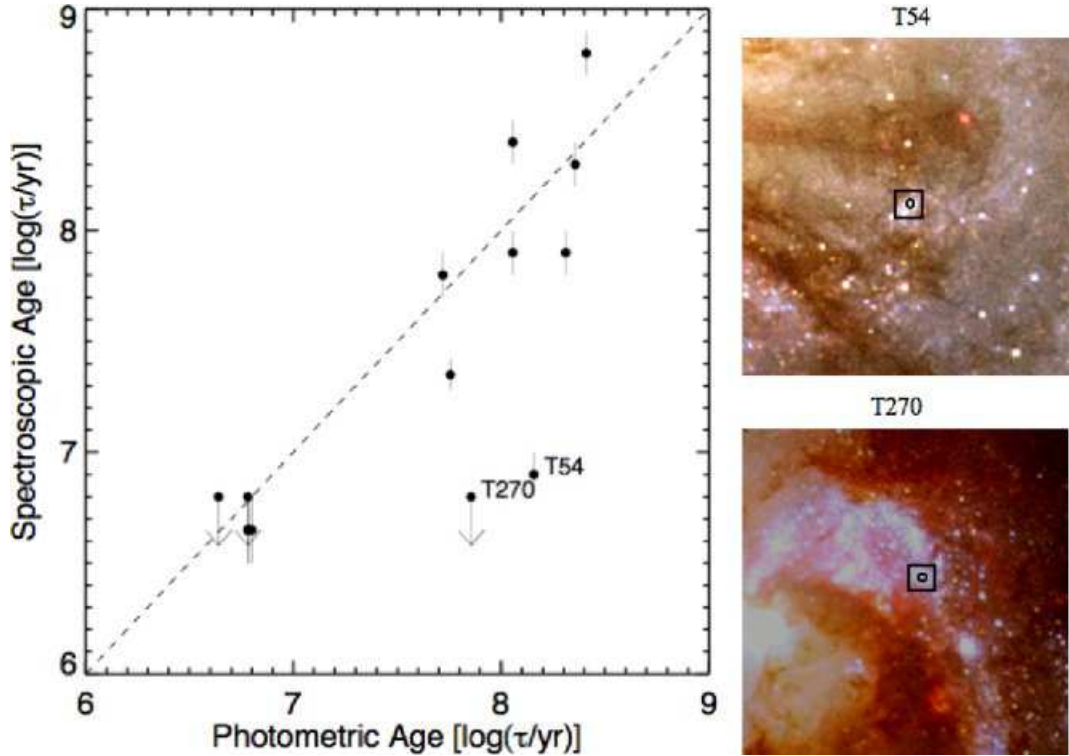


Fig. 5.— Comparison between spectroscopic estimates of cluster ages by Bastian et al. (2009) and our photometric age estimates for 15 clusters (note that four data points overlay each other near [6.78, 6.65]). Images of the two outliers T54 and T270 are shown to the right, with our aperture size (radius =  $0''.09$ ) marked by the small circles, and the approximate aperture (slit width =  $0''.75$ ; no correction for ground-based seeing) used by Bastian et al. (2009) marked by the larger squares. For details, see text.

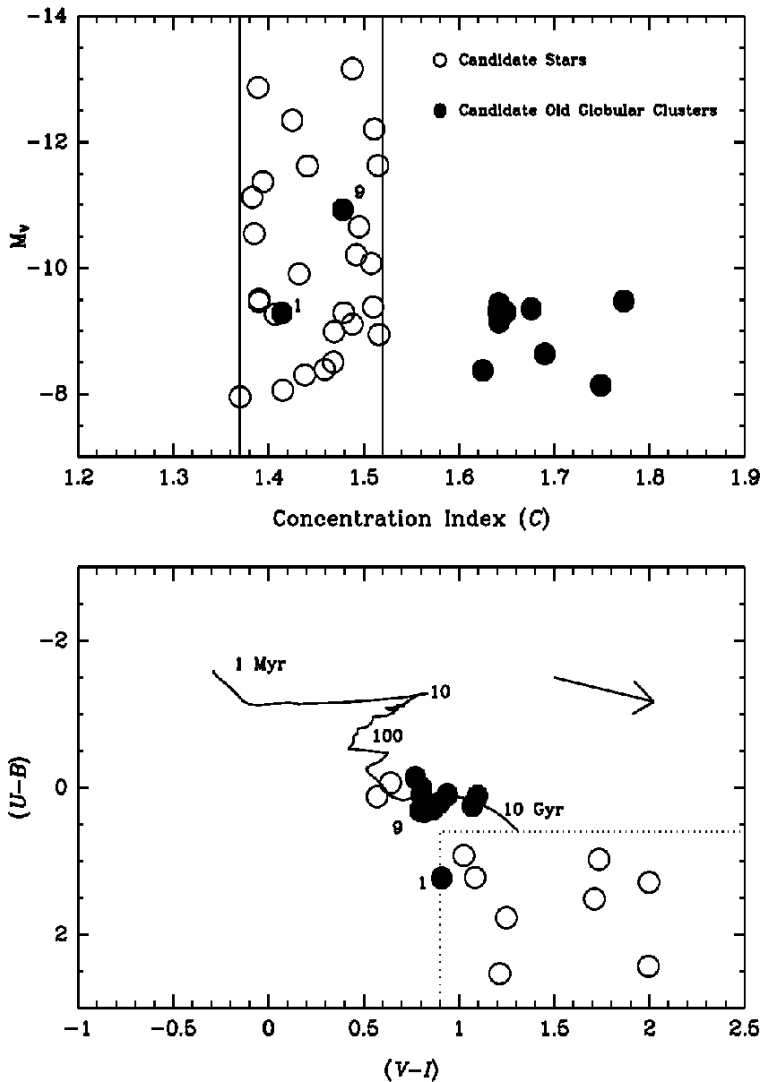


Fig. 6.— Properties for Training Set 1, which consists of hand-selected stars (open circles) and candidate old globular clusters (filled circles) from Whitmore et al. (1999) in the field of the Antennae galaxies. The upper panel shows the computed absolute magnitude  $M_V$  plotted vs. concentration index  $C$ , while the lower panel shows a two-color plot,  $U-B$  vs.  $V-I$ , for the same objects. The arrow marks a reddening corresponding to  $A_V = 1$  mag, assuming a standard Galactic extinction law, while the solid line shows the evolutionary track of a CB07 model star cluster of solar metallicity.

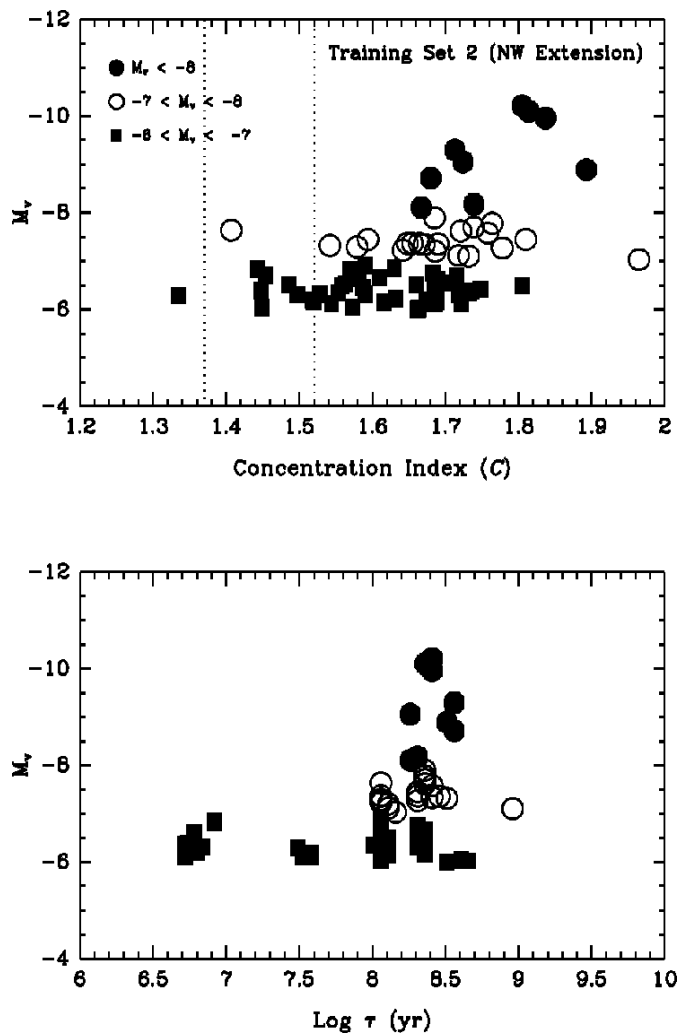


Fig. 7.— Properties for Training Set 2 (in NW Extension), which is dominated by intermediate-age clusters. The upper panel shows that bright sources have concentration indices  $C$  expected of clusters. At fainter magnitudes increased observational scatter results in some objects falling into (or even below!) the star category. This demonstrates that using size alone to distinguish stars from clusters breaks down at  $M_V \approx -7$  for isolated objects. Similarly, the bottom panel shows that the age determination breaks down at  $M_V \approx -7$ , since none of the plotted objects are believed to have ages of  $\log \tau < 8.0$ .

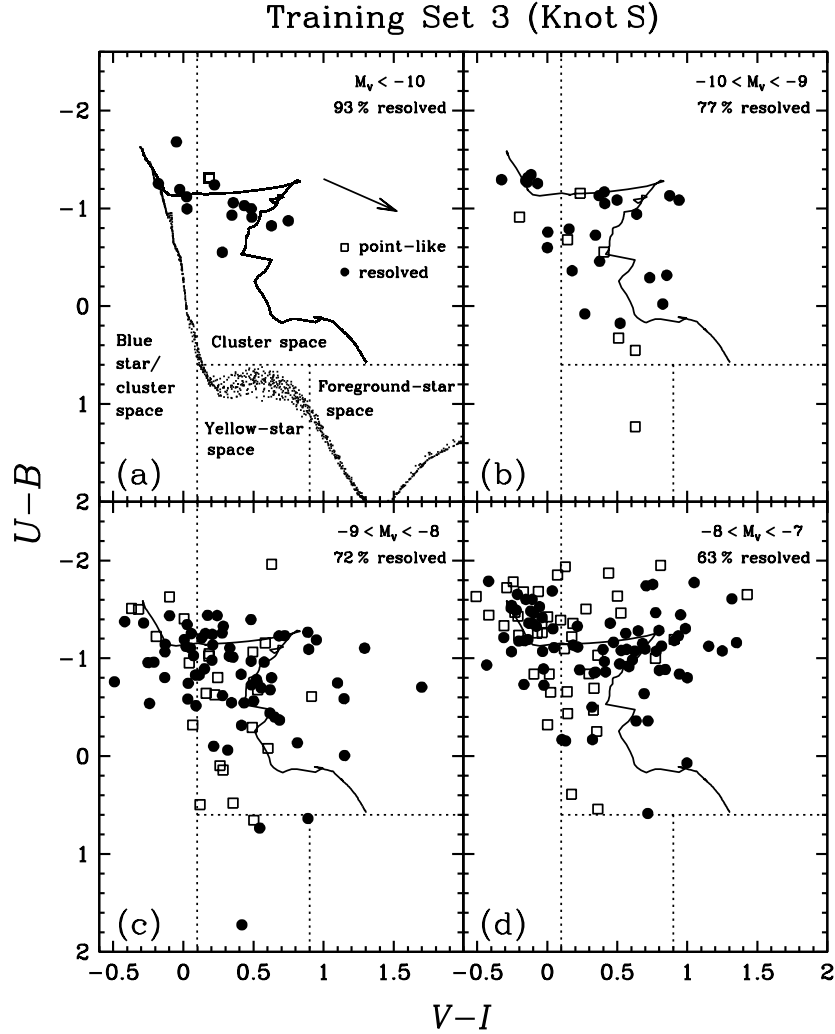


Fig. 8.—  $U-B$  vs.  $V-I$  two-color diagrams for objects around Knot S. Resolved objects (i.e.,  $C > 1.52$ ) are shown as filled circles and unresolved objects as open squares. The four panels show objects in different luminosity ranges. The solid lines in each panel show CB07 evolutionary tracks for clusters of solar metallicity, while the dots in Panel (a) show Padova model colors for stars brighter than  $M_V = -7$ . The dotted lines show the regions of the diagram used to define cluster space, foreground-star space, yellow-star space, and blue-star/cluster space, as discussed in the text.

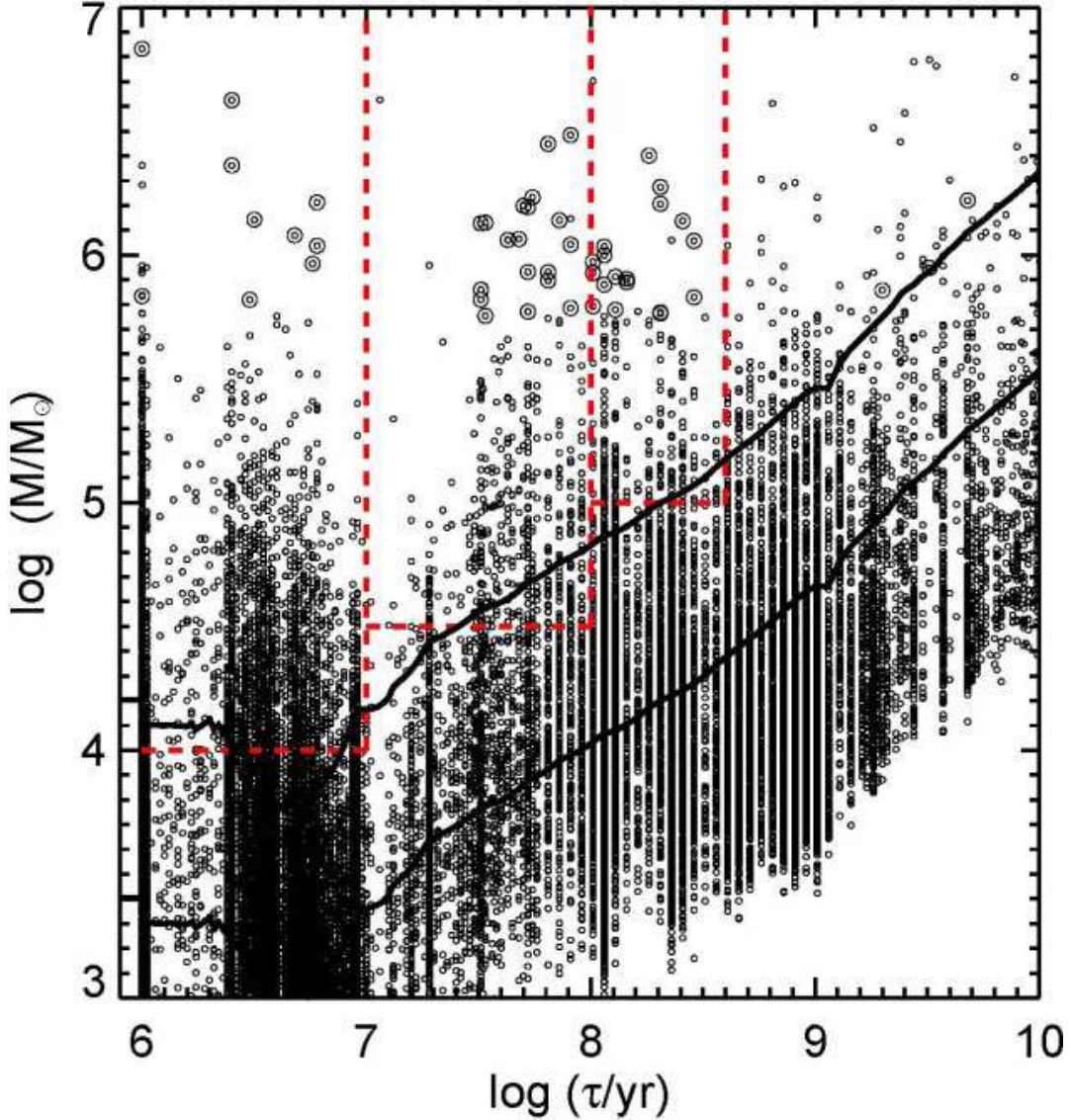


Fig. 9.— Log Mass vs.  $\log \tau$  diagram for clusters in the Antennae. The solid black lines show completeness curves for  $M_V = -9$  (to exclude stars based on luminosity alone) and  $M_V = -7$  (where age and size estimates become difficult). The dashed red lines show the bins used for the MF determinations in Figure 15. The 50 most massive candidate clusters from Table 7 are circled. Some artifacts (e.g., stars, the nuclei of the two galaxies, etc.) have been removed from the sample based on visual inspection. In addition, many of the apparently massive sources with  $\log \tau > 8.6$  are likely to be younger clusters with strong foreground extinction, as discussed in the text, and hence are not included in Table 8 or circled in this figure.

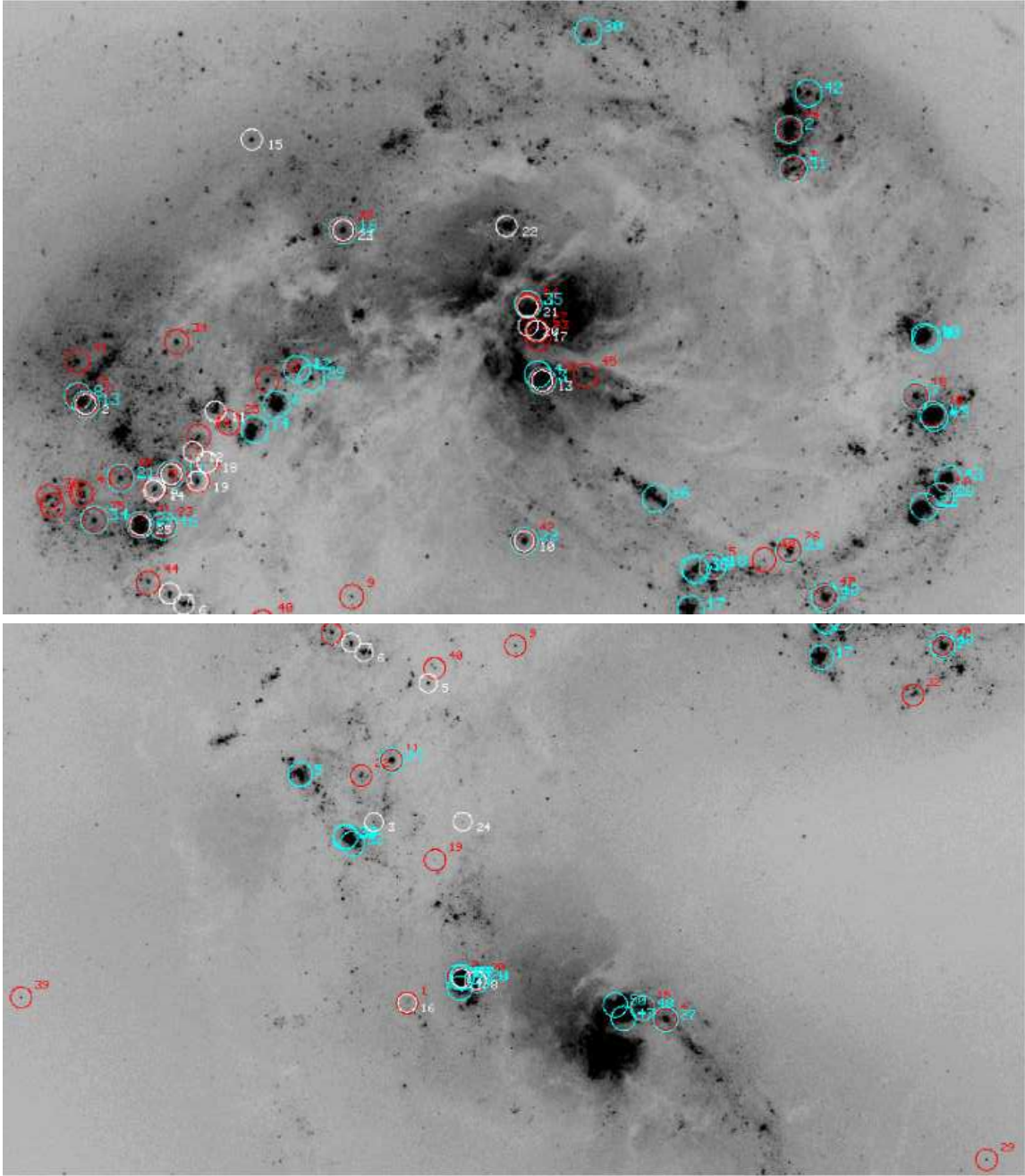


Fig. 10.— (a) Top half of the Antennae (NGC 4038) with the 50 most luminous clusters (blue circles) and the 50 most massive clusters (red circles) marked (see Tables 6 and 7). (b) Same information as in (a), but for the bottom half of the Antennae (NGC 4039). Also marked are the 25 most IR-bright clusters (white circles, see Table 8). Their number has been scaled down since the FOV for NICMOS observations was only about half that covered by the ACS observations (see also Figure 11).

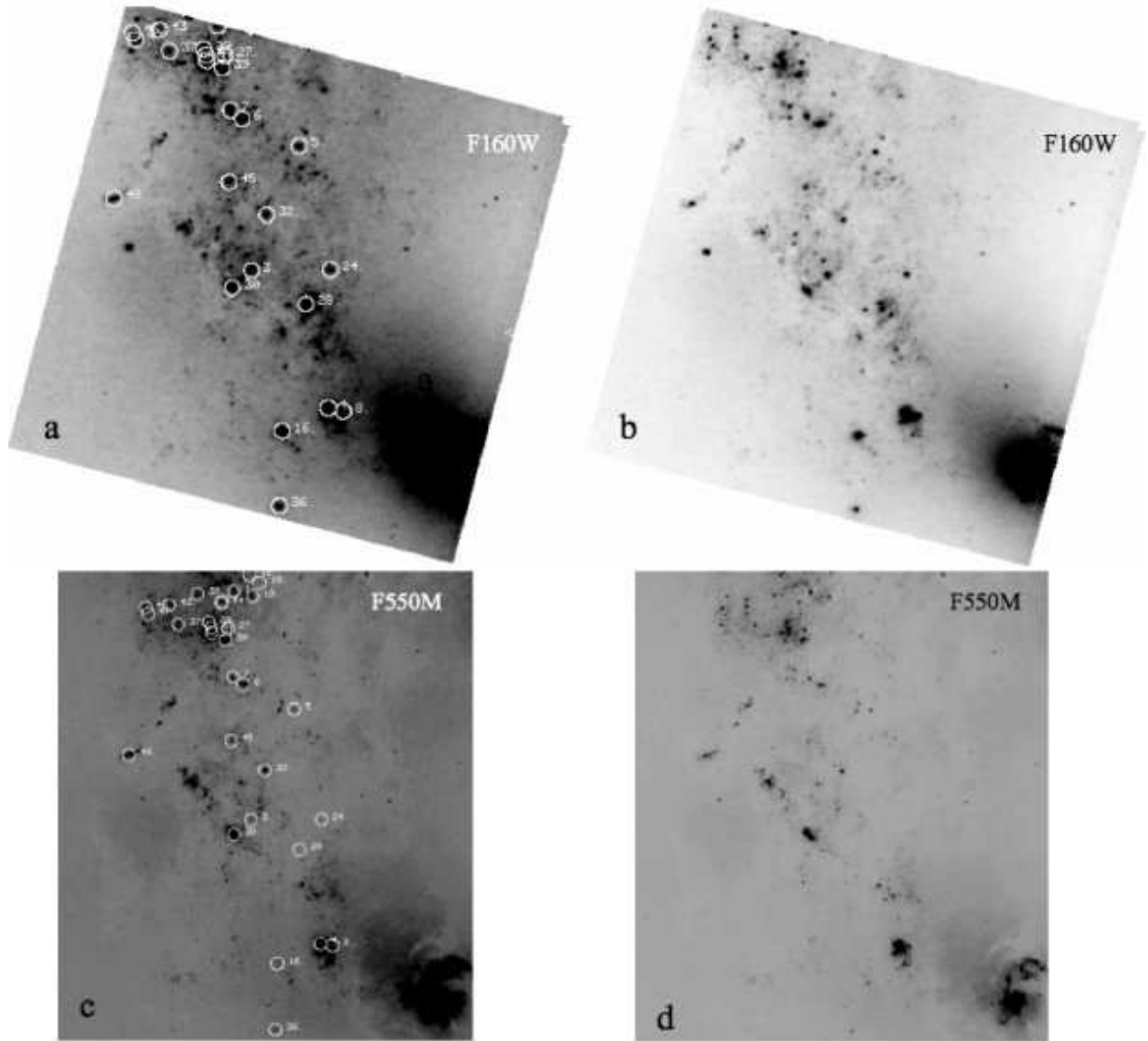


Fig. 11.— NICMOS field No. 1, which includes the nucleus of NGC 4039. Panels a and b show different-contrast renditions of the F160W image, with and without the brightest IR clusters from Table 8 identified by circles. Panels c and d show similar FOVs, taken from the F550M image obtained with ACS.



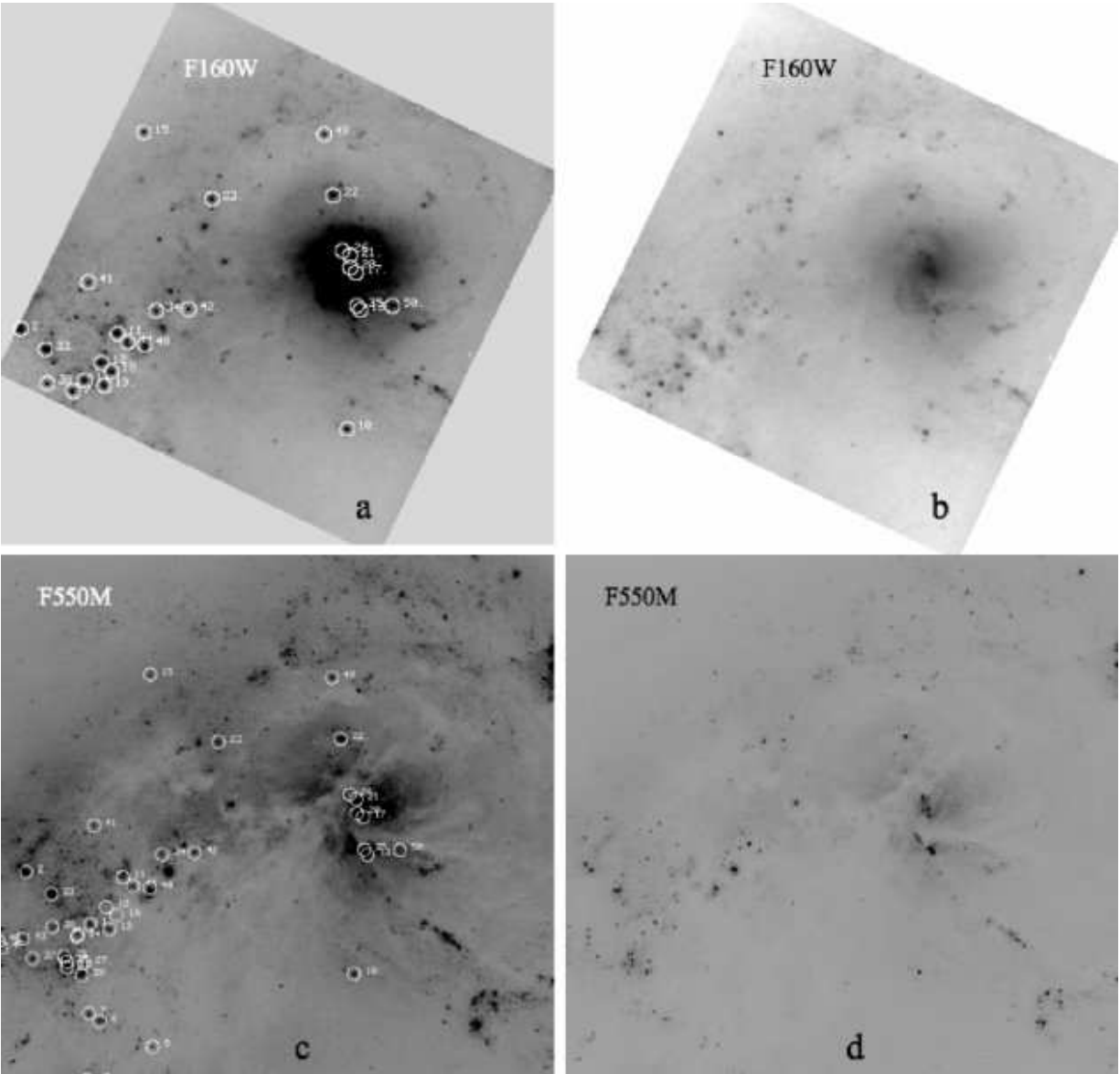


Fig. 12.— Similar to Figure 11, but for NICMOS field No. 2, which includes the nucleus of NGC 4038.

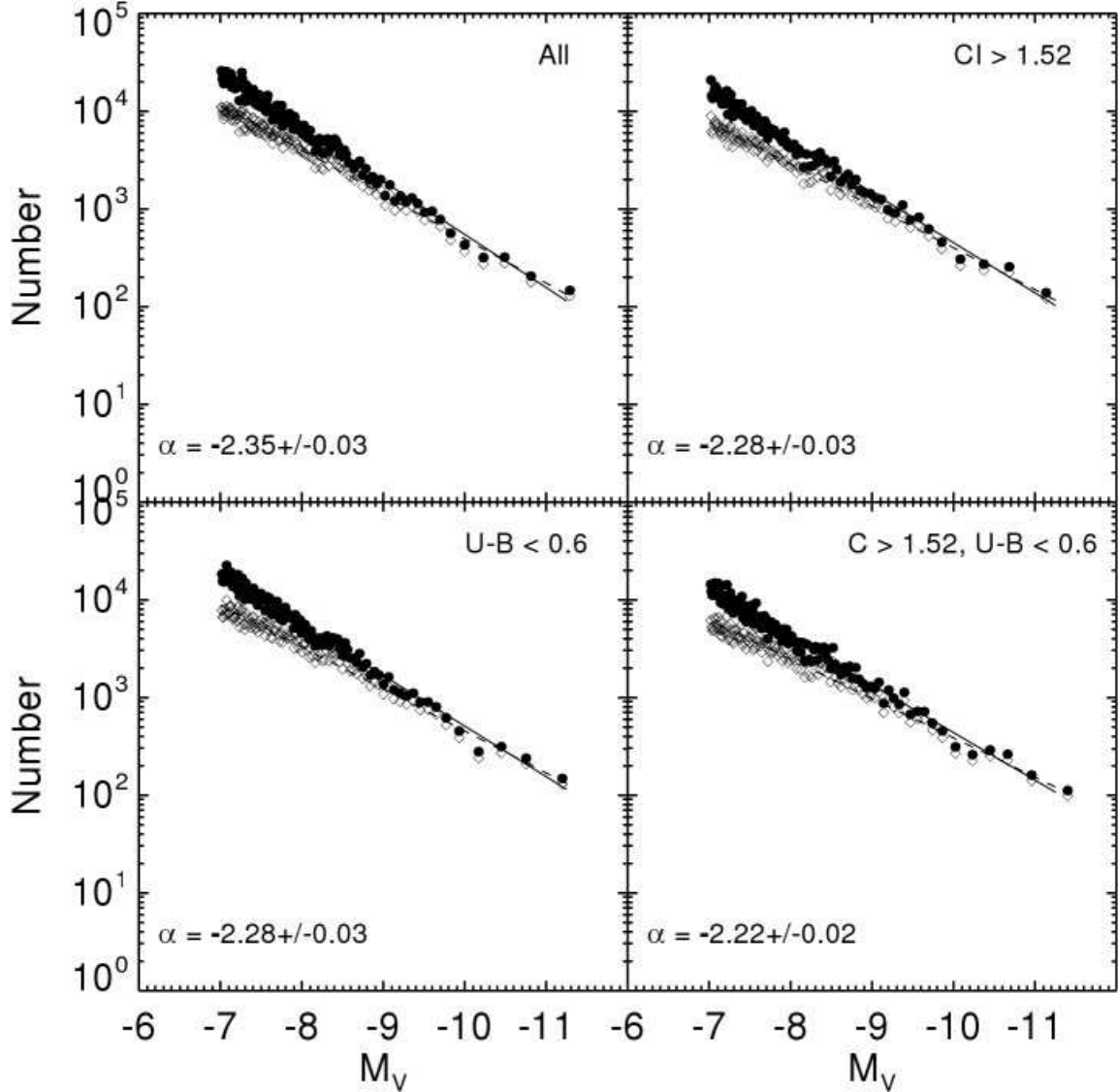


Fig. 13.— Luminosity functions for objects across the entire galaxy: (a) LF for all detected objects (i.e., a mix of individual stars and star clusters); (b) LF only for resolved objects ( $C > 1.52$ ); (c) LF for objects with  $U - B$  colors that place them in “cluster space” or “blue-star/cluster space”; and (d) LF for objects selected by both size and  $U - B$  color to be likely young clusters. Variable-binning is used with open circles showing observed data and filled circles showing completeness corrected data. Values of  $\alpha$  are for the completeness corrected fits to the data.

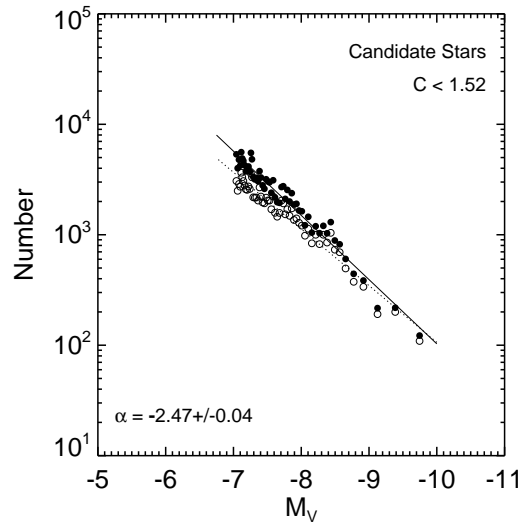


Fig. 14.— Luminosity function for candidate stars ( $C < 1.52$ ) across the entire galaxies.

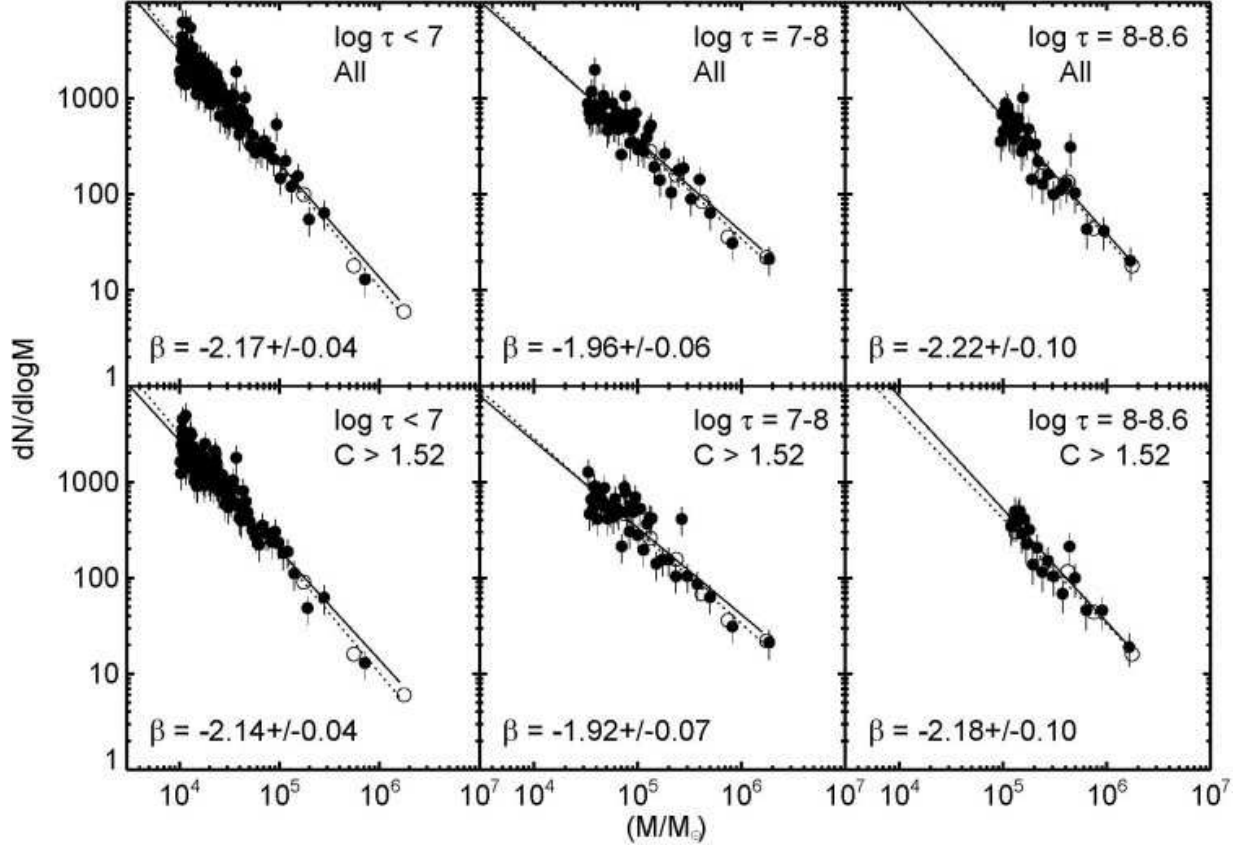


Fig. 15.— The top panels show the mass functions for clusters in the Antennae for three different age intervals, using the bins shown by the dashed red lines in Figure 9. The bottom panels show the corresponding mass functions for only the resolved clusters ( $C > 1.52$ ). The solid lines mark best fits to the variable-binning data (filled circles), while the dashed lines mark best fits to the fixed-binning data (open circles). The values of  $\beta$  given are for the variable-binning data.

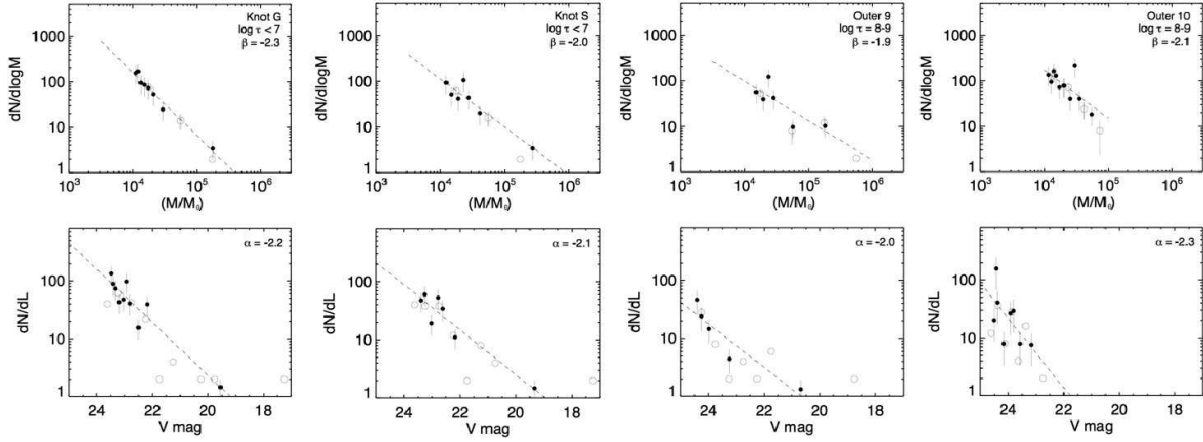


Fig. 16.— (top row) Cluster mass functions for age ranges corresponding to the dominant-age population in each of four representative areas, and (bottom row) the corresponding cluster luminosity functions. The dashed lines mark best fits to the variable-binning data (filled circles).

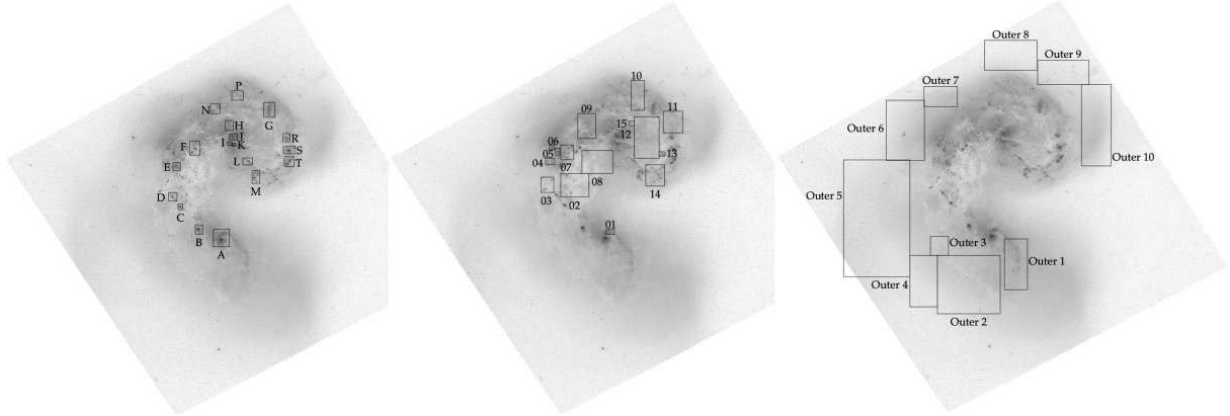


Fig. 17.— Locations of the star forming knots (letters), regions (numbers), and outer areas in the Antennae.

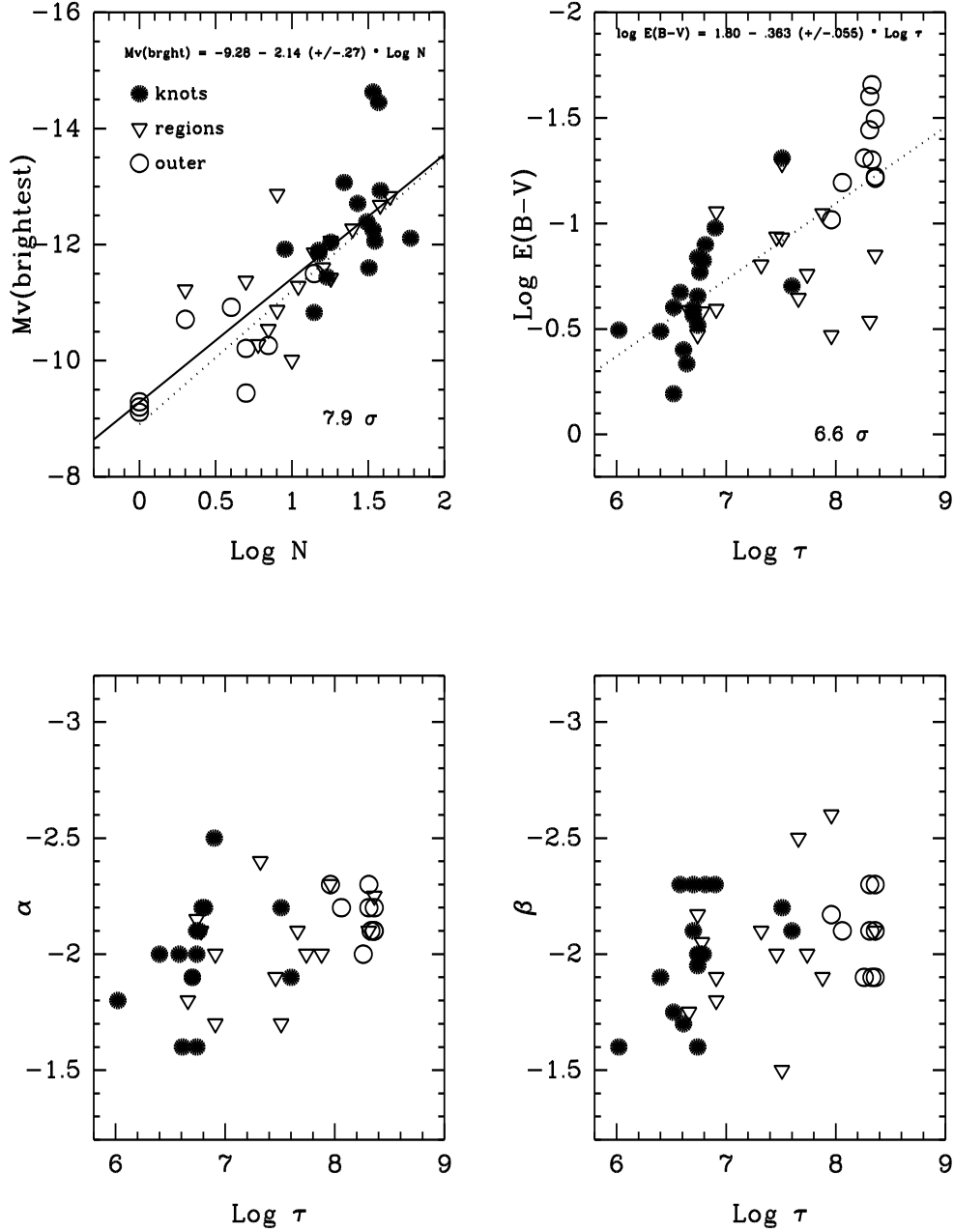


Fig. 18.— Various correlations for clusters in the knots, regions, and outer areas shown in Figure 17. (a, upper left) Absolute magnitude  $M_V$  of the brightest cluster in each area plotted vs. the logarithm of the number of clusters with  $M_V < -9$  in same area (the dotted line is the best-fit line for cluster populations in entire galaxies from WC07); (b, upper right)  $\text{log } E(B-V)$  vs.  $\text{log } \tau$  diagram for same clusters; (c, lower left) slopes  $\alpha$  of the regional luminosity functions plotted vs.  $\text{log } \tau$ ; (d, lower right) slopes  $\beta$  of the regional mass functions plotted vs.  $\text{log } \tau$ . The slopes of the best-fit lines for the top two diagrams are given and the significance ( $\sigma$ ) of the correlation is given to the lower right in each diagram. For a detailed discussion, see text.

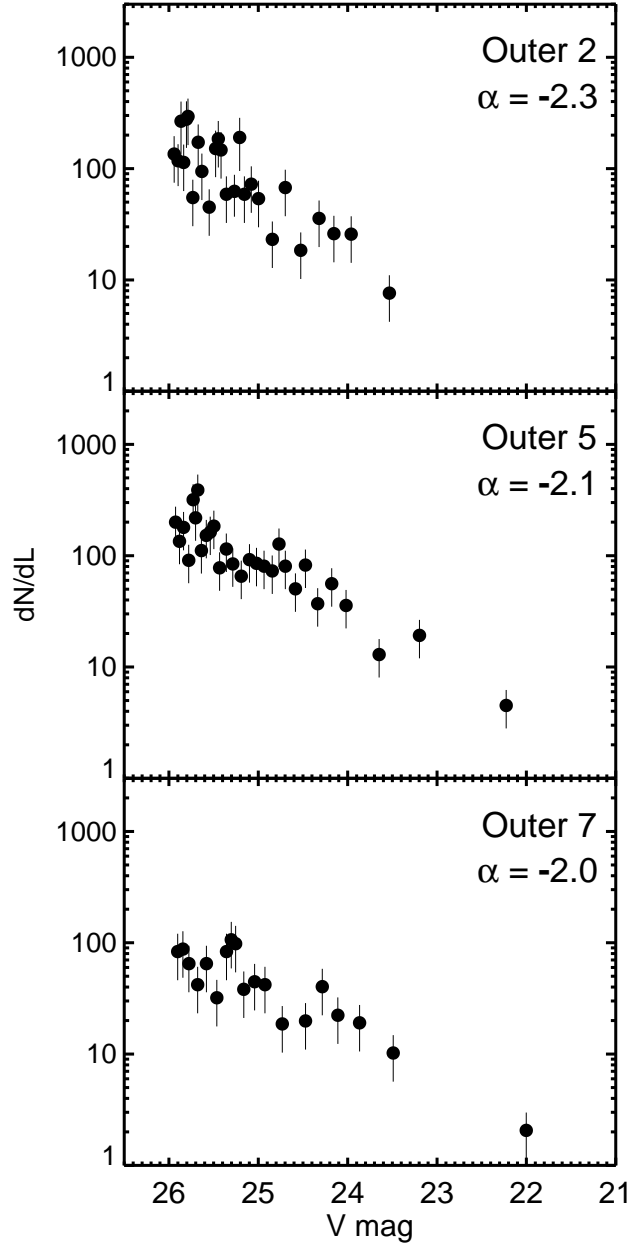


Fig. 19.— Luminosity functions for clusters in three outer areas. Note that there is no evidence of any turnover in the luminosity functions at fainter magnitudes. This is consistent with relaxation-driven cluster disruption models, which predict the turnover should not be observed until  $M_V \approx -4$  for clusters with ages of  $\sim 200$  Myr. This would correspond to a value of  $V = 27.7$  in the diagram.

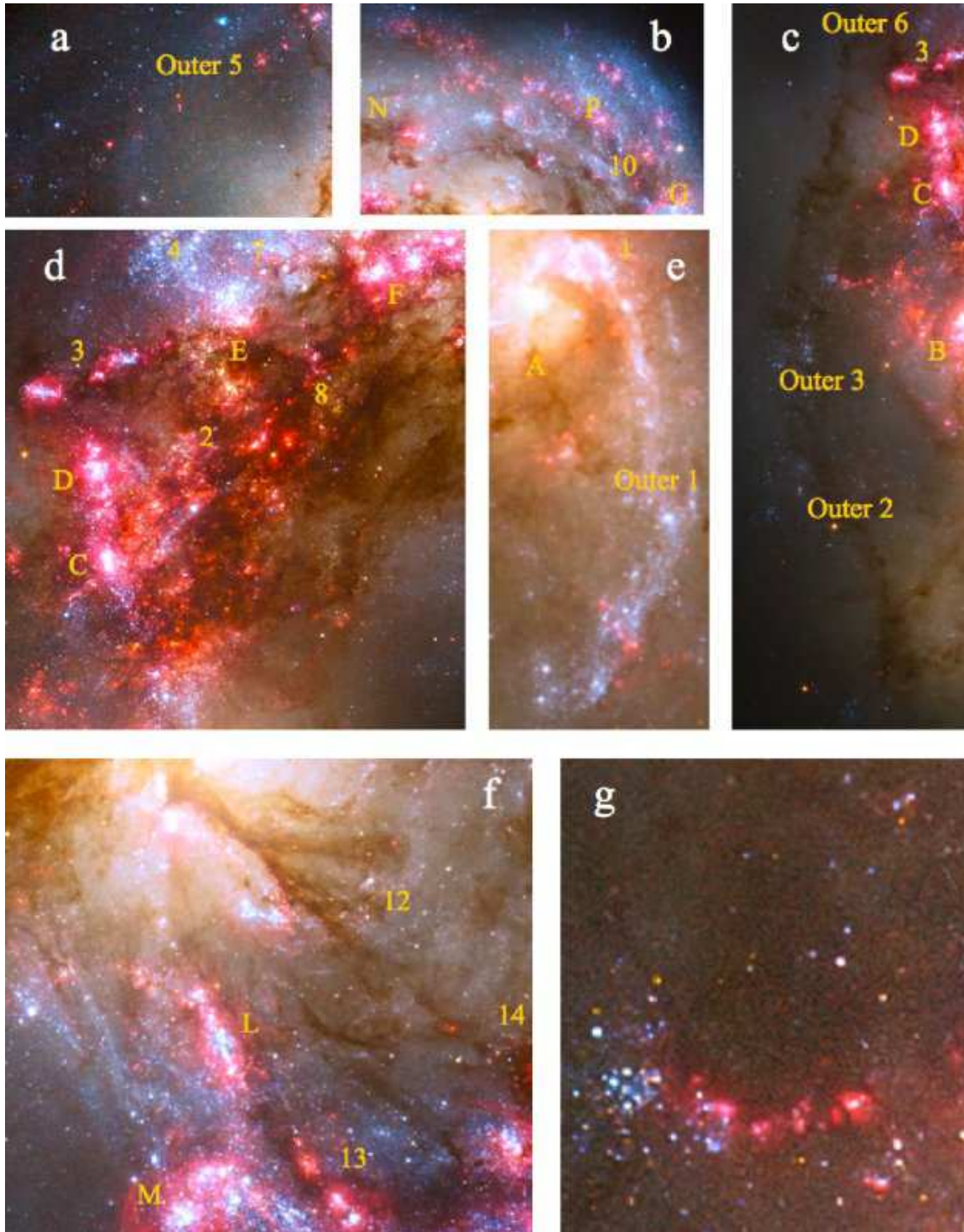


Fig. 20.— Mosaic of subareas in the Antennae (from Figure 1) that show interesting patterns of star formation. The capital letters and numbers in yellow correspond to the definitions of star formation knots, regions, and outer areas defined in Figure 17. For a discussion, see §9.



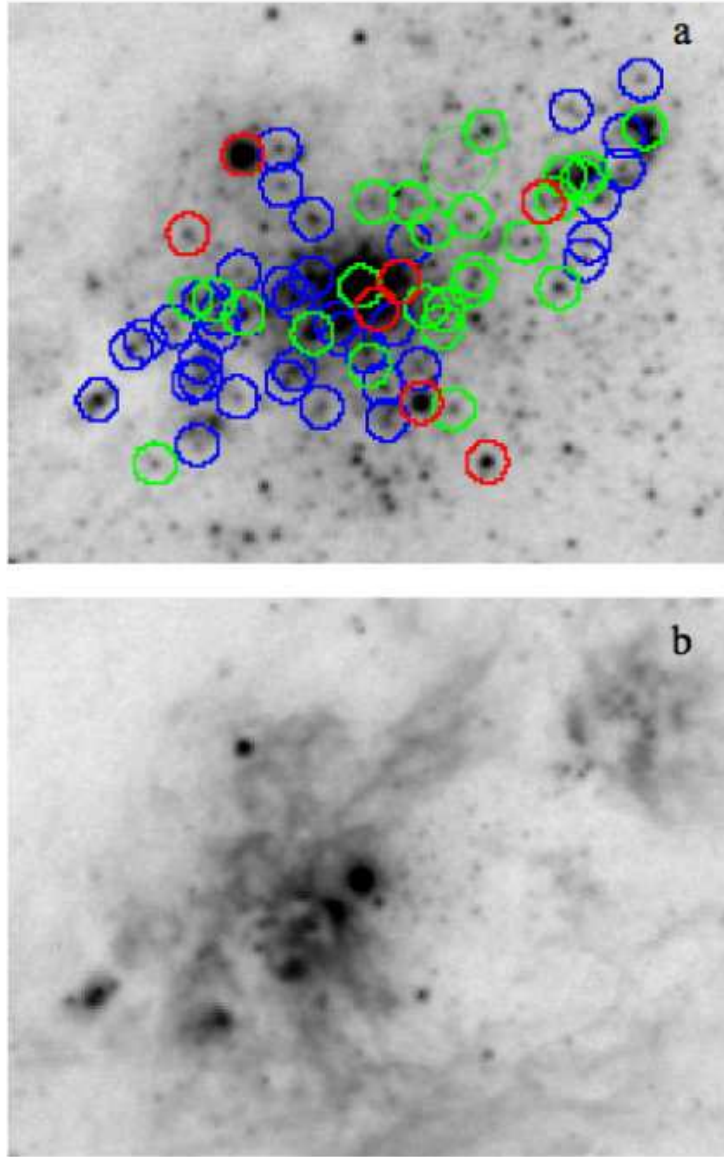


Fig. 21.— Top panel shows the  $V$  image of Knot S, with clusters color-marked by age (blue:  $\log \tau < 6.7$ ; green:  $6.7 < \log \tau < 7.0$ ; and red:  $7.0 < \log \tau < 7.7$ ). The bottom panel shows the corresponding  $H\alpha$  image of Knot S.

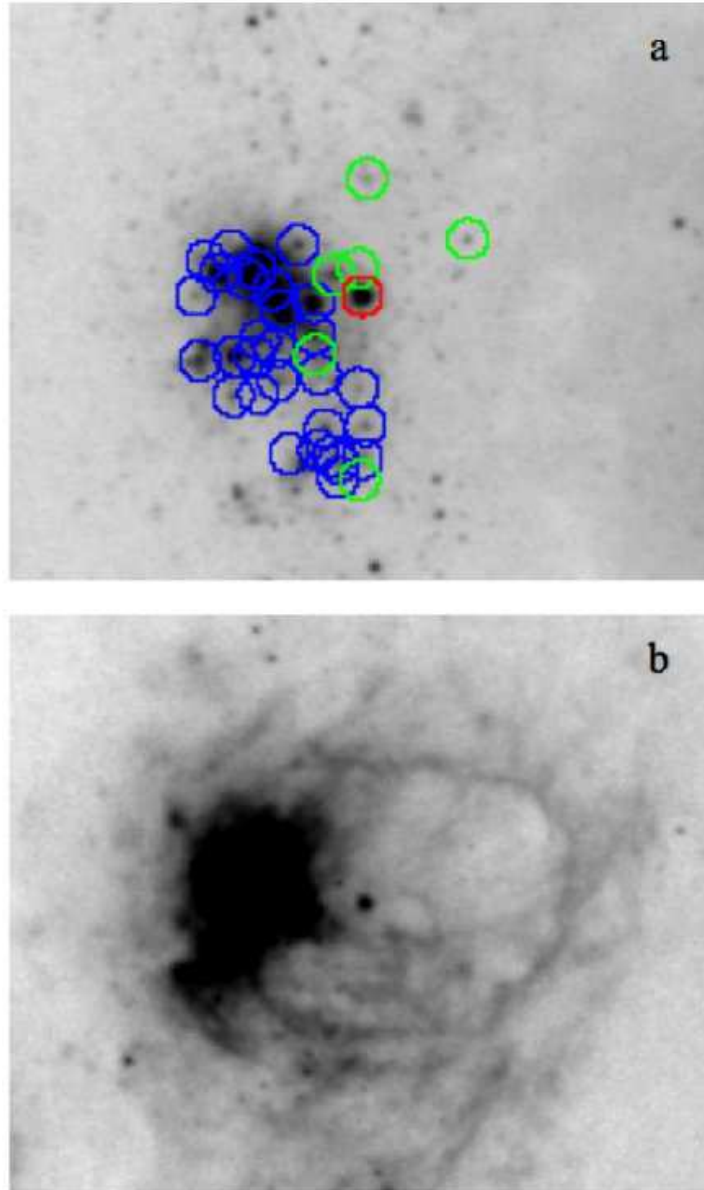


Fig. 22.— Similar to Figure 21, but for Knot B. The one intermediate-age cluster is circled in red and is the 20th most massive cluster from Table 7, with a mass of  $\approx 10^6 M_{\odot}$  and an age in the range 10–50 Myr. It appears to lie at the center of the prominent H $\alpha$  shell (lower panel) and is likely to have triggered the formation of the younger clusters around it, including the second most massive cluster known in the Antennae, with a mass of  $4.2 \times 10^6 M_{\odot}$  and age of  $\sim 2.5$  Myr.

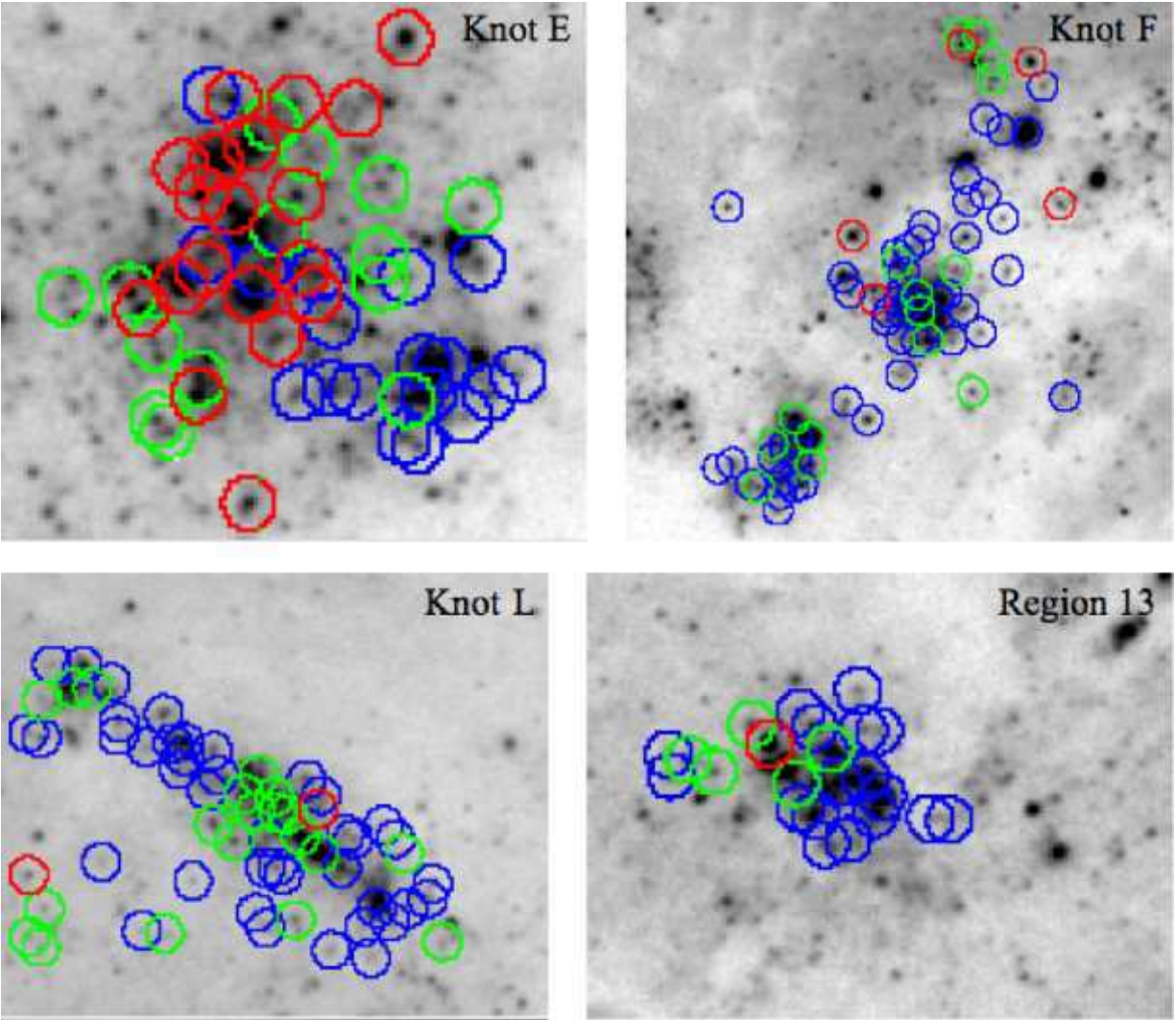


Fig. 23.— Evidence for triggered cluster formation in knots E, F, L, and Region 13. Clusters are color-marked by age (blue:  $\log \tau < 6.7$ ; green:  $6.7 < \log \tau < 7.0$ ; red:  $7.0 < \log \tau < 7.7$ ).

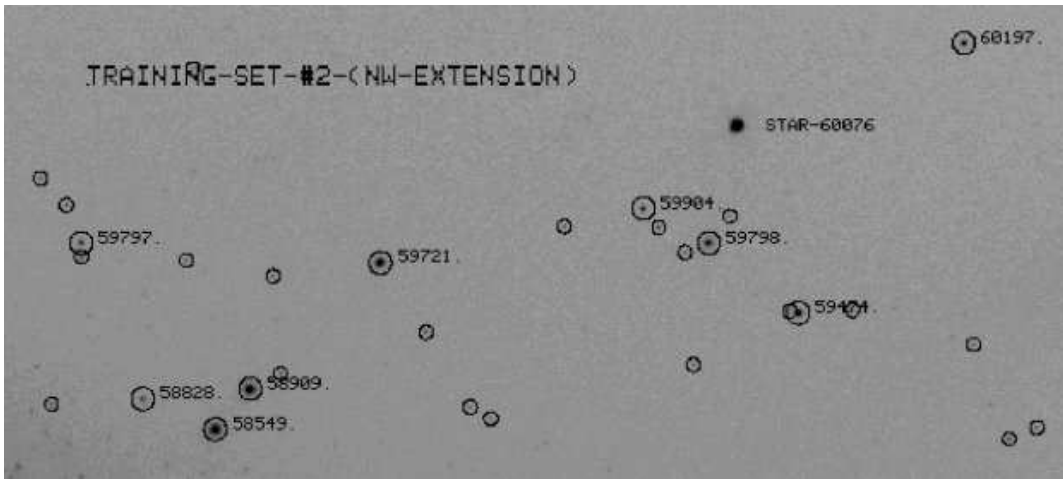


Fig. 24.— Image of area containing Training Set 2. This area is marked “Outer 9” in Figure 17 and is called the “NW Extension” in Whitmore et al. 1999. The most luminous clusters ( $M_V < -8$ ) are marked by large circles with the ID number included (see Table 3), while the less luminous clusters in the range  $-8 < M_V < -7$  are marked by small circles. Most of the fainter clusters are not visible here because of the chosen contrast stretch. Note that the brightest object (60076) is probably a star since it has a concentration index of  $C = 1.39$ , although it has colors similar to the other clusters in the region.

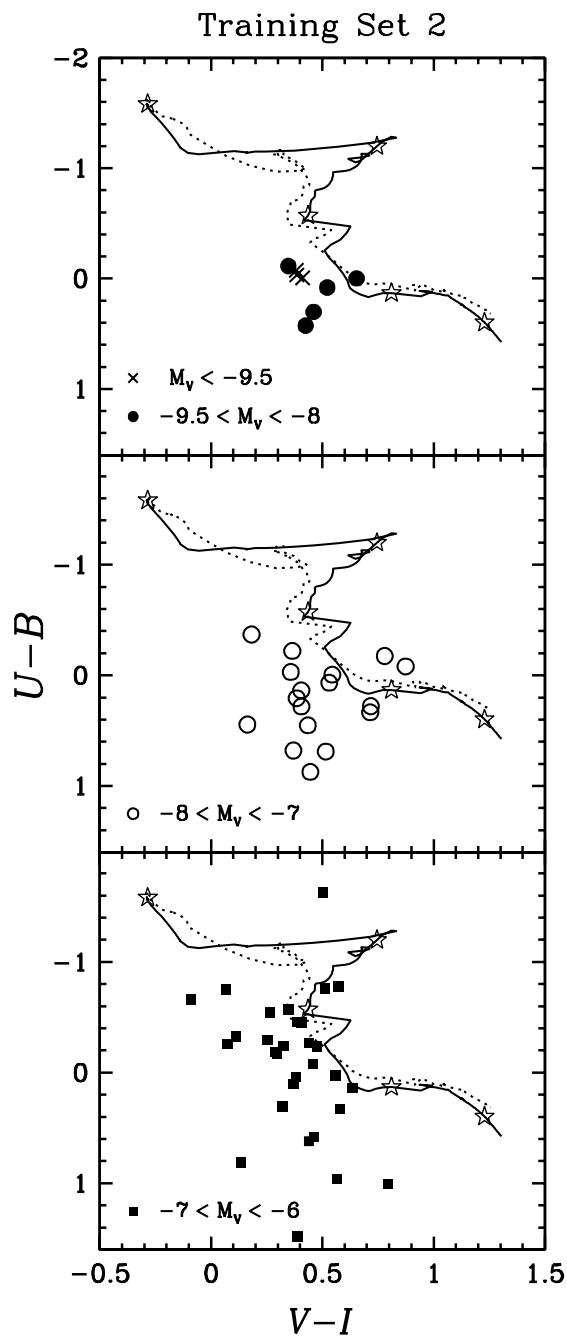


Fig. 25.—  $U-B$  vs.  $V-I$  diagrams for Training Set 2, with objects sorted by absolute magnitude  $M_V$ . Note how small the scatter is for the three brightest clusters (crosses in top diagram) and how it increases for fainter clusters. The solid lines show evolutionary tracks for CB07 model clusters of solar metallicity, while the dotted lines show similar tracks for model clusters of  $Z = 0.4 Z_{\odot}$ .

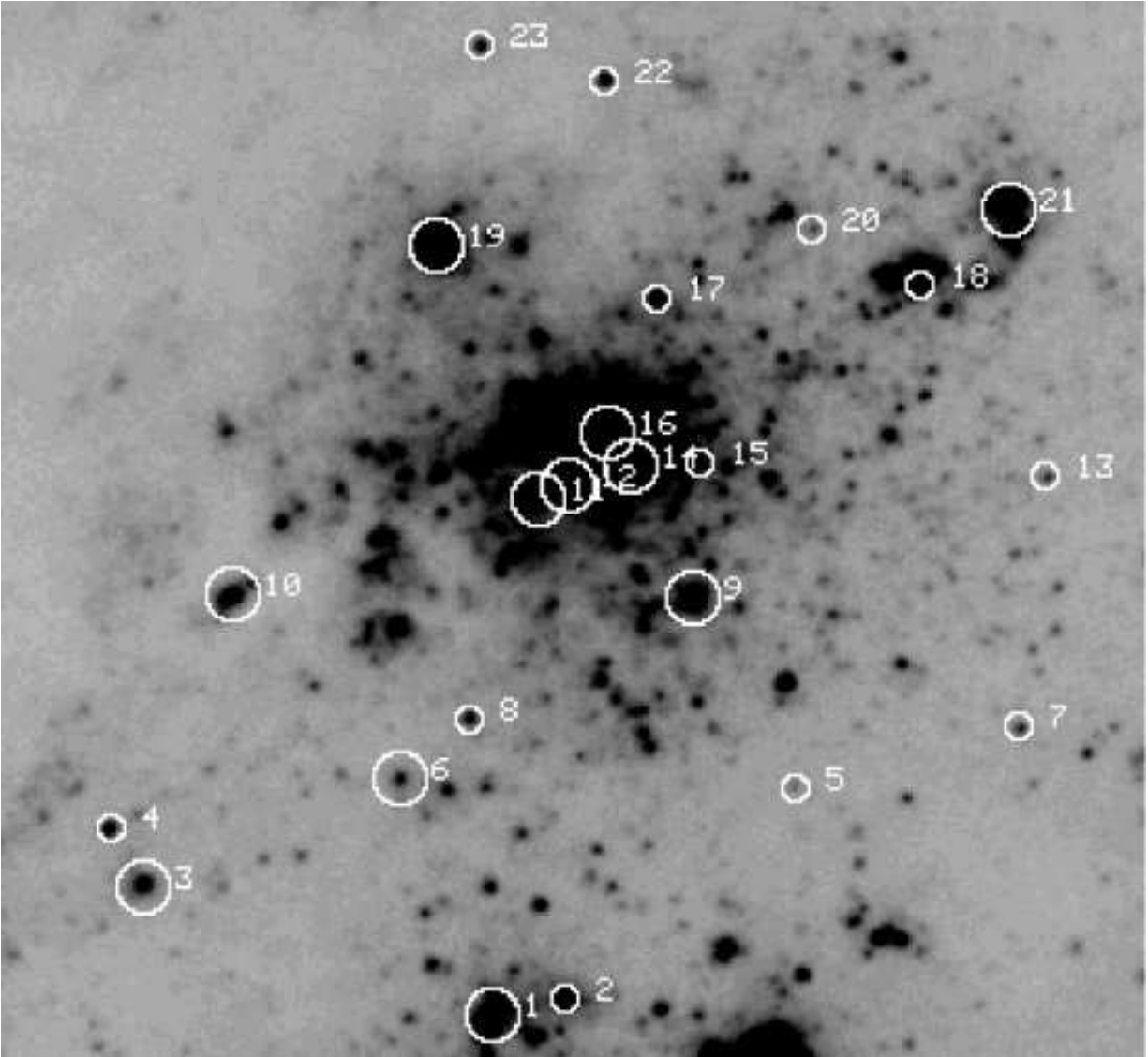


Fig. 26.— Image of the area around Knot S, showing the Training Set 3 objects discussed in the text and listed in Table 4. Large circles mark candidate clusters, while small circles mark candidate stars.

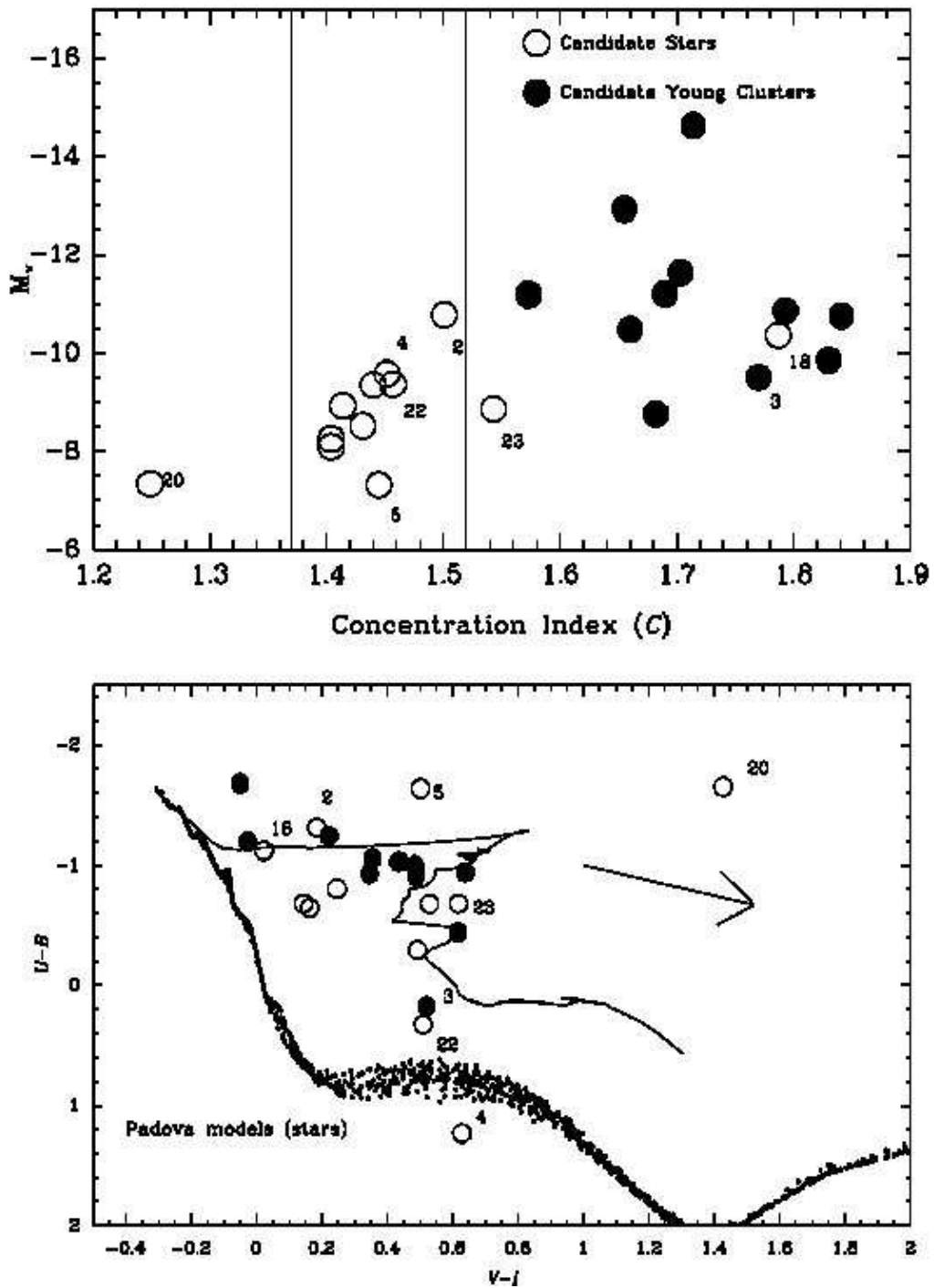


Fig. 27.— Properties for Training Set 3. The two diagrams are similar to those shown in Figure 6 for Training Set 1. See text for a description of how the “candidate” stars and clusters were selected.



Fig. 28.— ACS/HRC image of Knot S from the Hubble Legacy Archive (Whitmore et al. 2009). The cross marks the position of Supernova 2004gt.



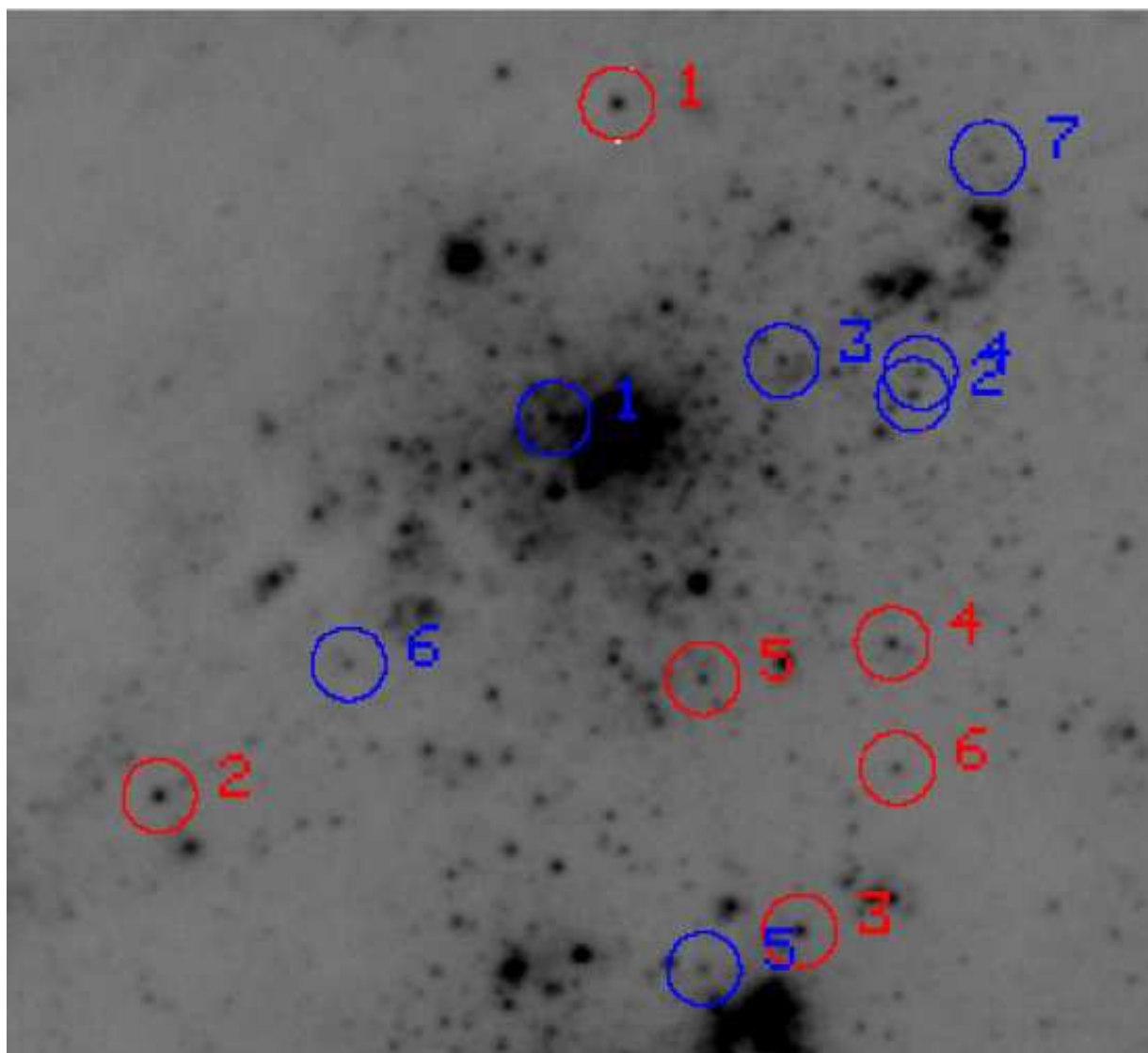


Fig. 29.— Brightest candidate blue and yellow stars in Knot S, taken from Table 5.



Fig. 30.— Enlargement from Figure 28 showing the second-brightest candidate yellow star of Table 5. Note the concentrated light profile of the yellow star (near the center of the image), when compared to a normal blue cluster near the bottom right, and the associated reddish cluster that the star probably resides in. Most of the other yellow and red stars in Figure 28 show similar morphologies, although not as pronounced since the bright stars generally appear more centered on the associated faint clusters. Use the interactive display of the Hubble Legacy Archive ([hla.stsci.edu](http://hla.stsci.edu), image name is *HST\_10187\_03\_ACS\_HRC\_F814W\_F555W\_F435W*) to examine this image in more detail.

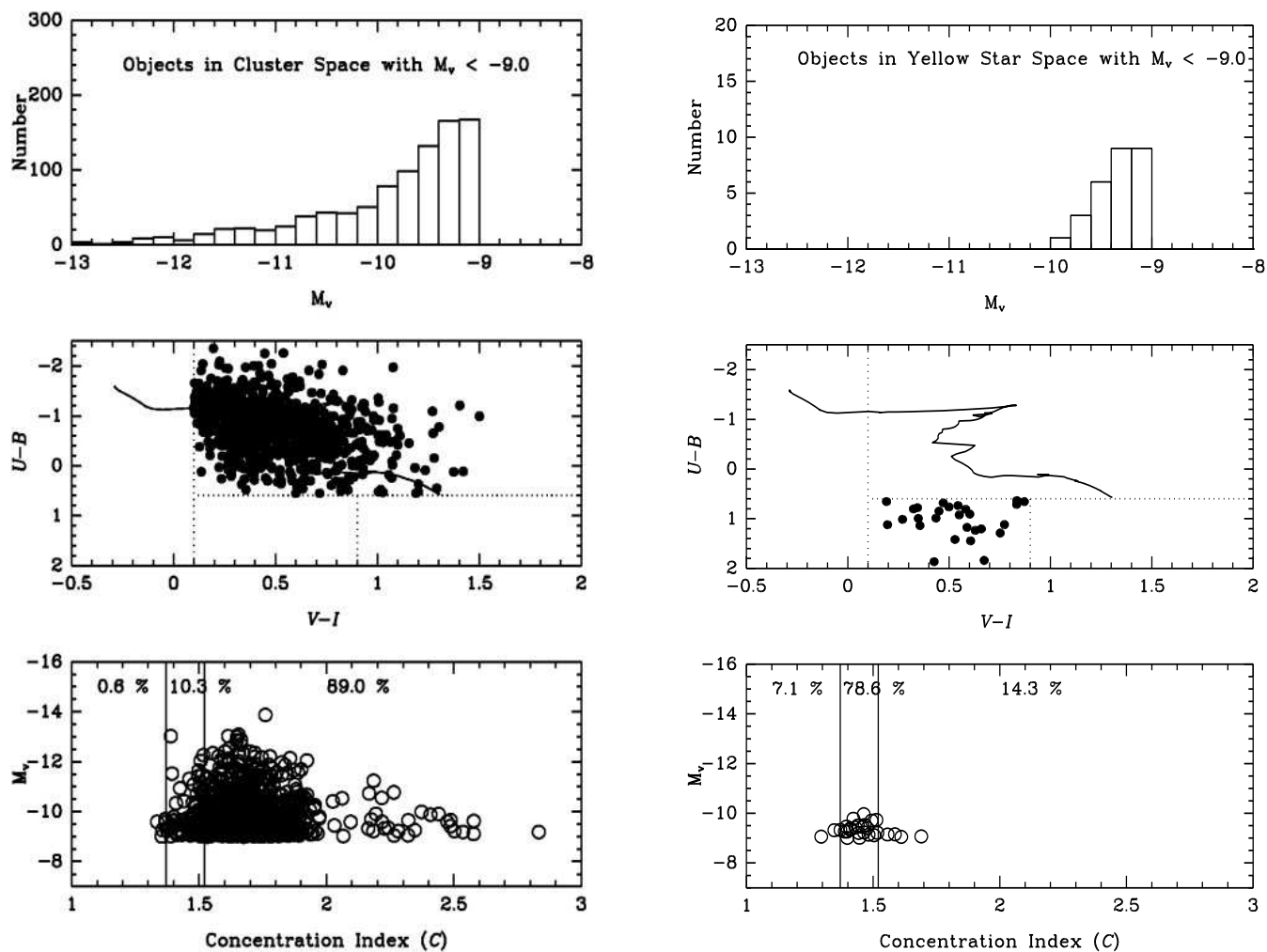


Fig. 31.— (a-left) All objects in the Antennae with  $M_V < -9$  that fall in the “cluster space” portion of the two-color diagram (as described in the text). The top panel shows the number of these objects as a function of luminosity, the middle panel shows their two-color plot, and the bottom panel shows their distribution in  $M_V$  vs.  $C$  and the percentage of objects in each of three bins. (b-right) Same as (a), but for objects in “yellow-star space.”

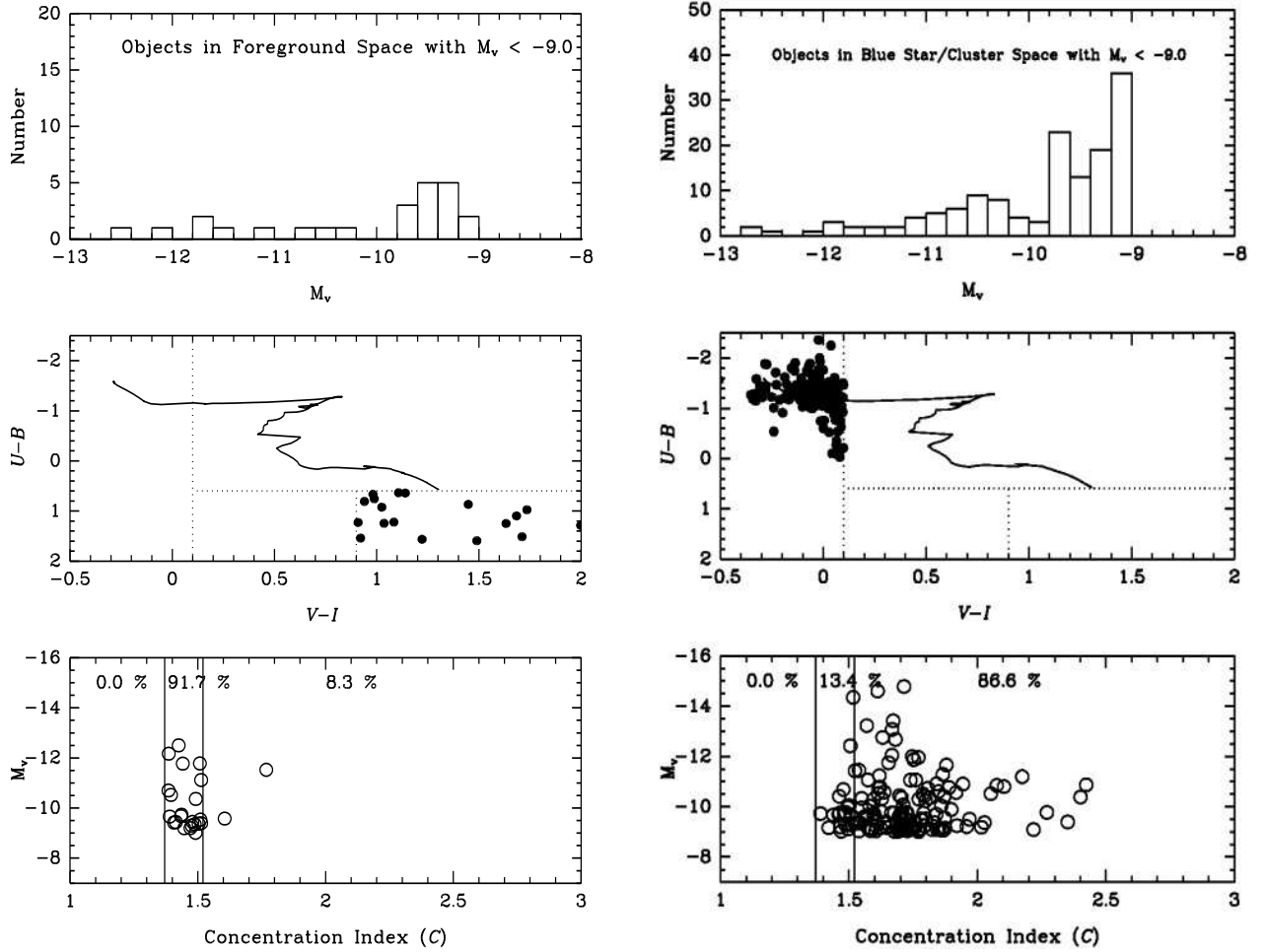


Fig. 31.— (c-left) Same as Figure 31(a), but for objects in “foreground-star space.” (d-right) Same as (a), but for objects in blue-star/cluster space.